Master of Science Thesis

A First Attempt to Analyze Bluff Vehicles at Moderate Reynolds Numbers with *OpenLB*

A. Akopov

Delft University of Technology

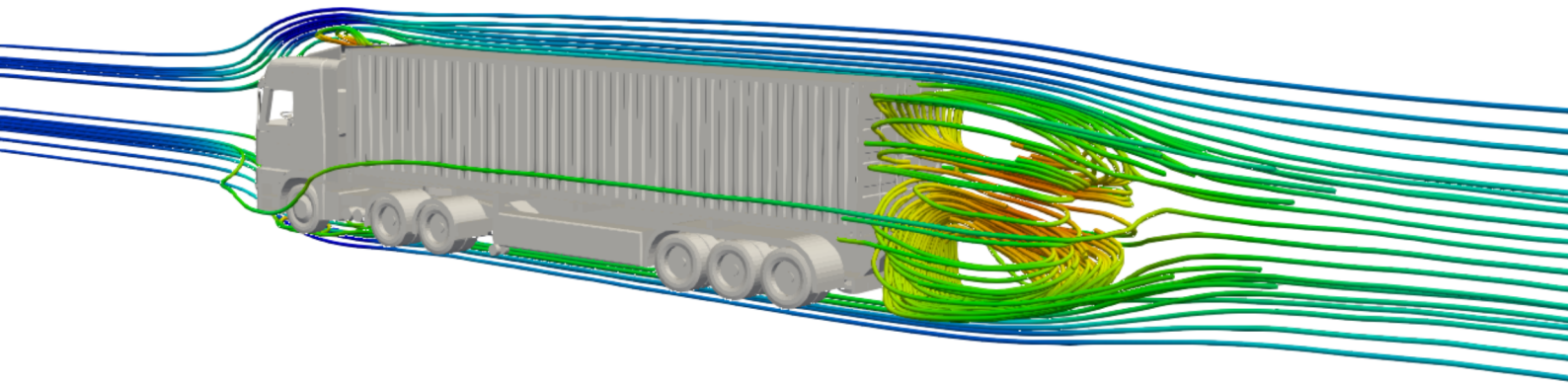

TU Delft

Master Thesis

A First Attempt to Analyze Bluff Vehicles at Moderate Reynolds Numbers with *OpenLB*

by

A. Akopov

to obtain the degree of Master of Science
at the Delft University of Technology,
to be defended publicly on Wednesday September 19, 2018 at 02:00 PM.

Student number:	4020243	
Thesis committee:	Prof. dr. ir. L. L. M. Veldhuis,	Chair
	Dr. ir. G. van Raemdonck,	Supervisor
	Dr. ir. A. H. van Zuijlen,	Examiner

An electronic version of this thesis is available at `http://repository.tudelft.nl/`.

TU Delft

Acknowledgements

This thesis work is the final milestone in achieving an MSc. in Aerospace engineering. The subject required a lot of dedication, perseverance and creativity and without the support of others, this would have been a much harder task. First and foremost I would like to thank by daily supervisor Gandert van Raemdonck for his guidance throughout the whole project and his enthusiasm that motivated me to keep going. Together we started with a very ambitious project that had its surprises along the way, however, we managed to keep going and investigate something that is very new but promising. I also want to thanks Marc Haussman, who gave me a better insight in how *OpenLB* worked and if I had any trouble understanding the code or problems with the simulation he had an answer to solve it.

Furthermore, I want to thank the guys in room 1.05 for there laughs, motivation and keeping a positive attitude in the room, without you it wouldn't be the same. I also want to thank my friends and family for there support, advice and a welcome distraction.

Last but certainly not least, I'd like to thank my mom, she always believed in me and supported me during my endeavors, therefore, making this accomplishment not only mine but also a little bit of hers as well.

A. Akopov
Delft, September 2018

Summary

For the numerical analysis, an open source Lattice Boltzmann Method (LBM) tool called *OpenLB* is used. The tool combines the Boltzmann equation together with Large-Eddy Simulation (LES), as turbulence model, to simulate the fluid behavior. The combination of LBM-LES which is used by *OpenLB* is relatively new within the CFD realm. To asses, the performance of *OpenLB* in the field of flow characteristics, drag prediction and pressure patterns a generic heavy duty bluff vehicle called, Generalised European Transport Model (GETS), is used. The inherent unsteady nature of both LBM and LES are complementary to each other, where LES is accurate in prediction of vortex shedding behind bluff bodies and with the easy parallelization of LBM computational time can be saved. A bluff vehicle such as the GETS model, where separation is expected, is the perfect model to test the performance of *OpenLB* and compare it with established phenomena of bluff bodies in literature and wind tunnel tests. By changing the configuration of the GETS model, variation in front-edge radii and additional boat tails, a better insight into emerging trends can be observed and compared, to validate the open source CFD tool. Furthermore, to investigate if there is potential in *OpenLB* for future projects.

In addition to numerical analysis and a wind tunnel experiment is performed to obtain drag coefficients for the various model configurations. The experimental analysis was performed at Reynolds number varying from 8000 to 60000, based in the square root of the frontal surface. This means that a 1:50 scale model of the original GETS model is used. Mainly, the drag force of the model with different configurations are measured to validate the numerical results. The relative low Reynolds number tested in this study is due to the limitations set by *OpenLB*. The absence of grid refinement, the use of LES as turbulence model and lack of a wall function, constrains the Reynold numbers that can be simulated with keeping computational time in mind. Therefore a choice was made to only simulate the Reynolds number of 8000, 24000 and 48000 and compare the effect it has on the flow characterizer, drag coefficient and pressure.

It was shown that the model with the smallest front-edge radius had the highest drag coefficient. This was the effect of a separation bubble over the front of the model. With increasing the radius the drag is also reduced, observed both by numerical analysis and conducted experiments in literature. The flow is guided over the rounding which gives a more favorable pressure gradient and therefore reduces the separation bubble that arises over the front-edge. Additionally, the effect of applying a simple Bounce-Back or Bouzidi boundary condition on the model is investigated. The interpolative nature of Bouzidi approximates the staircase shape of the rounding with a curve, in contrary to the bounce-back boundary condition. The drag difference between the two boundary conditions was 7.3%, which is moderate but it highly affects the flow over the front. The flow characteristics are simulated at two different heights, one at ground proximity and the other at a higher distance from the ground. The comparison is made because with the experimental analysis the model was placed somewhat higher from the wind tunnel floor to avoid interference with the wind tunnel boundary layer. Normally the model is situated at the ride height of a real-life truck. The position of the model influences the location of unequal sized vortices aft of the model. At ground proximity, the largest vortex is at the top whereas at a higher ride height this is vice versa. Which complies with Particle Image Velocimetry (PIV) performed by van Raemdonck [78]. The ride height did slightly affect the drag coefficient but was within a reasonable difference of less than 3% . Another observation that is made is, with increasing Reynolds the drag coefficient decreases. This is valid for all the front-edge radii for both numerical and experimental analysis.

The addition of the tail lowered the drag of the models, this trend is ascertained by both numerical and experimental analysis. With increasing tail angle the drag reduction also increases which is caused by increasing pressure over the rear part of the model. There are some exceptions. Experimental results show that with the largest tail deflection of 18° the drag is increased. This can be the influence of how the tail is attached to the model and the material used to create the model. A CAD model that is used in the numerical simulation, every angle and dimension is perfect to the specifications. However, with wind tunnel models this not the case and therefore has an influence on the results. In general, the numerical and experimental drag difference is rather high, varying from 50% at low Reynolds numbers to 10% at higher Reynolds numbers. This is mainly the cause of the force balance used to measure the forces in the wind tunnel. The balance is designed

for larger models at higher inlet velocities which generate a larger force. So, at smaller forces, the balance is not that sensitive which gives a wider spread in results at lower Reynolds numbers.

Comparing the flow characteristics of the model with the different configurations a few things can be noticed. That the separation bubble is reduced with increasing radius. Also, the strength of the recirculation region of the bubble is reduced. This is one of the reasons why the drag coefficient is reduced with increasing front-edge radius. Furthermore, the effect of the additional tail on the separation bubble is also visible. The flow over the rear is accelerated by the tilted plates of the tail, which affects the boundary layer over the entire model, it re-energizes regions of low-velocity flow reducing the size of the separation bubble. Comparing the simulated flow behavior of boat tails with a slant angle of 6° 12° and 18° to literature shows satisfactory results. The addition of the tail has three major effects on the flow aft of the tail. First, reduced the wake size. Second, pushed the wake more aft so it has less influence in the model and third, delaying separation over the tail and guiding flow more inward to reduce the vortex strength. All of these core functions of the boat tail are simulated correctly. At each simulated angle the flow characteristic match that described in literature.

The pressure coefficient could not be compared because the position of measurement was not equal. Due to an absence of a wall function the pressure at the wall of the *OpenLB* simulation are zero therefore no true comparison with literature can be made. In literature the pressure is often measured at the face of the body. Hence, no qualitative comparison could be made about the magnitude and the shape of the pressure distribution. However, certain trends are visible with the pressure plots. The larger boundary layer that is caused by a sharp front-edge radius decreases the pressure over the aft of the model, whereas, with a larger front rounding the pressure is increased. The addition of a tail clearly increases the base drag and therefore reduces the drag contribution. The pumping effect, that is very common with bluff bodies, is also observed with the help of the pressure plot. The pumping effect is, in fact, a periodic motion that sheds rear-end vortices generating a longitudinal oscillatory motion. This is reflected in the pressure coefficient plot which shows the back and forth motion with increasing and decreasing pressure coefficient.

In conclusion, it can be stated that *OpenLB* is not yet ready to be used for the mainstream engineering problems. The absence of certain key features limits the tool in many ways. Using LES without grid refinement and wall function only low Reynolds numbers can be simulated. Overall, the flow characteristics that are simulated with the various model configurations are accurate even if the Reynolds numbers are not the same order of magnitude. The drag prediction of the simulations are underestimated if compared to the experimental results. This could be due to the choice of the LES model or the effect of too much dissipation which reduced the drag coefficient. The force balance used in the wind tunnel has also a major influence on the results, by being not sensitive enough at lower Reynolds numbers. Although the pressure coefficient did not match with that of literature some important bluff body phenomenon could be observed from the trends.

Contents

Nomenclature

Abbriviation

BB	Bounce-Back
BC	Boundary Condition
BGK	Bhathnagar-Gross-Kook
CFD	Computational Fluid Dynamics
FVM	Finite Volume Method
$GETS$	Generic European Transport System
GHG	Greenhouse Gasses
HDV	Heavy Duty Vehicle
HPV	High Performance Computer
$ICCT$	International Coouncil on Clean Transport
LBM	Lattice Boltzmann Method
LES	Large Eddy Simulation
LGM	Lattice Gas Model
MRT	Multi-Relaxation Time
NS	Navier-Stokes
$RANS$	Reynolds-Averaged Navier–Stokes
SGS	Sub-Grid Scale
SRT	Single Relaxation Time
St	Strouhal Number
STL	Stereo-Lithography
TRT	Two-Relaxation Time
$VLES$	Very Large Eddy Simulation

Symbols

α	Slant angle	deg
ϵ	Error margin	%
Λ	TRT collision operator	–
ν	Kinematic viscosity	m^2/s
Ω	Collision operator	–
ω	Relaxation parameters	–

ρ	Air density	kg/m^3
τ	Relaxation time	s
C_D	Drag coefficient	–
C_L	Lift coefficient	–
C_P	Pressure coefficient	–
C_s	Smagorinsky constant	–
c_s	Lattice speed of sound	–
F	Force	N
f	Function	–
R	Radius	m
Re	Reynolds number	–
S	Surface	m^2
T	Tail angle	deg
t	time	s
U	Velocity	m/s
x	Voxel size	m

1 Introduction

Climate change is an imminent threat on our way of living. Due to the exponential growth of greenhouse gas emission the world's temperature is rising as can be seen in Figures 1.1 and 1.2. Where darker colors of red indicate temperature rise. These temperature anomalies are becoming more extreme in the last couple of decades. Continued emission of greenhouse gas will cause a further increase in the temperature swings and long-lasting changes to the climate system. This also increases the likelihood of severe and permanent impact on people and the ecosystem. However, there is something of a change in the air with more and more people understanding the importance and urgency to switch from carbon-based energy production to that of a more sustainable one. Scientists predict that if the average temperature on earth will rise with more than 2.0°C [63] that climate change will be irreversible and that more extreme types of weather e.g. flooding, hurricanes, drought, and extreme temperature swings will occur. Consequently, more people have to deal with these types of extremes.

On the 12th of December 2015, the Paris Climate accorded was adopted [77], from that moment a historical amount of 192 states and countries pledged to reduce the global temperature by 2050. The total emission of all the parties that signed the agreements is over 85% of the total yearly greenhouse gasses emitted in the world [88], therefore making it the world's first comprehensive climate agreement.

A large portion of greenhouse gas emission can be accounted to the transport sector. With the increase of prosperity around the globe more goods are consumed by a large part of the global population. The demand for road transport of freight is a secondary demand driven by the worldwide demand for goods and the flexibility that road transport itself supports. For many types of cargo, the commercially available road transport vehicles form the most efficient type of transport, despite the un-aerodynamic shape of heavy-duty road vehicles. However, with increasing demand for road transport also an increase in greenhouse gases emission is unavoidable. Therefore, light- and heavy-duty trucks can be a part of the solution in how the transport sector can reduce their carbon footprint and still find a suitable way to provide our goods and services.

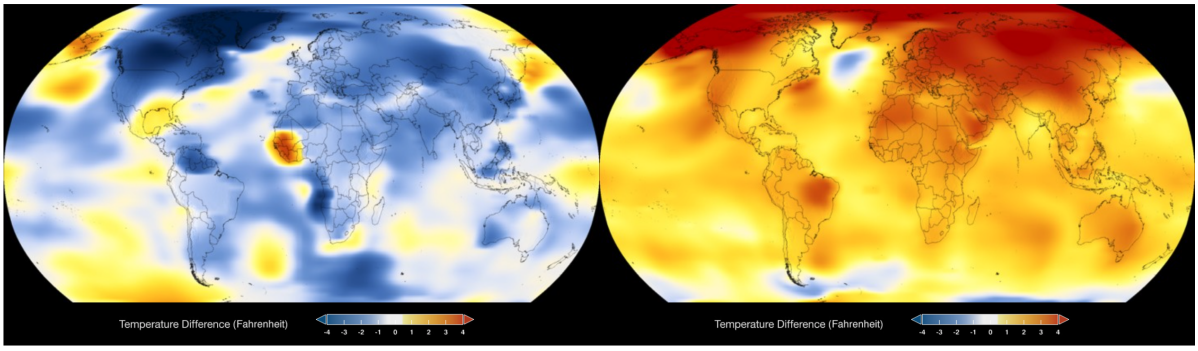

Figure 1.1: Temperature difference map of earth from the year 1884 [56]

Figure 1.2: Temperature difference map of earth from the year 2017 [56]

1.1. Influence of road transport on emission

There is a large consensus among the scientific community that there must be a change in how we deal with greenhouse gas emission to bring it back done to stable levels. Although, there is an urgency to transit from carbon-based energy to a more suitable one. Our world economy is based on growth and this is mainly fueled by our addiction to oil. It requires a tremendous amount of effort to make the transition to a more suitable source of energy and still guarantees the growth that our world economy is based on.

One of the major contributors to the emission of greenhouse gasses (GHG) in the European Union (EU) is the road transport sector. According to the numbers of The International Council on Clean Transport (ICCT) 40% of the fuel used and GHG emissions produced are by heavy-duty vehicles(HDV)[55]. EU Energy and Transport in Figures [15] indicates an increasing trend of GHG emission of the overall road transport sector, as can be seen in Figure 1.3. Figure 1.4 shows that cars are by far the largest contributors of GHG emissions on the road, however, the light- and heavy-duty vehicles also contribute their fair share. Heavy-duty vehicles are known to be inefficient compared to other road vehicles, this is a result of the un-streamlines shape of the truck. The large transport demand, rising energy prices and environmental impact make it a very interesting subject for study and innovation.

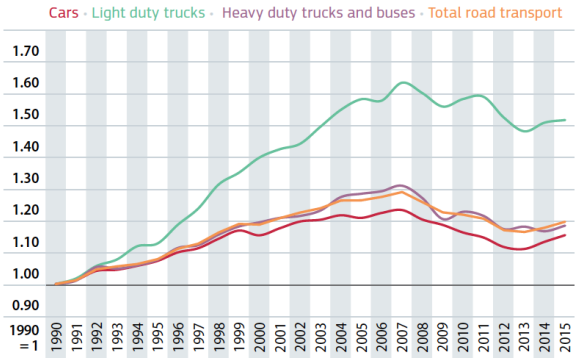

Figure 1.3: CO_2 emissions of road transport in millions of tons throughout the year in the EU[15]

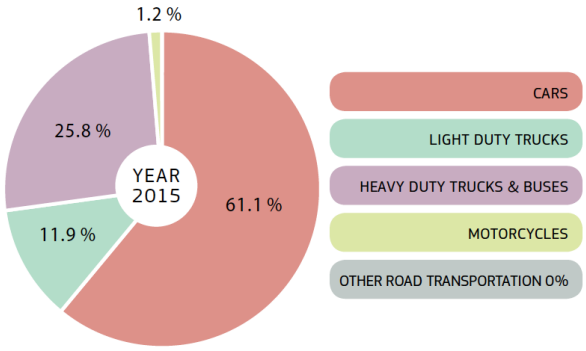

Figure 1.4: Contribution of emissions of road transport in the year 2015 in the EU[15]

In the past decade, intensive studies are performed to increase the efficiency of the heavy-duty vehicle by drastically decrease the drag of those vehicles by making them more aerodynamic efficient [12, 37, 78]]. The largest contributor to the total drag on a road vehicle is the aerodynamic drag, as illustrated in Figure 1.5. The aerodynamic drag, which increases exponentially with the increase of vehicle velocity, $D = C_D 0.5 \rho V^2 S$, emphasizes the importance of aerodynamic design and the possible efficiency gains that can be achieved.

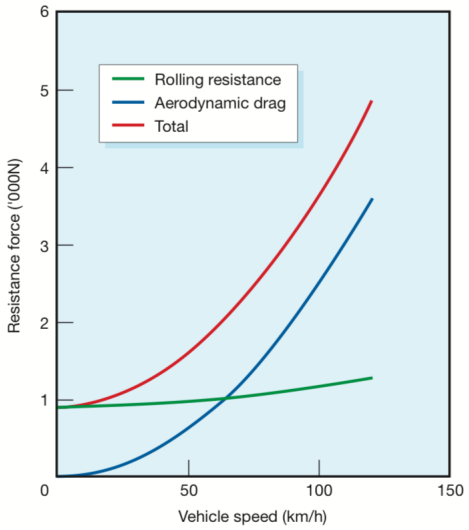

Figure 1.5: Resistance forces created at various speeds of a 10-tonne vehicle [27]

1.2. Bluff body aerodynamics

Heavy-duty trucks and other road vehicles are aerodynamically categorized as bluff bodies in close ground proximity. The design of an HDV must primarily comply with aesthetic, functionality, safety and lastly but maybe most import economical requirements. Where the aerodynamic design is something that is of secondary priority. The regulations in the EU have a considerable impact on the design of an HDV. Due to the specification of the total length of a tractor-trailer combination, designing an aerodynamic efficient body is challenging. The large cross-sectional area and un-tapered trailer shape represents a classic bluff body shape where the largest part of the drag contribution is caused by pressure differences aft of the body.

1.2.1. Bluff Body Basics

Bluff bodies have been investigated since the early days of aerodynamics and have a rich history of being used as validation cases for computational fluid dynamics through the decades[31]. Bluff bodies are bodies that have significant regions of separated flow, this is disregarding whether the separation is at the front or aft of the body. Most road vehicles are typical bluff bodies, especially that of a heavy-duty truck. The aerodynamic drag of a bluff body is due to pressure difference that occurs between the front and rear of the body. This is a significant contribution if compared to the skin friction drag. Where typically 85% of the drag is due to pressure and the other 15% due to friction [86]. Front-edge and rear-end shaping in the form of tapering or boat-tailing have been used to reduce the aerodynamic pressure drag in the past [11]. The result of a study on the contribution of each part to the aerodynamic drag of an HDV is shown in Figure 1.6. When looking at the illustration it is noticed that both the front and rear of the vehicle have the same contribution to the drag.

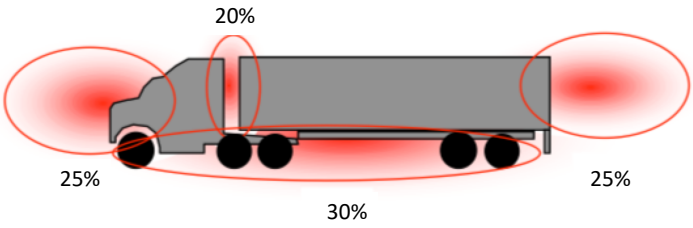

Figure 1.6: Typical drag distribution over a transport vehicle [87]

An aerodynamically inefficient truck is similar to a rectangular block, as shown in Figure 1.7a, the extensive flow separation that is caused by sharp edges at the front increase the pressure drag substantially. To reduce the pressure drag, caused by separation at the front, some modification to the shape of the body need to be made. To make sure the flow will stay attached a streamlined body is needed. In Figure 1.7b a more streamlined truck with a comparable flow is illustrated. Only relatively small changes to the truck shape, have substantial effects on the flow around it, resulting in a drag reduction. In Figure 1.7b a modest radius change of the cabin has a significant impact.

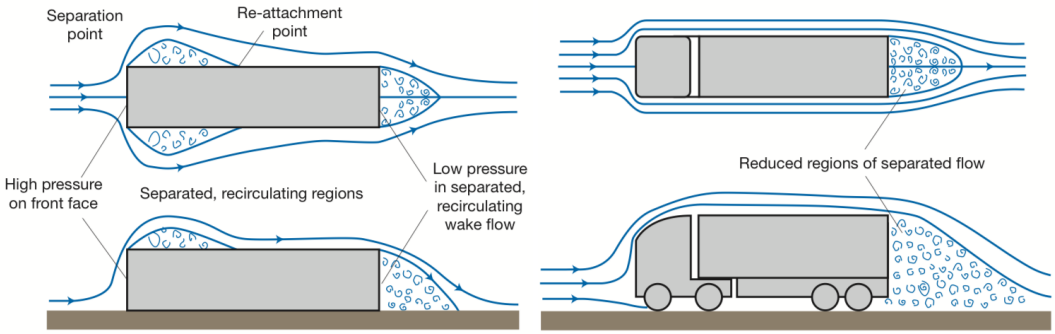

(a) Flow around a typical bluff body

(b) Flow around a streamlined truck

Figure 1.7: Difference in flow topology due to streamlining [27]

The abrupt geometrical change at the rear of a heavy-duty leads to flow separation and dead air region. This region of circulatory flow causes a low-pressure field which subsequently results in a higher pressure

drag. The flow contained at the rear of the body is highly unstable and governed by small and large rotating flows. The region of unsteady flow behind a bluff body is (among others) investigated by Bayraktar et al. [4], Duell and George [14], Khalighi et al. [37]. It was found that the wake behind a bluff body can be separated in two different regions, with the first region containing two vortices with unequal strength. The second region is a shear layer that traps the counter-rotating vortices. In Figure 1.8 both regions are illustrated and the location of these regions are given. The vortex shedding happens in a uniform manner, first from the top and half a period later from the bottom of the model, this is also known as the pumping phenomenon. This pumping effect is related to the periodic drag levels, tire wear and overall vehicle stability.

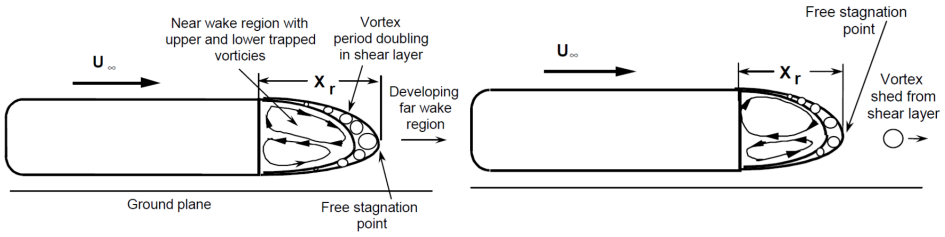

Figure 1.8: Schematic presentation of wake phenomenon behind a bluff body[14]

Reynolds number effect

The Reynolds number represents a dimensionless parameter that gives the ratio between the inertial forces against the viscous forces. At low Reynolds numbers, viscous forces have a more dominant effect on the laminar flow. With increasing Reynolds number the flow becomes more turbulent and a transition in dominant forces from viscous to inertial is observed. The flow at higher Reynolds number a characterized by chaotic, unstable flow with emerging vortices. Wood [85] conducted a study that shows what the effect of Reynolds number has on a typical bluff vehicle body. In Figure 1.9 an illustration of the effect of Reynolds number on the drag coefficient of such a typical bluff vehicle body can be seen.

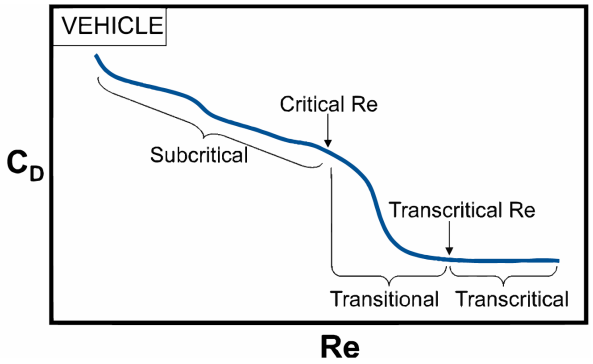

Figure 1.9: Reynolds number effect according to [85]

Figure 1.9 shows four characteristics regions. 1) in the sub-critical the highest drag occurs but also where the boundary layer and separation is laminar. 2) critical Reynolds number is where the boundary layer transition starts and the drag is significantly reduced. 3) In the transitional regions, most of the transition of laminar to turbulent boundary layer takes place. 4) the trans-critical region the drag is invariant and the boundary layer is almost or completely turbulent. When scale models are compared to full-scale models it is important that the wind tunnel test and numerical simulations are performed in the transcritical range where the drag coefficient is some invariant.

1.2.2. Drag Reduction Applications

There lies a great potential in drag reduction devices on a truck like bluff bodies. One of the basic methods to reduce the drag is to increase the front-end radius. Hammache and Browand [25] show that a larger front-end radius has the largest base drag reduction. In addition, flaps and tails increase the base pressure by creating a smooth transition at the rear of the body. These two measures have also a beneficial influence on each other.

Effect of front-end rounding

Rounding the front-edge of a vehicle-like bluff body has considerable influence on the drag coefficient. There have been many experiments where this effect is proven [11, 22, 59]. Cooper [11] performed a quantitative and qualitative research on the behavior of the front end rounding on the drag coefficient for relative high Reynolds number. The paper of Cooper shows that increasing the radii of the front edge will significantly reduce the drag, Hammache and Browand have also proven this. From the same paper, it can be concluded that fully-attached front-end flow does not occur at small radii, no matter how high the Reynolds number. There is an optimal front-edge radius, increasing the radius will not further reduce the drag because the flow will still be attached. There is an analytical equation which gives the minimum radius for attached flow:

$$R_{min} = 1.25 \times 10^5 \frac{\nu}{U_\infty} \tag{1.1}$$

where ν is the kinematic viscosity, U_∞ is the freestream velocity and R_{min} is the minimum radius for attached flow.

Effect of rear-end devices

Large regions of separated flow at the rear of the trailer are one of the underexposed sources of drag for the current base design of an HDV, according to Leuschen and Cooper [49]. An adequate solution to reduce the base drag is to have a smooth transition at the rear-end of the trailer. A way to do achieve a drag reduction is to mount plates at the side of the base to have a more elongated shape, similar to a boat-tail. To increase the effectiveness of such a measure the plates should be placed under an angle. The angle of the plate is crucial in the effectivenesses of the device. The flow over the base should follow the geometry without separating before reaching the trailing edge. If the angle is too large, the flow will separate and the effectiveness of the boat-tail will be reduced. However, if the plates are installed at the right angle the wake at the rear-end of an HDV will have narrowed and moved more downstream. This will increase the base pressure, resulting in a lower pressure drag. Furthermore, the length of the plates has an influence on the effectiveness of the rear-end drag reduction device. Longer tails have a larger taper ratio which leads to a higher pressure recovery over the rear of the base, it also moves the vortex further downstream with increasing base pressure. van Raemdonck [78] investigated the effect of the length of the tail on the drag reduction efficiency and concluded that longer tails are indeed more efficient than smaller tails. In Figure 1.10 a typical tail is shown.

Figure 1.10: Typical tail applied on a HDV [61]

1.3. Aerodynamic Development Tools

In order to achieve the drag reduction for heavy-duty vehicles, there is a need for testing new concepts and ideas. The traditional way is to use a wind tunnel facility to try different configurations and analyze the data that is obtained. Wind tunnel experiments are an important aspect of validating previously conducted research. For the current study, wind tunnel tests are performed for validation purposes. Wind tunnel time is very expensive and often only a scale model can be tested, especially when testing large road vehicles. Furthermore, wind tunnel tests can be complicated and dangerous, often uncertainties in flow and boundary layers arise making the measurement errors larger.

A different approach to test distinct concepts of drag reduction devices on heavy-duty vehicles is using a numerical method that simulates the fluid dynamics. Computational Fluid Dynamics (CFD) is nowadays used in many design processes to have a faster iteration of design changes and their influence on aerodynamic performance. Computational Fluid Dynamics simulations provide unequaled insights into the behavior of fluids over time and space. All the field quantities are available simultaneously at every location in the domain and can be accessed directly, which gives a better insight into fluid phenomena. However, there is a need to have a critical view on the obtained results, because different models give different outcomes and some of them can produce non-physical results. Hence, the critical view on the simulated results is needed. This can be achieved through means of validation and verification.

These two aerodynamics development tools are not self-contained, they are supplementary to each other. Both are evenly important tools for the development of more aerodynamically efficient designs and understanding the flow behavior better.

1.3.1. CFD: Navier Stokes

The standard practice nowadays is to use numerical discretization methods to solve the Navier-Stokes equation. There are commercial packages for this e.g. Fluent Ansys or Open source tools, e.g. OpenFOAM or SU2, that are used by academics but also increasingly more by industry. The best part of Open source software is that a collective development between multiple independent contributors is achieved. This creates a broad design perspective that can be further developed and adjusted to needs of the community for a longer period of time.

Apart from the access to certain CFD packages, another important aspect of CFD that is gaining momentum is, transient flow modeling. This gives a detailed view on transient flow phenomena which is not possible in steady-state. With transient flows, the simulation is time-dependent, which means that the flow propagation is visible and can be studied over time. Currently, most of the fluid flow simulations are steady-state. This type of simulation gives information about the mean flow and the magnitude of the fluctuations. But also statistical data about an assumed stochastic process.

Although, this is an important aspect of improving the aerodynamic performance of a wide scale of applications it does not give a detailed understanding of crucial flow behaviors. In the last couple of decades new development in CFD, away from the traditional Navier-Stokes, is happening. It is called the Lattice Boltzmann Method, the method distinguishes itself from the Navier-Stokes equation by being inherently transient and easy to parallelize [42].

1.3.2. CFD: Lattice Boltzmann Methods

The Lattice Boltzmann method (LBM) is a relatively new and still developing method to simulate the fluid mechanic properties of complex flows. The relative newness can be placed within a certain time frame. If Ansys-Fluent is considered, which is a popular Navier-stokes solver who uses a finite volumes discretization processes. Fluent inc. was acquired by Ansys and is developing CFD software since the 80's with a publication, one of many to mention, of useful commercial application described by Dodge and Schwalb [13]. This was not the first publication but was a result of decades of work. In contrast to that, Exa cooperation who founded in 1991, was the first successful company that implemented LBM for CFD. It published its first paper about a commercial application in 1999 by Halliday et al. [24]. This sets the use of LBM in more contrast to the more traditional way of solving computational fluid dynamics problems by either means of Finite Difference, Finite Element or Finite Volume.

LBM is characterized by its focus on constructing simplified kinetic models that incorporate the physics of microscopic processes from which the macroscopic flow characteristics are computed. The conventional computational fluid dynamics solvers are more focused on solving the macroscopic Navier-Stokes equation. As a result of a different approach to solving the fluid mechanics problem, it is based on a particle picture but focuses on the averaged macroscopic behavior for a variety of different situations. Ranging from flow through porous media to flow over an airfoil. The main improvements of the LBM compared to the conventional methods are correlated to the ease of implementation and is highly suitable for parallelization of the algorithm, therefore making it a revolutionary method for future CFD problems. There is also a study that investigates the performance of LBM by using GPUs instead of CPUs [38].

Succi, who is a renown name in the Lattice Boltzmann Method community, shines his light on the coming twenty-five years of Lattice Boltzmann Methods in [73]. An un-risky statement is to say that the LBM will have more attention and will keep on growing to be a useful tool in the field of classical fluid dynamics problem and soft matter research. With the addition of high-order lattices with more discrete velocity sets, kinematic

boundary conditions and a better tuning of kinematic nodes will surpass the possibilities of Navier-Stokes in certain areas of the fluid dynamic realm. Furthermore, the numerical stability issue that presents itself at high Reynold number flow will have a better behavior and be more stable. The same can be said about the turbulence modeling, with more and more research is done to make the transition from Reynold-Average Navier-Stokes (RANS) turbulence modeling to Large Eddy Simulation (LES). The future of LBM is looking bright, nonetheless, the path to it is still long and challenging.

Most of the LBM literature that is published in recent years investigated 2D laminar flow cases such as, Poiseuille flow, the lid-driven cavity flow, and the flow past a cylinder. Furthermore, 3D academic cases are also investigated such as round and square cylinders, all for low Reynolds numbers. True turbulence scale only exists in 3D, thus 3D academic cases are fundamental to the development of wall models, improve turbulence modeling and have a reliable force predicting function, among other improvements. Apart from the academic test cases, an interesting investigation would be to see if an LBM-LES combination can be applied to bluff vehicle bodies. With these type of bodies, separation is evident and are a source of aerodynamic inefficiency. The strength of the LBM-LES combination is the transient nature of both LBM and LES as turbulence model. This marriage gives the accuracy of an LES model with fast computation, due to parallelization, from LBM. This strength comes to its own on bluff vehicles with a side flow where separation is imminent and hard to predict. This study could be a stepping stone to investigate the performance of the LBM-LES combination on full-scale heavy-duty vehicles and gain a better insight into transient flow phenomena.

1.3.3. Open Source Lattice Boltzmann Methods

Open source lattice Boltzmann methods are relatively new to the CFD universe. Compared to the open source (OS) Navier-Stokes solvers which have a large and thriving community of developers and users. The two commonly known used OS lattice Boltzmann codes are *Palabos* and *OpenLB*. For this study, *OpenLB* is chosen mainly because of the code structure. It's a C++ package that enables researchers and engineers to implement both simple and advanced applications of CFD problems. The architecture of the code is designed to be easily adaptable to various problems and extending the usability of the program is made as user-friendly as possible.

OpenLB uses LES to model turbulence. As mentioned before, LBM-LES only limits to scientific research on a fundamental level. There is a gap in literature on how *OpenLB* performs with obstacle placed in a channel flow at moderate Reynolds numbers. Especially, how the flow and macroscopic quantities of heavy duty vehicle-like bluff body compare to e.g. wind tunnel test or literature. Does the fundamental behavior of the simulated flow match that of proven experiments? This is not yet studied, hence making it an interesting topic to investigate and show the current state of open source lattice Boltzmann method. In addition, open source software becomes a larger part of not only the scientific community but also the general public. Giving it an extra dimension to the current study.

1.4. Present study

Lattice Boltzmann Method is a new method to compute fluid dynamics problems. It uses a different approach, away from the normally used Navier-Stokes, in solving these problems. The traditional way of using finite volume to simulate fluid dynamics has proven its contribution and value to understand the fluid dynamics better. The potential of LBM is not shared by everybody and therefore need to prove itself to change that view. A company that is well on its way to change the view of using LBM in CFD applications is the Exa cooperation. Exa cooperation created a CFD package that is based on LBM, called PowerFlow. As with most commercial CFD tools, there is an open source counterpart that provides an alternative, and these tools are gaining more and more traction One of the open source CFD packages that uses LBM is *OpenLB*, which will be used in this study. The program is relatively new, initiated in 2001, compared to other open source packages that are based on Navier-Stokes. OpenFOAM, for example, is initially released in 2004 and has come a long way since.

To investigate how *OpenLB* performs in the fields of flow characteristics, drag prediction and pressure distribution a validation study is performed using bluff vehicles. The optimization of a bluff vehicle is an intensively researched topic due to higher fuel prices and greenhouse gas regulations, so there is an abundance of literature to measure the performance of the current state of *OpenLB*. Furthermore, LES turbulence modeling is known to performs very well with problems where flow separation prediction is of the essence, this is especially the case with bluff vehicle bodies. Due to the unsteady nature of both LES and LBM means that both methods are very suitable for transient flow problems where separation is a large part of the problem. This makes *OpenLB* which uses the LBM-LES combination highly appropriate to apply to heavy duty

shaped bluff bodies. It will also give an insight if *OpenLB* is a tool that has the potential to be used for further investigation of bluff bodies flow behavior.

All in all, this study tries to give a clear view of where *OpenLB* stands today and if this could be a good alternative to use in the future for transient aerodynamic problems. This leads to the main question that the present study tries to answer:

> **How does *OpenLB* perform with 3D bluff bodies at moderate Reynolds numbers when compared to wind tunnel tests and literature?**

Open source Lattice Boltzmann Methods is a young and fast developing field of research, which has major benefits but also drawbacks. To test the performance of such an open source code and therefore answering the main question of this study, several sub-question is formulated that try to give a satisfactory answer on the question of the present study:

- Are the flow characteristics of a typical bluff vehicle captured by *OpenLB* simulations?
- How well does *OpenLB* predict the drag coefficient when compared to wind tunnel test of a bluff vehicle with various front- and rear-end configurations?
- Does the pressure coefficient simulated by *OpenLB* match with patterns found in literature, for the front- and rear-end of the bluff body?

To achieve the research objective and answer all the research question the following approach is taken. Firstly, the lattice Boltzmann method is explained in more detail. On the bases of the *OpenLB* structure, all the various aspects involved are elaborated in detail in the next chapter. Once the theory is described the numerical set-up for the simulated is discussed in Chapter 3, together with the numerical results. Furthermore, wind tunnel set-up and results are presented in Chapter 4. To validate the simulated drag coefficients and measure the performance of drag prediction by *OpenLB* a wind tunnel experiments is conducted. Lastly, in Chapter 5 both results are compared and with reference to literate a final answer is given to the questions that are stated above. From which conclusions can be drawn and recommendation on future research topics are given in Section 6.1.

2

Lattice Boltzmann Method

In this chapter, the Lattice Boltzmann Method will be discussed in depth. Explaining every step of implementing the method in the used software. An open-source Lattice Boltzmann Method code, *OpenLB*, is used to perform the fluid dynamic simulation. The *OpenLB* project was initiated in 2006. Between 2006 and 2008 Jonas Latt was the project coordinator. As of 2009, Mathias J. Krause has been coordinating the project. The project contributors are mainly Ph.D. students from Karlsruhe Institute of Technology (KIT) and research partners from other universities all over the world.

2.1. Introduction to Lattice Boltzmann Methods

Lattice Boltzmann Method (LBM) is evolved from Lattice gas models (LGM). In LGM, fictitious particles are on a 2d lattice where the particles collide and stream in a way that respects the fluid mechanical properties of conservation of mass and momentum. This is quite similar to how molecules move in real gas[26]. The LGM was originally developed to simulate fluid flow, however, the microscopic approach introduced a lot of noise and fluctuations on that scale. For this reason, the method was abandoned for the Lattice Boltzmann Method that took a mesoscopic approach which reduced the noise and fluctuations in the particle population.

The equation for solving fluid dynamical problems are particularly difficult to solve in general. Problems with complex geometries and boundary conditions are customarily solved by numerical methods. However, a numerical method to solve fluid dynamic equations are both hard to implement and parallelize. The numerical scheme for the Boltzmann equation somewhat paradoxically turns out to be quite simple, both to implement and to parallelize. The reason is that the force-free Boltzmann equation is a simple hyperbolic equation which essentially describes the advection of the distribution function with the particle velocity. In addition, the source term depends only on the local value and not on its gradients [42].

Discretizing the Boltzmann equation in velocity space, physical space and time, we find the Lattice Boltzmann equation

$$f_i(\mathbf{x} + \mathbf{c}_i \Delta t, t + \Delta t) = f_i(\mathbf{x}, t) + \Delta t \Omega_i(\mathbf{x}, t) \tag{2.1}$$

This equation expresses that particles $f_i(\mathbf{x}, t)$ move with a velocity $\mathbf{c}_i$ to a neighboring point $\mathbf{x} + \mathbf{c}_i \Delta t$ at the next time step $t + \Delta t$, this is illustrated in fig. 2.1. At the same instance the particles are influenced by the collision operator Ω_i. This operator models particle collisions by redistributing particles among the populations f_i at each site. There are various types of collision operators available, the simplest one that also can model the Navier-Stokes equation is the Bhatnagar-Gross-Krook (BGK) operator [5]

$$\Omega_i = -\frac{f_i - f_i^{eq}}{\tau} \tag{2.2}$$

It relaxes the population of particles towards an equilibrium, f_i^{eq}, at a rate that is determined by the relaxation time, τ. Other collision operators exist that make use of additional relaxation times to achieve increased accuracy and stability.

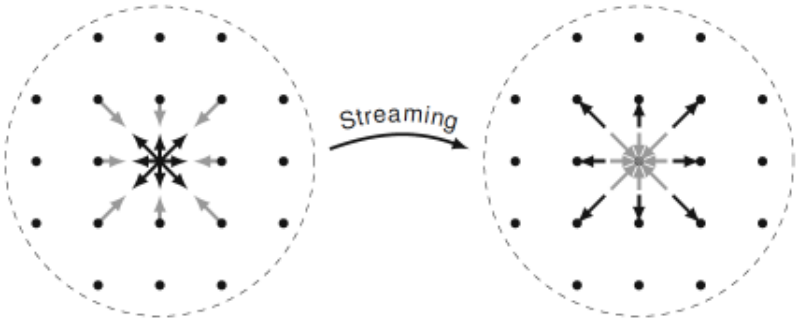

Figure 2.1: Particles (black) streaming from the central node to its neighbours, from which particles(grey) are streamed back. To the left we see post-collision distributions f_i^* before streaming, and to the right we see pre-collision distributions f_i after streaming[42]

$$f_i^{eq}(\mathbf{x},t) = w_i \rho \left(1 + \frac{\mathbf{u}\cdot\mathbf{c}_i}{c_s^2} + \frac{(\mathbf{u}\cdot\mathbf{c}_i)^2}{2c_s^4} - \frac{\mathbf{u}^2}{2c_s^2}\right) \tag{2.3}$$

Equation (2.3) shows the form of the equilibrium term of the BGK operator, with the weights w_i specific to the chosen velocity set. A more elaborated explanation about velocity set is done in Section 2.2. The equilibrium depends on the local macroscopic quantities of the density and velocity. The link between the LBE and the NSE can be determined using the Chapman-Enskog analysis[9]. Through this analysis, it can be established that the LBE behaves according to the Navier-Stokes equation, with the kinematic shear viscosity given by the relaxation time, τ.

$$\nu = c_s^2\left(\tau - \frac{\Delta t}{2}\right) \tag{2.4}$$

relaxation time is a very important variable in the Boltzmann equation, it is a key variable for the convergence and accuracy of the simulation.

The unique part of the Lattice Boltzmann equation (LBE) is the collision and streaming step, which can be computed parallel. If we take the simplest collision operator of eq. (2.2) and substitute in the discretized LBE of eq. (2.1) we get an equation in the form of

$$f_i(\mathbf{x}+\mathbf{c}_i\Delta t, t+\Delta t) = f_i(\mathbf{x},t) - \frac{\Delta t}{\tau}\left(f_i(\mathbf{x},t) - f_i^{eq}(\mathbf{x},t)\right) \tag{2.5}$$

The equation can be split into two separate operations, collision and streaming. The collision part, also know as the relaxation is the first part of Equation (2.5)

$$f_i^*(\mathbf{x},t) = f_i(\mathbf{x},t)\left(1 - \frac{\Delta t}{\tau}\right) + f_i^{eq}(\mathbf{x},t)\frac{\Delta t}{\tau} \tag{2.6}$$

The second part is streaming and can be extracted from the other part of eq. (2.5) as seen in Figure 2.1

$$f_i(\mathbf{x}+\mathbf{c}_i\Delta t, t+\Delta t) = f_i^*(\mathbf{x},t) \tag{2.7}$$

Overall, the LBE concept is straightforward. It consists of two parts: collision and streaming. The collision is simply an algebraic local operation. First, one calculates the density and the macroscopic velocity to find the equilibrium distributions f_i^{eq} as in eq. (2.3) and the post-collision distribution f_i^* as in eq. (2.6) . After the collision, we stream the resulting distribution f_i^* into neighbouring nodes as in eq. (2.7). When these two operations are complete, one time step has elapsed, and the operations are repeated.

2.2. Lattice Characteristics

In Equation (2.3) an term is introduced that describes the discrete velocity set, w_i. This naturally begs the question of what this term is and how to choose the appropriate set discrete velocities for a given problem. As mentioned before the LBE divides the fluid domain in velocity space, physical space and time. Discretizing the velocity space gives prescribed paths in a lattice on which the particles move. These prescribed paths are introduced to limit the movement of the particles from infinite to an amount that does not cost an immense

computational effort to solve the fluid dynamic equation. But still, find an appropriate set of paths to have a sufficiently resolved simulation to allow a consistent solution of the Navier-stokes equation. It is important to find a set of minimum velocities that describes physical behavior, nevertheless keeping the computational cost in mind.

There are various ways to construct a Lattice Boltzmann velocity set. One of which is based on the Gauss-Hermite quadrature[68], this leads to velocity sets that are writes as follows: D1Q3, D2Q7, D2Q9, D3Q15, D3Q19 and D3Q27, where D is the spatial dimension and Q gives the prescribed number of velocity paths. In Figure 2.2 there is an example of how a velocity set looks like for one lattice unit.

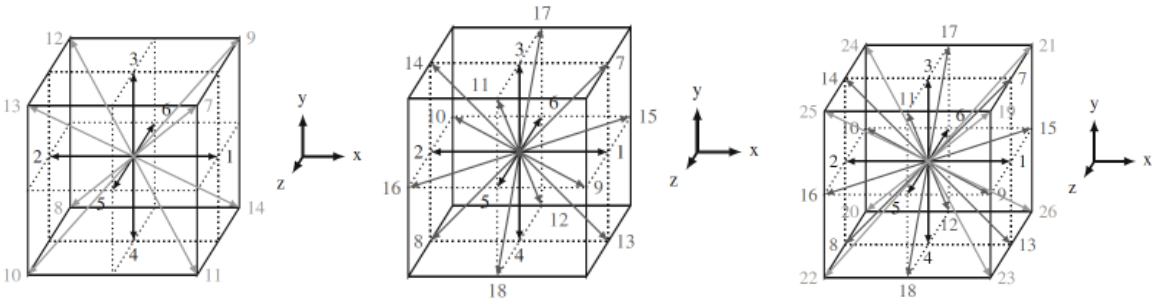

(a) D3Q15 (b) D3Q19 (c) D3Q27

Figure 2.2: 3D Lattice Boltzmann velocity sets of D3Q15, D3Q19 and D3Q27 [42]

If Figure 2.2 is taken as an example. For a 3D problem, it is important to consider a scheme that is most suitable for the situation. Evidently, D3Q15 is more computationally efficient than D3Q19 and which in turn is more efficient than Q3D27. Q3D27 requires 40% more memory and computing power than D3Q19 [42]. As a result of more freedom in motion, the computational efficiency will decrease, It has to be kept in mind that with smaller velocity sets it is harder to capture some flow phenomena. In the papers of Kang and Hassan [35], Suga et al. [74], White and Chong [83] is mentioned that D3Q27 is a better choice to use for simulating high Reynolds number turbulent flows, whereas D3Q19 is a good compromise for laminar flows.

2.3. Structure of *OpenLB* Algorithm

The general functioning of the *OpenLB* code follows a generic path. The LBM structure is implemented in the code and gives a good overview of how the code works step by step. Figure 2.3 provides a concise flow diagram of step by step approach, which will be the guideline for the remainder of the chapter.

2.3.1. Non-dimensionalisation and choice of the relevant simulation parameters

Representing the physical properties in the lattice of an LBM simulation and vice versa is crucial to obtain a valid model that corresponds to the true physical behaviour of fluid flow phenomenon. LBM simulations are performed in lattice units where all the physical properties are represented by non-dimensional numerical values. *OpenLB* has a build in unit converter where the input variables are both converted into the physical unit, lattice units, but also into conversion factors which are an important bridge between the worlds. Nonetheless, LBM simulations require a good understanding of how unit conversion essentially works. Due to inherent constraints of the Lattice Boltzmann Method, it is essential to find an equilibrium for the simulation parameters in a manner that a suitable trade-off of accuracy, stability, and efficiency is accomplished.

The conventional steps that need to be taken in order to convert from the known physical values to lattice units is a twofold approach. First, the physical system is converted to a dimensionless system and is independent of the original physical scales, but also does not depend on the simulation parameters. The second step is to advance from the dimensionless system to discrete simulation parameters. The coherence between the physical, dimensionless and the lattice system is made possible by the scale-independent numbers. The solution to a conventional incompressible Navier-Stokes problem is dependent only on one scale-independent number, the Reynolds number respectively. Here applies the Law of Similarity[44], which states that: two incompressible flow systems are identical in a dynamical sense if they have the same Reynolds number and geometry. This means that in the three mentioned systems, physical, dimensionless and lattice, the Reynolds number must be the same. The transition from the physical to non-dimensional scales is accomplished by choosing a characteristic length and time scale.

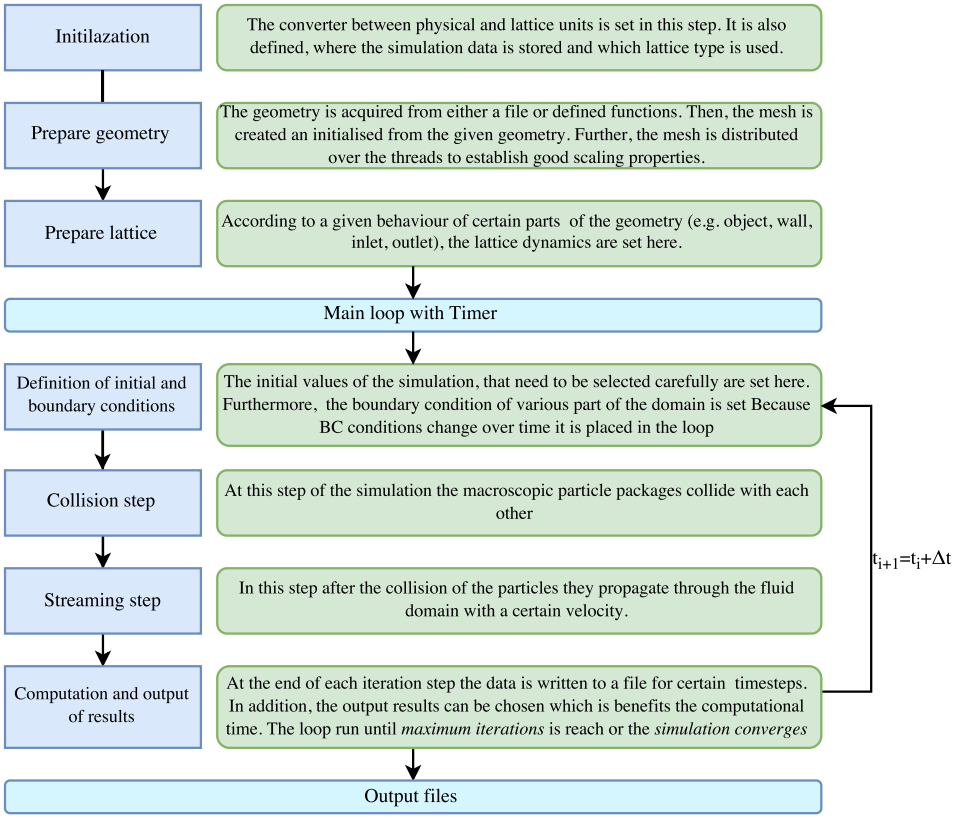

Figure 2.3: Flow diagram of the LBM code, inspired on[41]

$$\text{Physical system} \overset{Re,l_0,t_0}{\Longleftrightarrow} \text{Non-dimsional system} \overset{Re,\delta_x,\delta_t}{\Longleftrightarrow} \text{Lattice system}$$

The step from the physical to lattice scale can be performed in one go, however, it is encouraged to take the intermediate step for several reasons. The primary reason is that the discrete values of space, δ_x, and time, δ_t, are crucial for the stability and accuracy of the simulation[46]. These values do not depend on the physical system and more importantly, they do not depend on the arbitrary chosen physical units. Non-dimensionalisation is achieved by dividing the physical scale by a selected quantity that is of the same dimensions. The resulted value is referred to as lattice scale or lattice unit. The selected value to non-dimensionalise the physical scale is called the conversion factor. Let us denote the conversion factor by C, and lattice units by a star *, similar to [42]. For a given length, l, the conversion can be written as:

$$l^* = \frac{l}{C_l} \tag{2.8}$$

However, this feature of conversion and choosing the appropriate value is built-in in the *OpenLB* code. *OpenLB* has a minimum set of mandatory parameters in order to start a simulation, in Table 2.1 the mandatory set of parameters is shown. This is only one example of a converter that can be used within *OpenLB*, where the key parameters are resolution and relaxation time. Other converters use a combination of a certain key parameter such as: relaxation time, mesh resolution, lattice velocity and many more.

Some of the simulation parameters that are chosen are grid size, velocity, density, viscosity and relaxation time parameter. In *OpenLB* the Reynolds number is chosen and with that, the kinematic viscosity is calculated with the given velocity and characteristic length. The characteristic velocity in the lattice is set to well below the compressibility limit since LBM simulation is not yet accurate enough for high Knudsen number or incompressible flows. The expression of the Knudsen number in lattice quantities is given in Equation (2.9). The limit is related to Mach number which is a ratio of the speed of sound and the lattice velocity, as shown in Equation (2.10). In the physical space incompressible flow ends around Mach 0.3, however, this is different at the lattice scale where the speed of sound C_s is constant and equal to the density variation over the pressure variations [45], Equation (2.11).

$$Kn = \frac{\Delta x}{l} = \frac{1}{l^*} \tag{2.9}$$

$$Ma^* = \frac{U^*}{c_s^*} \tag{2.10}$$

$$c_s^* = \frac{1}{\sqrt{3}} \tag{2.11}$$

Table 2.1: *OpenLB* mandatory input variables

Variables	Symbol	Unit
Resolution	N	[-]
latticeRelaxationTime	τ	[-]
charPhysLength	charL	[m]
charPhysVelocity	charU	[m/s]
physViscosity	ν	$[m^2/s]$
physDensity	ρ	$[kg/m^3]$
pressureLevel	p	[Pa]

This is a standard quantity that is used in general LBM simulations[42]. To operate in the quasi-incompressible flow limit, all the simulated velocities should be significantly lower. In practice this means that the lattice velocity should be around or under $U^* = 0.2$ [42]. Additionally, the relaxation time parameter, τ, depends on the compressibility limit of the speed of sound. For a Single Relaxation Time (SRT) model the chosen relaxation time is applied in the whole domain and also depends on the kinematic viscosity, as is illustrated in Equation (2.4). But can also be expressed as follows:

$$\nu = c_s^{*2}\left(\tau^* - \frac{1}{2}\right)\frac{\Delta x^2}{\Delta t} \tag{2.12}$$

The kinematic viscosity is a consistency equation with three simulation parameters, τ, Δx and Δt, from this expression it can be established that these parameters are not independent of each other. Only two of these parameters can be chosen freely at the start of an LBM simulation. To comply with the Law of Similarity the Reynolds number needs to be accounted for when choosing one of these simulation parameters.

2.3.2. Geometry and Lattice Initialization

The built-in application in *OpenLB* for generating geometries is a powerful one. There is an option to load a Stereo-lithography (STL) file and generates a uniform mesh. However, there are also functions to create more generic geometry such as cuboids, cylinders, and spheres. A step by step example of how the application works are illustrated in Figure 2.4. The example shows a complex geometry which is converted into a lattice geometry. This fully automated generation of the lattice geometry shows the high user-friendliness of the code.

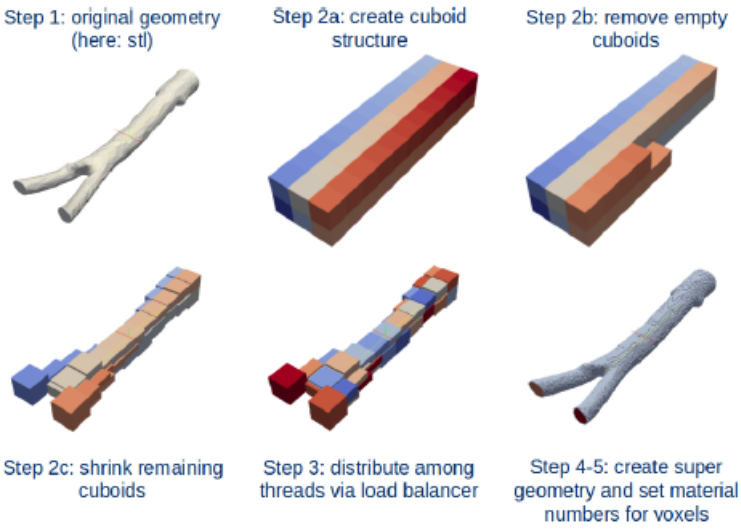

Figure 2.4: Steps *OpenLB* takes to create a geometry. It converts an STL file into voxels [41]

Representing a geometry in *OpenLB* is a very general approach. A specific number named *material number* is assigned to each cell in the entire domain. With these material numbers the cells that represent boundaries, fluid domains or superfluous areas can be set for computation. Moreover, after the material number is assigned to a cell, different collision and streaming steps, but also the fluid behavior and boundary condition, can be appointed with respect to the material number. The major advantage of using material numbers in flow simulation is the fully automated determination of the fluid direction on each boundary node, this is especially for complex geometries often a cumbersome job to perform by hand.

In order to analyze novel problems, such as turbulent flows in combination with curved geometries must be represented appropriately in an LBM simulation. The only problem with this is that the lattices are quadratic. This means that either the resolution of the geometry must be very high, which in turn would still lead to a staircase approximation, or the outline must be adjusted accordingly [57]. In literature there are a few common methods for representing a complex geometries that are based on body fitted grids [28–30], immersed Boundary Methods[33, 60, 90], inter- extrapolation methods [21, 53, 54]. Nevertheless, *OpenLB* mainly uses an interpolation method proposed by Bouzidi et al. [6] and validated by Kao and Yang[36].

2.3.3. Definition of Initial Conditions

In conventional discrete numerical methods, when solving the Navier-Stokes equation, the initial condition is specified by the velocity at $t = 0$ which is the same as a non-time-dependent solution, steady state. There is a more general step which is called initialization, which is not the same. The two vary in how things are defined. The initial condition is set by physics of the problem, for instance, they only apply for time-dependent problems. Initialisation step is required even when the problem is steady-state because the simulation must not start with random values filling the memory[42]. Therefore, initialization is always a step that is taken in numerical simulation.

In LBM this plays a vital role in how to take the first steps in obtaining a correct simulated solution. In a typical CFD simulation of incompressible flow the velocity, density and pressure are the initial condition variables. However, this is not adequate for an LBM simulation, since certain values must be assigned to the distribution functions. An approach is to set the local initial distribution function, f_i equal to the corresponding equilibrium distribution, f_i^{eq}, this can be obtained from Equation (2.3) given the density and velocity term.

2.3.4. Boundary Conditions

The impact of boundary conditions on the overall solution must not be underestimated, even though it applies to a small part of the fluid domain it has a considerable influence. Hence, boundary conditions must be treated with the utmost care. In LBM the boundary condition are applied to nodes that are both linked to a fluid and solid node. Instead of defining the macroscopic variables such as density and velocity, LBM boundary conditions apply to mesoscopic population f_i in Equation (2.1). This gives more degrees of freedom and rise of a non-uniqueness of the problem [42]. The collection of LBM boundary conditions can be divided into two major groups: *linked-wise* and *wet-node*, the two perspectives of domain discretization methods can be seen in Figure 2.5. The main difference with conventional numerical methods lies in the fact that the order of accuracy and exactness are not equal. An example of this is that a second-order scheme does not produce an exact parabolic solution. The best example of a *link-wise* scheme is the Bounce-Back method which will be discussed in more detail later in this section.

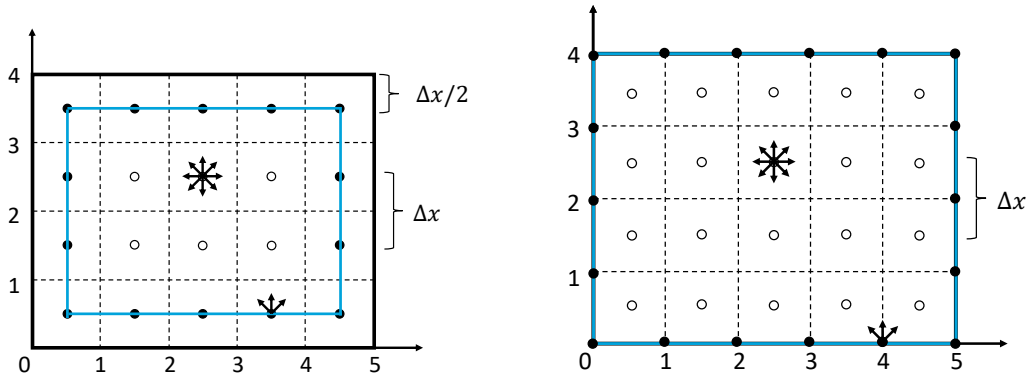

(a) link-wise (b) wet-node

Figure 2.5: Different methods of discretisation of the same domain. The blue line is the computational boundary and the black line the physical boundary. Fluid nodes are illustrated with open circles (○), boundary nodes as solid circles (•), inspired by [42]

Periodic Boundary Conditions

From the large selection of boundary conditions, this is one of the simplest that can be implemented. Periodic boundary condition applies only to a situation where the flow solution is periodic, here the edge nodes behave as if they were attached to the nodes on the opposite side of the domain. Consequently, this boundary condition complies with the conservation of mass and momentum at all times. A noteworthy aspect of this boundary condition is that a fully periodic flow solution is physically not possible due to the fact that it would use the entire known space. Nonetheless, the application of a periodic boundary condition is justified in certain cases where a finite part of the flow can be approximated by a recurrent pattern. The classical Taylor Green vortex is a great example where a periodic boundary condition can be applied. It is the simplest flow where the turbulent energy cascade can be observed numerically. Starting initially from a single turbulent length scale and quickly dissipating into a full turbulent spectrum in a very periodic manner. Due to the periodic, isotropic nature of the flow, it is very suitable for a periodic boundary condition

Bounce-Back Boundary Conditions

The working principle of the Bounce-Back (BB) boundary condition boils down to the fact that, if particle populations hit a rigid wall during diffusion they will be bounced back to the pre-impact location. The BB boundary condition is also known as the no-slip boundary, where the velocity at the wall is zero. The no-slip boundary follows from the bounce back property of the wall, which makes it impenetrable for fluid. Moreover, there is no flux across the wall boundary and the fact that the particle population is reflected back and not forward leads to that there is no cross motion between wall and fluid, hence no-slip condition. Despite the simple explanation of the boundary condition it should not takes to literally. A more complete explanation of the macroscopic behaviour of the boundary condition can be performed with e.g. Chapman-Enskog analysis[9].

As discussed in the introduction of Section 2.3.4, a distinction can be made of how the computational and the physical boundary is defined. This also applies to the Bounce-Back boundary condition.

There are two ways in how Bounce-Back method can be accomplished:

1. First approach is the *fullway bounce-back* [75]. Here the particle population travels the complete patch from the fluid node to the solid node, where the wall is somewhere in the middle between these nodes. The velocity is inverted in the collision step as can be seen in Figure 2.6. This can be categorizes as part of the *wet-node* group.

2. Another approach is called the *halfway bounce-back* [43]. The particle population only travels half the distance between the nodes. The inverse velocity is a part of the streaming step as illustrated in Figure 2.7, as with the *link-wise* boundary condition group.

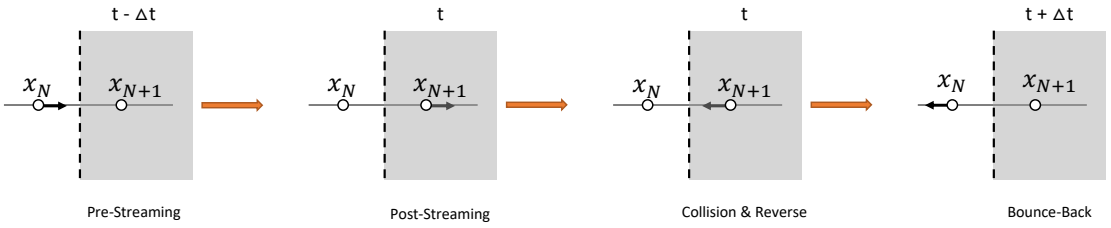

Figure 2.6: Illustration of fullway bounce-back BC. The arrow represent the particle population, the grey shaded area is the solid domain and the dashed line is the wall boundary

Regardless of the names of both methods, both the fullway and the halfway approximate the boundary to be positioned at the midpoint between the two nodes, And it is actually not situated on the solid node.

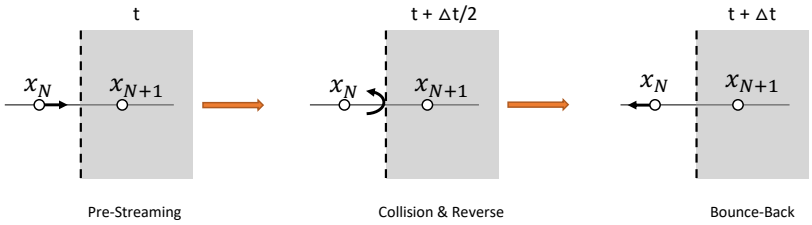

Figure 2.7: Illustration of halfway bounce-back BC. The arrow represent the particle population, the grey shaded area is the solid domain and the dashed line is the wall boundary

Bouzidi Boundary Condition

The Bouzidi-Firdaouss-Lallemand [6] approach for velocity boundary conditions for curved boundaries is a very elegant way of using the most out of the simplicity of the Bounce-Back(BB) boundary condition and improving it. This boundary condition is a well-known part of the *link-wise* group. Bouzidi et al. [6] starts with the simple BB and interpolates the values of particle population that needs to be propagated to the position of the fluid particles to which the standard BB would stream it to. Using interpolation techniques, within the LBM framework, to represent an arbitrary surface is challenging because the post-propagated state of the fluid next to the wall needs to be evaluated within the discrete time step. The evaluation is needed since the information of the post-collision state is used for the interpolation. The described method of Bouzidi et al. [6] is illustrated in Figure 2.8. To reconstruct the properties at node A, a linear interpolation method is proposed. In the paper of Bouzidi et al. [6] they present two variations, one with linear interpolation and the other with quadratic interpolation. Bouzidi et al. [6] claim that both methods are second-order converging, however, the linear method has a poorer prefactor. The factor q in Figure 2.8 and Equation (2.13), describes the ratio of the length between the nearest fluid cell and the wall w.r.t. the lattice size.

$$q = |AC|/|AB| \tag{2.13}$$

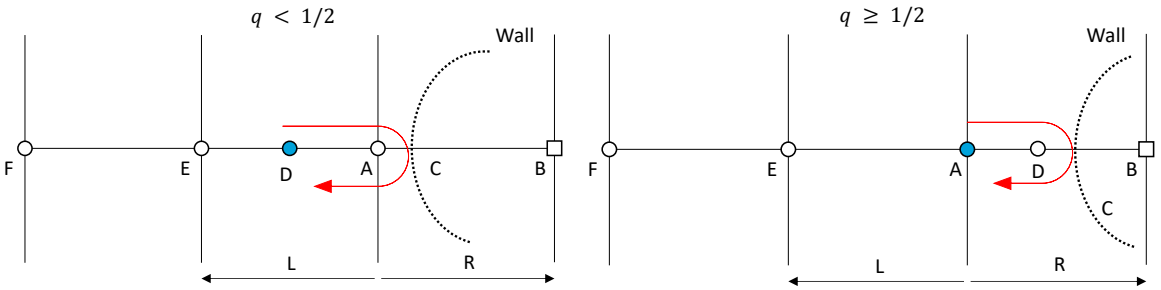

(a) Normalized distance $q < 1/2$ (b) Normalized distance $q \geq 1/2$

Figure 2.8: Particle population state representation based on distance between the solid boundary and the fluid nodes [6]

On Lattice Boundary Conditions

On lattice boundary conditions are in principal boundary nodes that are assigned with a specific role. The roles are the boundary conditions at which these nodes are applied to in the lattice. Here is an overview of the applicable boundary condition, within *OpenLB*, on straight walls. These boundary conditions are clear and detailed described by Latt et al. [48], however, a short summary of each boundary condition is given for completeness. It must be said that all the boundary conditions in the short summary are a part of the *wet-node* group.

- **Inter Boundary Condition:** A boundary condition with finite difference approximations is introduced by Skordos [69]. This is the only boundary condition that violates the base principle of LBM, locality. It is known that the off-equilibrium part of the particle population is dependent on the velocity gradient. Instead of obtaining the particle populations information through a known node, the method interpolates the information by accessing neighbouring nodes and using a finite difference scheme. This makes the method very robust and ideal for high Reynolds numbers.
- **Regularized Boundary Condition:** The method developed by Latt and Chopard [47] replaces all the particle population, known or unknown. The local values of the stress tensor are deducted from the known particle population. Next step is that this information is then used to attribute the value of the regularized LB method to all particle population. The method is less accurate at low Reynolds numbers but is strong at high Reynolds numbers, only the non-local BC is better.
- **Inamuro Boundary Condition:** With the method of Inamuro et al. [34], only unknown particle populations are replaced. This is initiated at an equilibrium distribution with set density and a velocity which is shifted by a slip-velocity parallel to the wall. The implementation of the method is simple and very accurate in 2D cases, however, has his shortcoming at high Reynolds numbers.
- **Zou/He Boundary Condition:** Similar to Inamuro et al., the Zou and He [91] also replaces the unknown population particles. The same shortcoming and strengths are with this boundary condition implementation as with Inamuro BC. The only difference with this method is that a bounce-back scheme is applied to the off-equilibrium particle population.

2.3.5. Collision & Streaming step

The concept of LBM is a simple one. There are two parts that are fundamental to the method and those are the *Collision and Streaming* steps. Collision step is an algebraic local operation. In this step first the density and the macroscopic velocities are calculated to determine the equilibrium distribution equation f_i^{eq} as in Equation (2.3) and the post-collision distribution f_i^* as in Equation (2.6).

After the collision step is executed the next step is the streaming step, at this point, the resulting distribution f_i^* is streamed to the neighboring node, as in Equation (2.7).

2.4. Collision Operators

The collision step is a local algebraic operation which has multiple possible methods to perform this action. The first and currently widely used is the Bhatnagar, Gross, and Kook (BGK)[5] operator which only uses a single relaxation time. There are many other operators that are based on the BGK and they will be elaborated in this subsection. Besides the BGK with his single relaxation time operation, there are more, the two other

widely used operators are Two-Relaxation Time (TRT) and Multi-Relaxation Time (MRT), these are an extension on the simple BGK scheme or more accurately BGK and TRT are a special case of MRT. Due to the relative newness of LBM, there are a lot more operators available nowadays, each with his own purpose, however, we will limit ourselves to the three mentioned operators.

2.4.1. BGK: Single-Relaxation Time

The BGK model original purpose was to describe the essential physics of molecular interaction, where the relaxation time τ is chosen as the molecular collision time. The most important aspect of the collision operator is to apply to the conservation laws of mass and momentum. A simple collision operator, as the BGK, can be written as a linear function of the equilibrium function Equation (2.3) and the collision term Equation (2.6). Equation (2.5) is already a discretized form with the BGK collision operator applied, to see how this final form is reached and to explain what all the term mean a more detail description is given. Starting with the first-order discretized form of the LB equation:

$$f_i(\mathbf{x}+\mathbf{c}_i\Delta t, t+\Delta t) = f_i(\mathbf{x}, t) + \Delta t\Omega_i(\mathbf{x}, t) \tag{2.14}$$

where Ω_i the collision operator is. In this case the BGK operator, which is described in Equation (2.2)

$$\Omega_i = -\frac{f_i - f_i^{eq}}{\tau}$$

The physical interpretation of Equation (2.2) is, that the population f_i has a tendency to move in the direction of f_i^{eq} to reach a certain equilibrium state after time τ. This is often called the relaxation towards equilibrium, and τ, as mentioned before, is the relaxation time towards that equilibrium. Substituting Equation (2.2) into Equation (2.14) gives Equation (2.5). This very rudimentary approximation of the original LBE with the BGK operator gives strangely very good results in most cases. It is able to reproduce the continuity and the Navier-Stokes equation, that is its strength and reason of LBM's popularity.

Relaxation time has a major influence on the stability of the simulation. Although the population f_i has a tendency to move towards f_i^{eq} it does not mean it will, directly. There are three way how the propagation of f_i progress to f_i^{eq}. These three ways are, Under-Relaxation, Over-Relaxation and Full-Relaxation, depending on the choice of $\tau/\Delta t$. Moreover, there is the fourth case and that is where the simulation is unstable. Below a list of all conditions for every case is summarized and illustrated in Figure 2.9 .

- **Under-Relaxed** for $\tau/\Delta t > 1$, the population f_i is propagation toward f_i^{eq} exponentially
- **Over-Relaxed** for $1/2 < \tau/\Delta t < 1$, the population f_i is oscillating around f_i^{eq} with an exponentially decreasing amplitude
- **Full-Relaxed** for $\tau/\Delta t = 1$, the population f_i propagating directly to f_i^{eq}
- **Unstable** for $\tau/\Delta t < 1/2$, the population f_i is oscillating around f_i^{eq} with an exponentially increasing amplitude

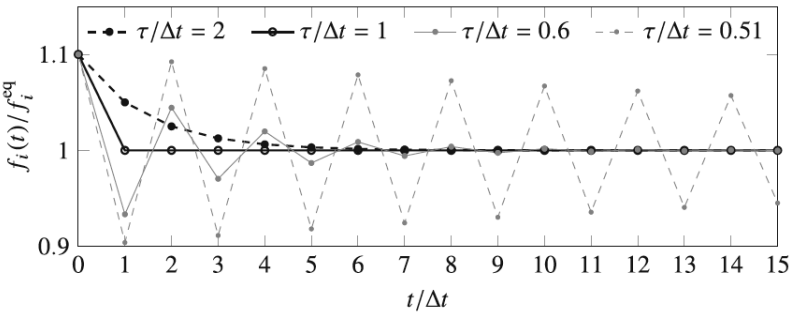

Figure 2.9: Example of Under-Relaxed, Over-Relaxed and Full-Relaxed for a homogeneous lattice in Equation (2.5) [42]

It shows that no matter what $\tau/\Delta t > 1/2$ must be true otherwise there is no converging solution.

2.4.2. MRT: Multi-Relaxation Time

BGK collision operator has his limitation under certain condition. At high Reynolds numbers, BGK shows some stability issues. To avoid the increase in mesh resolution and therefore the computational cost of a different approach is needed. The general approach to solve this stability and accuracy problem is applying the MRT scheme. Although, the shortcoming of BGK are solved MRT has his own drawbacks. The general idea of MRT is to map the particle population into a moment space by mean of a transformation matrix. This allows moments rather than populations to be relaxed with individual rates. A relaxation matrix is applied to this moments to relax them to an equilibrium state. The relaxed moments are transformed back to particle population space where the streaming step can be performed as usual. How the transformation matrix is constructed is rather elaborate and consist of multiple theories with different approaches to solve the problem and beyond the scope of this thesis.

The advantage of MRT is that each particle population has an individual relaxation rate that moves the population to the local equilibrium. This local operation is more tailored made approach rather than the BGK scheme where one size, fits all. The disadvantage of the custom-made solution is the shear amount of parameters that need to be tuned to reach a far better accuracy and stability, which also requires more time.

2.4.3. TRT: Two-Relaxation Time

The Two-Relaxation Time (TRT) scheme combines the algebraic simplicity of BGK and the improved stability and accuracy of MRT, best of both worlds. The degrees of freedom of MRT maybe large and unclear for many, it is often not clear how to tune the parameters of MRT to achieve better stability and accuracy. TRT only requires two relaxation states. The first relaxation time is dependent on the shear viscosity and the other is a free parameter. TRT can overcome the problem of BKG's accuracy error only is dependent on one value, the relaxation rate ω. Relaxation rate is the rate at which the particle population progresses to its equilibrium state. To better understand how TRT is more capable of dealing with the shortcoming of BGK scheme, first of all, the weakness of BGK needs to be pinpointed.

The weakness of BGK has to do with numerical errors that the simplicity of the method causes. The spatially second-order accurate and first order in time, which is proportional to $(\tau - \Delta t/2)^2$ and τ, respectively. The viscosity is dependent on the relaxation time, therefore making the error dependent on the viscosity. With the BGK scheme to achieve consistent errors with varying relaxation time's, various parameters need to be adjusted to accomplish this. This is in contrast to the TRT collision operator, where the accuracy is dependent on a combination of two relaxation parameters, ω^+ and ω^-. There is a parameter that helps to choose the right values of both relaxation rates.

$$\Lambda = \left(\frac{1}{\omega^+ \Delta t} - \frac{1}{2}\right)\left(\frac{1}{\omega^- \Delta t} - \frac{1}{2}\right) \tag{2.15}$$

Controlling the accuracy and stability of the simulation is drastically simplified. Choosing a constant value for Λ while changing the viscosity through adjustment of ω^+ and changing the corresponding ω^- to match the values of Λ is more simple and accurate way to choose the right parameters for the simulation.

2.5. Turbulence Modeling: Large-Eddy Simulation

Most problems in real life of a practical importance have a far to high Reynolds number to be a subject to direct simulation. This makes it challenging to predict the high turbulence behavior of flow at these high Reynolds numbers without simulating all scales of motion. Turbulence is a topic of intense research, especially how to model turbulence and Sub-Grid Scale (SGS) modeling. A powerful leading idea behind the SGS is the concept of eddy viscosity. The theory assumes that the effect of the small scales on the large scales can be linked to diffusive motion caused by a random collision. Small eddies are kinematically transported without distortion by the large ones, the large eddies experience diffusive motion from jerk collision with the small eddies[72]. The energy transport from the larger eddies to the small ones is also called the energy cascade and is a basic idea of Large Eddy Simulation (LES). A popular method to model the eddy viscosity for SGS is the Smagorinsky [70] model, the popularly comes from the simplicity of the model.

The inherent nature of the Lattice Boltzmann Method guides the choice of turbulent models. The nature of LBM being time-dependent, local, on a basis of a distribution function and cheaper in computational cost compared to continuum approach. With the latter meaning that a finer mesh can be used for the same computational cost. This has a benefit that unresolved scales can be restricted to smaller scales, which are more universal and therefore a simpler model can be used. This last argument has led a lot of researchers to

explore LBM in combination with LES. Encouraging results are obtained by Krafczyk et al. [39], Malaspinas and Sagaut [51, 52], Nathen et al. [57], Sagaut [66]

However, there are some unanswered problems within the general LES framework as Rodi et al. [65] describes. One of which includes the sub-grid model determination, or adaptive mesh regulation to achieve a locally fine grid to model the unresolved scales, but also how to appropriately determine the wall model and boundary conditions. Furthermore, a fully three-dimensional time-dependent simulation is required, the consequence of this that it requires a large number of computational resources. While these are problems that need to be solved, it is important to make LBM useful with the current tools available. Teixeira [76], among others, presents a solution to the problem of simulating high Reynold number flows. The approach is simple in the sense that is using a standard two-equation model, k-ϵ model. The only change that is made is to the fluid algorithm is the computation of the viscosity. With the presence of the eddy viscosity term, the total viscosity becomes a dynamic term.

Nonetheless, the availability of such a method or function is not present in *Openlb*. The program only deals with LES based turbulence models or other LBM based turbulence models. As stated by Malaspinas and Sagaut [52], "It appears that subgrid closures within the lattice Boltzmann method (LBM) framework are almost exclusively limited to eddy viscosities models", that is more or less the philosophy of the *Openlb* developers. Therefore, a brief overview of the LES equations are mentioned and a handful of Smagorinsky based methods available within *OpenLB* are considered in the next section.

Smagorinsky Models

The most popular method to model the eddy viscosity for SGS is the Smagorinsky [70] model. The formulation of Smagorinsky's eddy viscosity model is as follows:

$$\nu_{SGS} = C_S^2 \Delta^2 |\overline{S}_{ij}| \tag{2.16}$$

where C_S is called the Smagorinsky constant, Δ is the mesh size and the filter width. The filter width is a threshold value and point from where the unresolved grid scales are modeled. This describes the classical model that is developed by Smagorinsky, although developed in the sixties the method is still broadly used. The strain tensor ($\overline{S}_{ij}$) in Equation (2.16) can be obtained locally from the non-equilibrium moments, making the implementation even more straightforward than in conventional CFD [72]. Nonetheless, it has his flaws and shortcomings so that is why a large group of researchers took on the task to improve the model. In the list below a selection of improved Smagorinsky based methods, that are available within the *OpenLB* framework, are elaborated.

- **Shear-Improved Smagorinsky Model:** This model improves the too dissipative nature of the original Smagorinsky model with respect to the resolved motions in the near-wall region, this due an arising of excessive eddy-viscosity from the mean shear [50]. The proposal to alleviate the deficiency from the original model, by Lévêque et al. [50], is to introduce the following adjustment to the eddy viscosity formulation

$$\nu_{SGS} = C_S^2 \Delta^2 \left(|\overline{S}_{ij}| - \left\langle |\overline{S}_{ij}| \right\rangle \right) \tag{2.17}$$

  The magnitude of the mean shear $\langle|\overline{S}_{ij}|\rangle$ is subtracted from the magnitude of the resolved rate-of-strain tensor $|\overline{S}_{ij}|$.

- **Consistent Smagorinsky Model:** The model proposed by Malaspinas and Sagaut [52] is a consistent way of introducing SGS closure within the BGK dynamics of the LB equation for large eddy simulation. A link between the proposed approach and the standard way of incorporating the eddy viscosity term into LBM is established. By introducing an additional local turbulent relaxation time that includes the eddy viscosity term. The modification of the relaxation time locally holds as long as the Chapman-Enskog expansion commutes with the subgrid filtering procedure. The paper of Malaspinas and Sagaut [52] shows how to include consistently existing Navier-Stokes models in LBM with BGK dynamics.

- **Approximate deconvolution model (ADM):** The approach of Malaspinas and Sagaut [51] is based in the Approximate Deconvolution Method(ADM) of Stolz and Adams [71]. Similar to the Consistent Smagorinsky Model, Malaspinas and Sagaut try to implement an existing Navier-Stokes turbulence model into the LBM framework. The discrete Boltzmann equations are filtered and subsequently deconvoluted with a regularized inverse filter operation in order to reconstruct the proper macroscopic

equations for LES within the kinetic theory [58]. The ADM implementation of Malaspinas and Sagaut [51] is based in the BGK collision operator, however, it can be extended to other collision operators, with the note that every collision operator has a different approach to stability and accuracy which has to be accounted for.

2.6. Limitations of *OpenLB*

The nature of *OpenLB*, being a relatively new open source tool, has his limitations on what type of problems the tool can be applied on. In this section a few essential limitations of the tool are summarized, but also the importance of solving these limitations are discussed.

- **No wall model:** Flow close to a wall is inherently different from flow in the far field. To accurately analyze the aerodynamic efficiency and to capture the essential boundary layer behavior of a body in the flow a wall treatment model needs to be introduced. Wall function is used to bridge the gap between the inner layer and the fully developed turbulent outer layer. Using a wall function approach diminishes the need for resolving the boundary layer, resulting in a significant reduction of mesh size and a decrease in computational time. However, due to the equal voxel size used, within *OpenLB*, across the entire fluid domain leads to an unnecessarily large amount of cells. This consequently has an influence on the computational time en resources. Hence, commercial software packages include a wall function to model the flow close to the wall instead of simulating it, accomplishing a computationally efficient simulation.

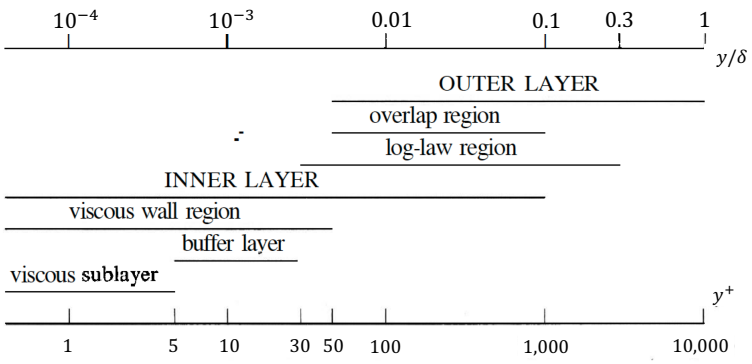

Figure 2.10: The various layers of turbulent boundary layer profile at a moderate Reynolds number of $Re = 10^4$ [64]

To understand the importance for such wall model the various layers that are present in the boundary layer are examined more in-depth. An important parameter, when considering wall-bounded flow, is the non-dimensional wall distance y^+, which is defined as:

$$y^+ = \frac{yu^*}{\nu} \tag{2.18}$$

Based on this non-dimensional wall distance the boundary layer can be dived into several layers, with each layer representing a different flow characteristic. All the layers that are in a turbulent boundary layer are illustrated in Figure 2.10. The region close to the wall is the inner layer where $y^+ < 50$, in this layer the viscous effects govern the flow characters. One step closer to the wall where $y^+ < 5$ is the viscous sub-layer where the Reynolds shear stress can be neglected compared to the viscous stress. In this layer, the flow is almost linear, as is the velocity profile according to the law of the wall [64]. An accurate representation of the inner boundary layer determines a successful prediction of the wall-bounded turbulent flows.

- **No local grid refinement:** The absence of a local grid refinement function in *OpenLB* is a fundamental limitation of the tool. With local grid refinement, sections of interest in the fluid domain can have smaller voxel sizes which not only capture essential flow phenomenon but also significantly reduce the number of voxels needed to discretize the domain. This also has an effect on how detailed the imported

models could be. If a very detailed truck model with mirrors, side flaps, undercarriage and other small parts on a truck is imported, *OpenLB* gives an error and a warning that the small parts on the model could not be modeled because of a too coarse mesh. For the current used GETS model this not the case due to the generic shape.

- **Use of LES for turbulence modeling:** Large eddy simulation is a field of study that is very heavily investigated in the last couple of decades. Considerably amount of progress is made due to the increasing computational power, however, it is still limited to relatively low Reynolds number flows. This is, even more, the case for LES used in Lattice Boltzmann Methods, where the progress is lacking behind on the SGS models based on the Navier-Stokes(NS) based methods. Nonetheless, due to the easy implementation of the SGS models in the LBM the conversion from NS to LBM is getting better and faster. Application of LBM for high Reynold number cases is an important step to make, not only *OpenLB* but LBM in general, useful for the aerospace or automotive industry.

2.7. Validation with Literature

In this section, various cases of numerical simulation are performed to validate the *OpenLB* code. The validation cases are laminar flows. A 2D square cylinder is simulated at Reynolds number varying from 50 to 300. The drag and velocity profiles are compared with literature. Also, a 3D round cylinder is simulated and compared with literature. The maximum drag, lift and the pressure drop over the cylinder are obtained.

2.7.1. Laminar Flow Simulation Around a 2D Square Cylinder with *OpenLB*

To validate that the open source code and the application of boundary condition for an MRT collision model a 2D square cylinder is used. The drag coefficient and velocity profiles of the 2D square are compared for various Reynolds numbers for a laminar flow. The results obtained are compared to Breuer et al. [7] and Nathen et al. [57]. Both authors described an average drag coefficient in a channel flow with a height $H = 8D$ and a length of $L = 50D$, where D is the diameter of the cylinder in question and has a reference length of $D = 1$. In Figure 2.11 a schematic drawing of the geometry and domain is shown. The blockage ratio was fixed at B =1/8. The length of the channel is chosen is such to reduce the influence of the inflow and outlet boundary condition. Breuer et al. [7] compared an FVM and an LBM, where the position of the cylinder in the FVM case was fixed at $l = L/4$, however, in the LBM case, the position of the cylinder was varied between $l = L/3$ and $l = L/4$ to investigate the influence of different inflow and outflow conditions. Nevertheless, only a slight divergence of the results was found.

Authors use different numerical approaches for the boundary conditions, Nathen et al. [57] imposes a laminar velocity inlet profile and a pressure outlet condition. The upper and the lower walls are prescribed as a bounce-back boundary condition. The drag coefficient was obtained via a momentum exchange method, which is an intrinsic way of evaluating the forces on solid boundaries within LBM.

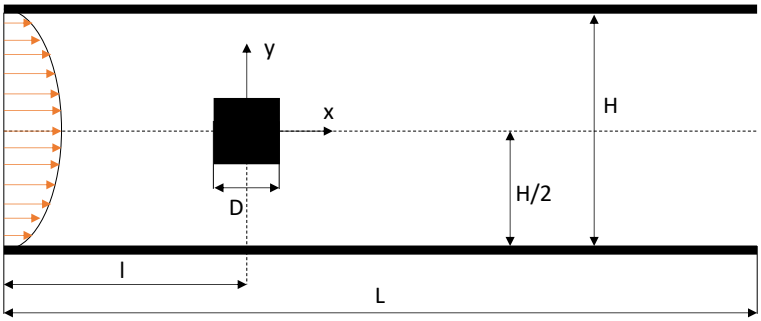

Figure 2.11: Definition of geometry and integration domain, inspired on [7]

In fig. 2.12 the result obtained with the present study is compared to the LBM and FVM results of Breuer et al. [7] and LBM results of Nathen et al. [57], which also uses *OpenLB*. The results of the present study and that of Nathen et al. [57] use an MRT collision scheme combined with complex boundary treatment discussed earlier. The spatial resolution of all the simulations is identical. All the LBM results have 40 voxels for the reference length of the cylinder and 42 voxels for the FVM simulation.

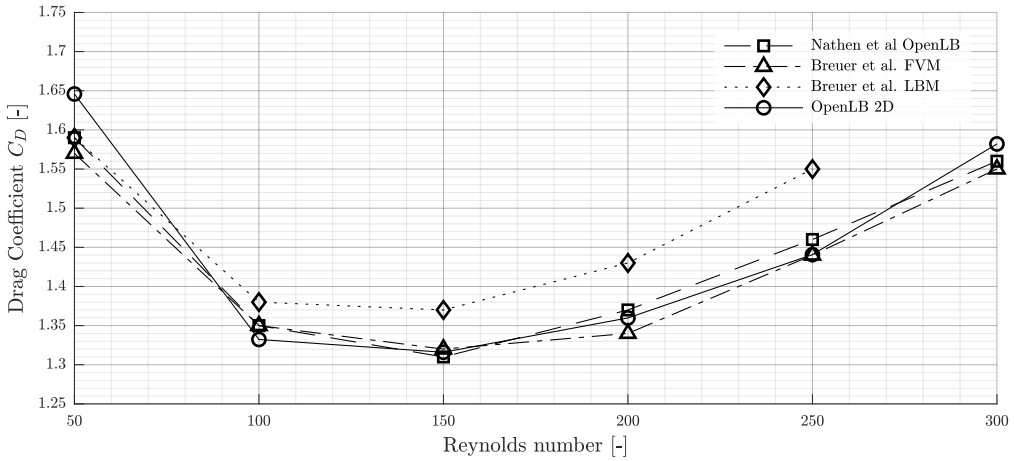

Figure 2.12: Comparing drag coefficient (C_D) at various Reynolds numbers with Breuer et al. [7] & Nathen et al. [57], performed both with LBM and FVM

The drag difference between the simulated results and literature are shown in Figure 2.13 and given in Table 2.2. The largest difference in drag is with the LBM of Breuer et al. [7]. The values diverge with increasing Reynolds number. When the simulated values are compared to Nathen et al. [57] and the Finite volume method of Breuer et al. [7] there is a better agreement in drag, especially between Re=100 and 250. The large difference between the obtained results and the LBM results of Breuer et al. [7] could be the cause of different boundary conditions that are applied in the cylinder.

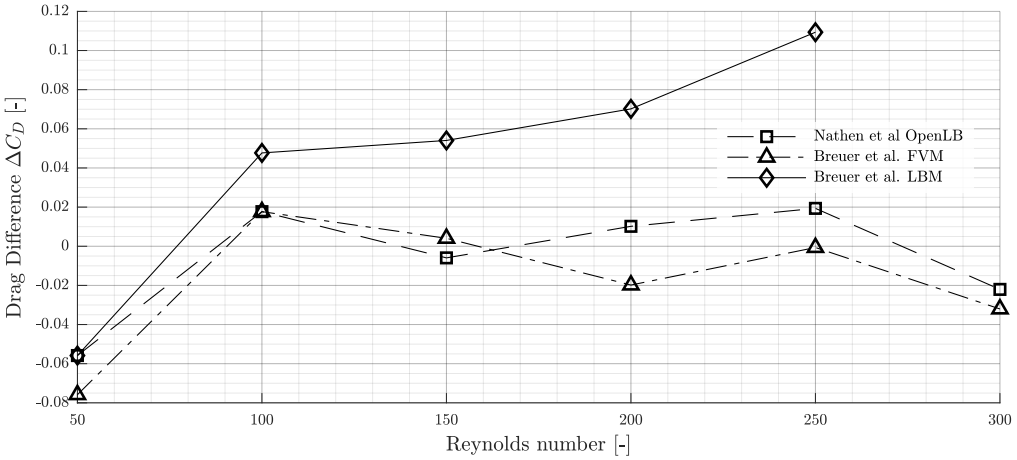

Figure 2.13: Drag difference (ΔC_D) at various Reynolds numbers subtracted from Breuer et al. [7] & Nathen et al. [57]

Table 2.2: Drag difference between the *OpenLB* simulation of 2D square cylinder and literature

	Drag Difference ΔC_D **[-]**					
Run	Re=50	Re=100	Re=150	Re=200	Re=250	Re=300
Nathen et al. [57] *OpenLB*	-0.056	0.018	-0.006	0.010	0.019	-0.022
Breuer et al. [7] LBM	-0.056	0.048	0.054	0.070	0.109	-
Breuer et al. [7] FVM	-0.076	0.018	0.004	0.020	-0.001	-0.032

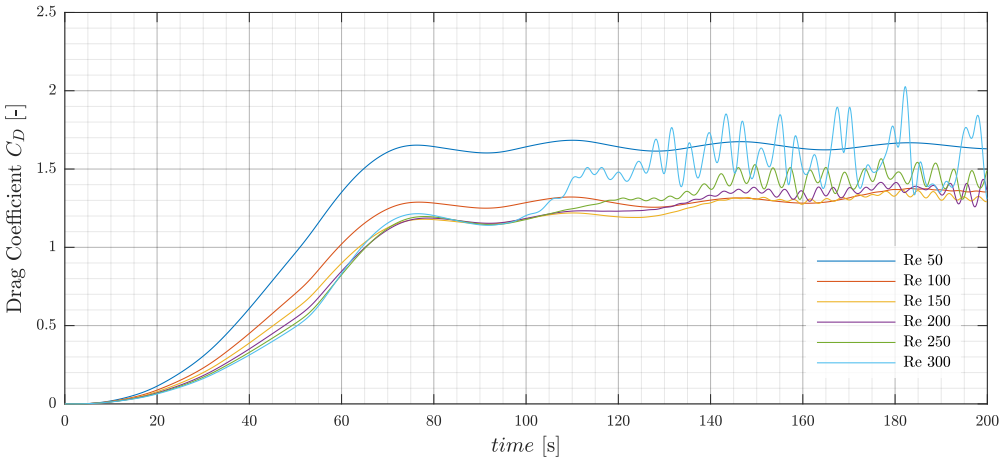

Figure 2.14: Drag coefficient over time for square cylinder of Reynolds numbers varying from 50-300

In Figure 2.12 results obtained with the present *OpenLB* study are compared with data from literature. It shows that result matches the FVM and *OpenLB* results much better than the regular LBM solution of Breuer et al.. This is mainly due to the improved solid boundary treatment of the body, introduced by Bouzidi et al.[6]. There are some small deviations from reference data, this could be caused by how the average is determined. As can be seen in Figure 2.14, after reaching maximum velocity the drag coefficient is oscillating around a mean, the oscillations are caused by vortex shedding or better know as a Karman vortex street. A snapshot of the flow around the square cylinder can be seen in Figure 2.15. In the sub-plots the behavior of the flow at various Reynolds numbers is illustrated, with Figure 2.15d clearly illustrates a more chaotic vortex shedding than Figure 2.15b where a periodic motion can be observed.

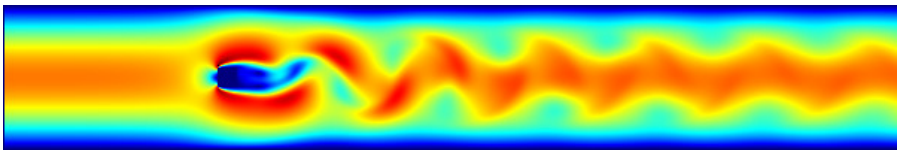

(a) Velocity contour at Re=100

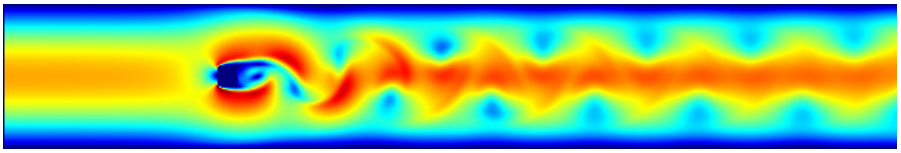

(b) Velocity contour at Re=200

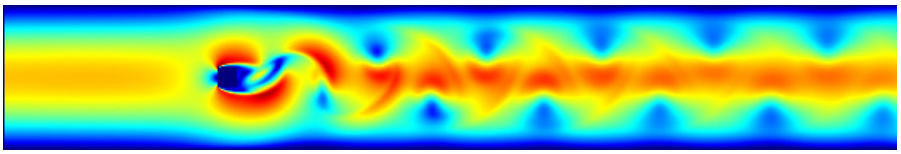

(c) Velocity contour at Re=250

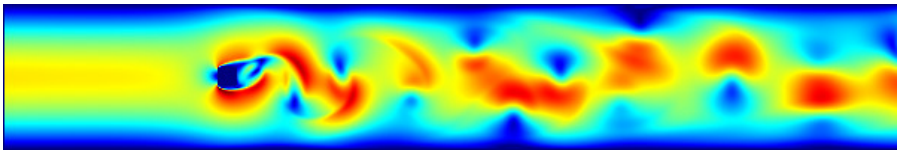

(d) Velocity contour at Re=300

Figure 2.15: Velocity contour plots for different Reynolds numbers: (a) Re=100, (b) Re=200, (c) Re=250, (d) Re=300

To make a detailed comparison between Breuer et al. [7] and the current validation case, the velocity profiles around the square cylinder are compared. In Figures 2.16 and 2.17 two velocity profiles in streamwise direction are illustrated, at a Reynolds number of 100. Figure 2.16 shows the velocity profile in x-direction. The figure shows that the results match excellent upstream, downstream there is a phase shift. However, the values of the velocity profile are correct, this could be as a result of a small deviation in how the values are measured or how the meshing is performed. Also, the difference in applied boundary condition on the body could play a role.

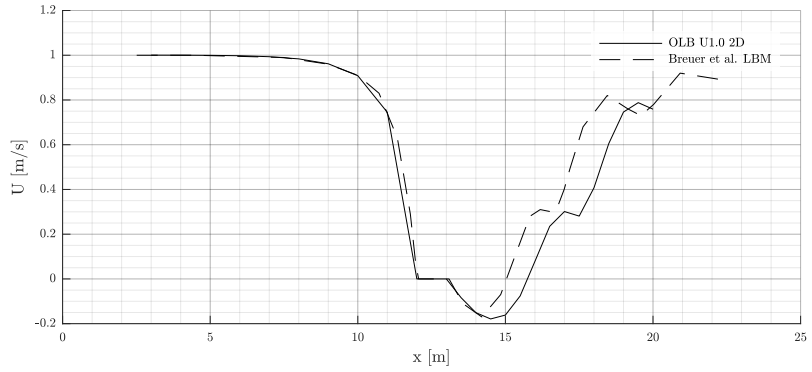

Figure 2.16: Comparing streamwise velocity (U) with Breuer et al.[7] at a certain moment, along the centerline (y=0) for Re=100.

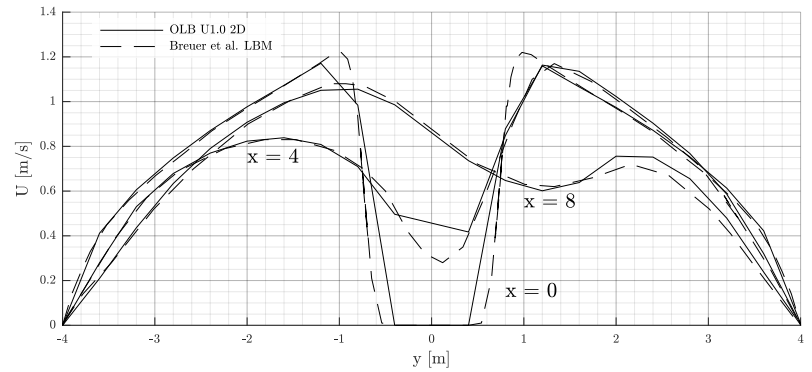

Figure 2.17: Comparing streamwise velocity (U) with Breuer et al.[7] at a certain moment for three different position in the flow, center of cylinder (x=0), near wake (x=4) and far wake (x=8), Re=100.

Figure 2.17 shows a plot of the velocity profile in the y-direction at three different positions: center of the cylinder (x=0), near weak (x=4) and far wake (x=8). The results are almost identical, however, there are some deviations. For x=0 the velocity profile near the cylinder is somewhat different and this could be explained. The choice of the physical simulation time has an influence in how the velocity is build up and therefore how the flow behaves. Also, a certain point is chosen where the velocity is measured so this could have an influence on how the lines are interpolated. The error in the interpolating of the chosen point is very well visible at the near wake measurement (x=4), where there are no points on or an extension of the cylinder center. Overall the results are very satisfactory.

2.7.2. Laminar Flow Simulation Around a 3D Cylinder with *OpenLB*

The paper of Schäfer et al. [67] is a CFD benchmark test for 2D/3D square and round cylinder at low Reynolds numbers. A large number of research groups participated in the construction of the benchmark comparison. The following simulation with *OpenLB* is to compare and validate the program with this benchmark test. For the comparison, a round cylinder in a channel is simulated to the presented literature data. In Figure 2.18 the geometry and the applied wall boundary conditions are illustrated. In the paper the following quantities must be computed to have a qualitative comparison: maximum drag coefficient $C_{D_{max}}$, maximum lift coefficient $C_{L_{max}}$, pressure drop ΔP with the measuring points just in front and back of the cylinder.

For the inflow conditions, an equation is given

$$U(0,y,z,t) = 16U_m yz(H-y)(H-z)/H^4, \quad V = W = 0 \tag{2.19}$$

where the $U_m = 2.25m/s$ and a yielding Reynolds number of $Re = 100$. The other variables in Equation (2.19) can be found in Figure 2.18

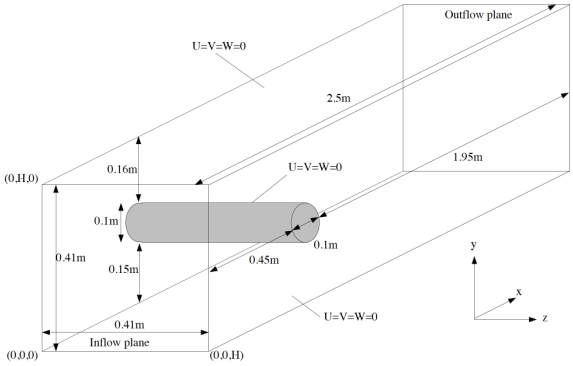

Figure 2.18: Geometry and applied boundary conditions for flow around a circular cylinder, drawing from [67]

Table 2.3: Flow characteristic value comparison of *OpenLB* with literature, for a 3D cylinder in a channel

Case	$C_{D_{max}}$	$C_{L_{max}}$	ΔP
OpenLB	3.338	0.015	-0.138
Schäfer et al. [67]	3.25	0.003	-0.10

This shows that the drag and pressure predictions are within reasonable margins. However, the lift prediction is not very accurate. The expectation is that due to the off-center location of the cylinder there must be positive lift coefficient. This could be due to relative coarse mesh, to increase the accuracy a higher mesh resolution need to be used.

2.8. A Brief Comparison Between Commercial and Open Source Software

In this section, a brief overview of the difference between open source LBM CFD packages as *OpenLB* and commercial solutions as Exa's Powerflow are discussed. A misconception that is often associated with open source CFD software is that is either less accurate and less efficient compared to proprietary solutions. This is not true for some of the open source CFD tools that have a strong community support. Almost all open source codes are publicly available. The accuracy, as often with numerical simulation, is determent by mesh resolution and quality, numerical schemes and the physical models that are used. In the end, the user has control over the accuracy of the results. For commercial software, the efficiency of the code is much better because the applications are mostly on a certain certified system where it is easier to optimize for. Open source is more generic so that is applicable for a wide range of systems. This can be easily solved by tweaking the compiling settings for the used systems. However, it must be said that open source CFD software is not for everybody. There must be some sort of affiliation with either programming and understanding the numerical approaches of aerodynamics and its limitations.

If one aspect is compared between the open source tool and commercial software where a difference in philosophy is exposed, is turbulence modeling. A commercial package as EXA's PowerFLOW, which also uses LBM, combines Very Large Eddy Simulation (VLES) and a κ-ϵ Renormalization group (RNG) to model turbulent boundary layers [17]. This makes it easier to simulate high Reynolds number flows because the majority of the flow is modeled and not simulated. Whereas *OpenLB* only uses LES models to simulate the turbulence. This restricts the use cases of the open source tool to low Reynolds numbers and more academic driven projects. *OpenLB* is still very new to the CFD realm and needs time and more developers to bring it to the next level of mainstream use. Both parties have a different philosophy in which turbulence model is used for the simulation. This does not mean that one is better than the other. A choice is made for the method that suits best with each group.

3

Numerical Analysis

Using Computational Fluid Dynamics (CFD) based on the Lattice Boltzmann Method (LBM) the flow of a bluff body is analyzed. The geometry of the model is presented in Section 3.1. After all the settings are set, the parameters are chosen and boundary conditions are implemented in Section 3.2. All the result of the front-edge radius and tail angle effects are given, in Section 3.3.

3.1. Surface Model: GETS

Heavy-duty vehicles have a complex geometry with gaps and various object that have an influence on the flow around the object. To reduce the complexity of the model and still have the correct flow characteristics is very important. Moreover, to create a mesh of such a complex geometry is a time-consuming task and computational intensive job. To capture general flow characteristics around a specific type of bluff body that represents a generic heavy-duty vehicle, a model designed by van Raemdonck [78] is used for this study. The model is named GETS and it is inspired on generic European heavy-duty truck, with its maximal dimensions. The model used for the present study is a 1:50 scale model of the original GETS model and is illustrated in Figure 3.1. The dimensions of the original model and the currently used can be found in Table 3.1. The model is too small to obtain accurate boundary layer flow phenomenon, due to the material (wood) that is made of but also the Reynolds number. The actual model tested is the wind tunnel by van Raemdonck [78] is much larger and the Reynolds number are multiple factors higher, however, the general flow patterns stay the same. Hence, the choice to experiment with various front-end rounding and rear-end angles, Cooper[11] has demonstrated it with larger models and Reynolds numbers.

Using LBM with Large Eddy Simulation (LES) limits the code to solve high Reynolds number flows without using a very fine mesh size. Hence, the choice is made to create a small model that operates with a Reynolds number in the magnitude of $Re = 8,000 - 60,000$, with measurements performed every intermediate step of $Re = 4,000$.

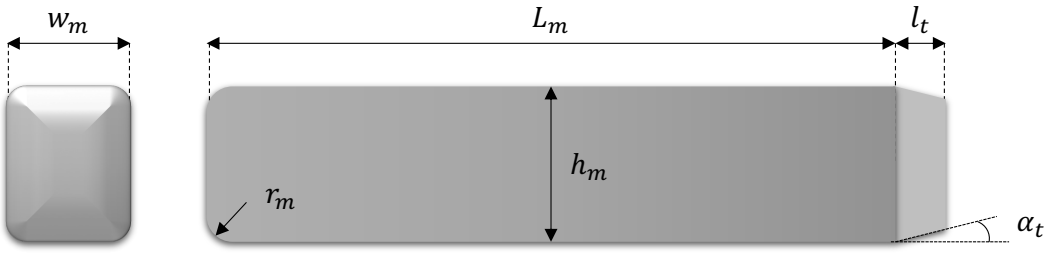

Figure 3.1: Geometry of the GETS model

[1] Various values are used during the study

Table 3.1: GETS dimensions of original and scaled model used in current study

Dimensions	Symbols	1:1	1:50	Units
Length	L_m	16,500	33	[mm]
Width	w_m	2,600	51.9	[mm]
Height	h_m	3,500	70.2	[mm]
Front-end radius	r_m	540	10 [1]	[mm]
Tail length	l_t	1,500	30 [1]	[mm]
Tail angle	α_r	12	12 [1]	[°]

3.2. *OpenLB* Simulation Set-up

3.2.1. Computational Domain and Grid Generation

The computational domain is generated by converting a CAD file into a Stereolithography (STL) file. An STL file describes the surface geometry of an object without any additional information about the material, color or other commonly CAD model attributes. The body is subtracted from the channel so that the object is part of the fluid domain, in Figure 3.2 an example of the computational domain is given. By means of material numbers appointment, the boundary condition can be defined. The different colors in Figure 3.2 define a boundary condition, each of the colors is a specific boundary condition that is assigned to that part of the domain. In Section 2.3.2 the power of material number assignment for boundary condition is explained in more detail.

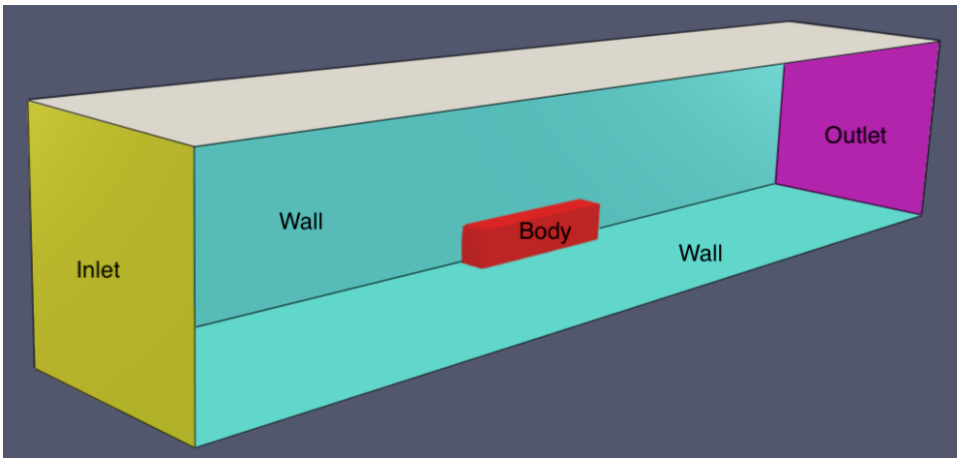

Figure 3.2: Fluid domain and boundary orientation

The grid is automatically generated within the LBM framework. The strength of LBM, in general, is that complex geometries can be meshed very easy and that the appropriate boundary conditions are assigned to the right voxels without extra work. The voxels size depends on the chosen resolution given by the user. Due to the nature of LBM, the voxel size is the same over the entire fluid domain. There are grid refinement functions available with various LBM platforms however not with *OpenLB*. This causes a staircase-like representation of curved bodies and non-straight walls. The automatic grid generation with a uniform voxels size has a major influence on how the body is represented. The front-end rounding of a GETS model will be a staircase-like shape with the possibility that the radius is not consistent all around. The discretized shape of the body has considerable influence on how the flow will behave, especially when a coarser mesh is used. Because of the uniform mesh grid size and the absence of a local grid refinement function within *OpenLB* the very detailed flow phenomenon will not be captured.

3.2.2. Boundary Conditions

One of the advantages of LBM is that complex boundaries are easy to implement in complex geometries e.g. porous media. This convenient way of applying boundary conditions in fluid domains is also implemented in *OpenLB*, in a very clever way. The problem with defining boundary conditions in LBM is the local and non-local boundaries that can be applied. Both must be handled differently, however, with the help of so-called

OnLattice BoundaryCondition object function, one can treat local and non-local boundaries the same way. The generic mechanism of boundary condition initiation is very easy and convenient for regular geometries. In irregular geometries, even if a staircase approximation of the geometry is agreed, it's hard to appoint the correct boundary to each node. Although OffLattice BoundaryCondition object function is not very mature in *OpenLB*, where the appointment of the correct boundary to the node is much better, there is a possibility to use it for only the Bouzidi boundary condition.

Furthermore, in this section, every boundary condition that is applied is briefly discussed and the motivation of choices are elaborated on the basis of finds that are gathered along the whole processes of the simulation set-up.

Initial Conditions

The initial conditions are a mandatory set of variables to able to start the simulation. In LBM the initialization of the simulation is somewhat different compared to steady-state Navier-Stokes simulations. The particle population at $t = 0$ is set with the parameters that are shown in Tables 3.2 and 3.3. The values in Table 3.2 are a mandatory set of variables that are needed to start the simulation. From this set of parameters the lattice, conversion factors and the physical values are calculated by the UnitConverter function within *OpenLB*. The choice is made to fill in the characteristic length, inlet velocity and the density of the wind-tunnel test conditions. However, this is not necessarily the requirement to get a physical solution, the most important is that the non-dimensional variables e.g. Reynolds number is the same as with the wind-tunnel test, this is also mentioned in Section 2.3.1. The choice of latticeRelaxationTime is very important one because that sets the accuracy and stability of the simulation. It is chosen that the model simulation uses a relaxation time of $\tau = 0.5002$, this is number is selected by trial and error but also some external advise from one of the contributors to *OpenLB* [2].

Table 3.2: *OpenLB* initial conditions

Variables	Symbol	Value	Unit
Resolution	N	30	[-]
latticeRelaxationTime	τ	0.5002	[-]
charPhysLength	charL	0.06	[m]
charPhysVelocity	charU	1	[m/s]
physViscosity	ν	$1.456E^{-5}$	$[m^2/s]$
physDensity	ρ	1.2	$[kg/m^3]$
pressureLevel	p	0	[Pa]

Table 3.3: *OpenLB* constant simulation values

Variables	Symbol	Value	Unit
Reynolds number	Re	$8,000^*$	[-]
Max. simulation time	T	10	[s]
Convergence Residuum	ϵ	$1E^{-6}$	[-]
Convergence check interval	ΔT_{check}	0.1	[s]

A typical output file at the start of the simulations is given in Table 3.4, this is only a selection of all the calculated and converted parameters that are used during the simulation. In Table 3.4 the key parameters are given so that at a glance can be seen if all the parameters are correct or in the right order of magnitude.

[2] Recommend by Marc Haussman, Ph.D. LBM Turbulence modeling with *OpenLB* at Karlsruhe Institute of Technology. Through mail and phone contact a better insight in the working *OpenLB* is gained.

Table 3.4: *OpenLB* UnitConverter information at the start of the simulation

Parameters:	Symbol	Value	Unit
Resolution:	N=	30	[-]
Lattice relaxation frequency:	omega=	1.9996	[-]
Lattice relaxation time:	tau=	0.5002	[-]
Characteristical length:	charL=	0.06	$[m]$
Characteristical speed:	charU=	1	$[m/s]$
Phys. kinematic viscosity:	charNu=	4.6729e-06	$[m^2/s]$
Phys. density:	charRho=	1.2	$[kg/m^3]$
Characteristical pressure:	charPressure=	0	$[N/m^2]$
Reynolds number:	reynoldsNumber=	8,000	[-]

Conversion factors:	Symbol	Value	Unit
Voxel length:	physDeltaX=	0.00333333	$[m]$
Time step:	physDeltaT=	7.92593e-05	$[s]$
Velocity factor:	physVelocity=	42.0561	$[m/s]$
Density factor:	physDensity=	1	$[kg/m^3]$
Mass factor:	physMass=	3.7037e-08	$[kg]$
Viscosity factor:	physViscosity=	0.140187	$[m^2/s]$
Force factor:	physForce=	0.0196524	$[N]$
Pressure factor:	physPressure=	1768.71	$[N/m^2]$

Inlet

The inlet boundary conditions is a very easy implementation to a velocity boundary condition. There are a few approaches on how to implement the boundary condition. The standard method is to first define the inlet as part of the fluid domain, secondly, the velocity boundary can be set by OnLattice BoundaryCondition and added the velocity boundary to the given material number. There is also a possibility to set the inlet as a Bounce Back boundary condition where a velocity value can be given to the wall. A third option is to set it as a Bouzidi BC making it an interpolative inlet condition. It depends on the case that is running which boundary condition is required. There are some possible problems that can be causing the simulation to diverge and there are mentioned briefly below.

Using the standard approach to define the inlet can possibly give rise to a problem of extremely high pressure at the corners. These artifacts in the corner cause the simulation to diverge when the maximum velocity at the inlet is reached. This can be a consequence of how the material number of the inlet is set and positioned. The solution to this problem is either to try and move the inlet cuboid to solve the problem or use a different inlet boundary condition.

Using the Bouzidi BC as an inlet condition can solve the problem with high pressure in the corners, however to a certain extent. When the resolution of the mesh is to high the interpolative nature of the Bouzidi BC can cause for problems and as a backup retreat to the bounce back boundary condition. This causes the inlet to be set as a regular wall without any velocity description. Solution to the problem is to have a bounce-back velocity boundary condition with a prescribed velocity so that the inlet does not behave as a wall but as an inlet.

The velocity inflow is build-up slowly, Figure 3.3 shows a plot of how the maximum velocity is reached. To guarantee that the inflow is smooth and not causing any numerical divergence by choosing a too large time step. There is two possible function with both somewhat similar ramp up to the end value, the Sinus and Polynomial StartScale. The curves are a function of the total simulation time, *T*, and Time step, *physDeltaT*, given in Tables 3.3 and 3.4 respectively. Figure 3.3 shows that if the maximum velocity is reached the simulation maintains that velocity until the simulation is over. The time it needs to reach the maximum velocity can be set manually or as a function of the total simulation time. Taking in account that the velocity ramp-up is not to steep. In Figure 3.3 the maximum is reached in half of the total simulation time. This fraction has a dominant role in the stability of the simulation. If the fraction is too small, which means that the velocity inclination is very steep, additional numerical instabilities can been introduced that cause a possibility of divergence.

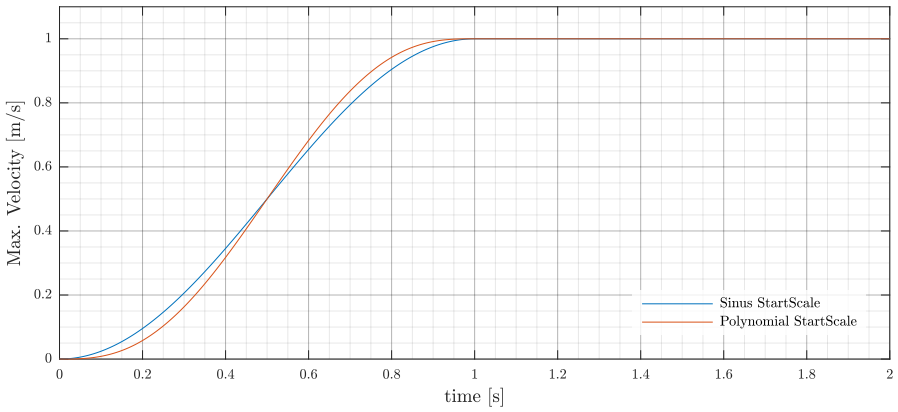

Figure 3.3: Inlet velocity build-up profile for Sinus StartScale and a Polynomial StartScale

Walls

For the walls, a no-slip boundary condition is imposed. By using the standard bounce-back boundary scheme. As mentioned before *OpenLB* only considers a wet-node approach for there implementation of the bounce-back boundary.

Body

There are two options to accurately describe a complex geometry, with a structured or unstructured grid. The later uses a coordinate system that fits the geometry boundary. This leads to a body-fitted mesh where the advantage of a simple Cartesian grid is omitted, especially if the geometry varies in time re-meshing becomes necessary and a time-consuming task [23]. Most LB methods use a lattice to mesh the fluid domain and thereby take the advantage of a Cartesian grid, which makes it easy to correct only the behavior of the boundary nodes instead of adjusting bulk nodes to match the geometry.

The simplest boundary condition that is used to describe a geometry in LBM is the bounce-back boundary condition. It is a local, simple and efficient method to describe complex boundary conditions. However, due to its simplicity, the bounce-back BC approximates a curved boundary with a staircase. In Figure 3.4 an example of a circle is shown in how the nodes are assigned to be either a part of the fluid or the boundary. Any lattice link, $\mathbf{c}_i$, connects a boundary and a solid node with a link line, where a wall node (shown as a solid square) is in the middle. The resulting staircase shape is shown as a grey-area in Figure 3.4. The particle populations are moving from $\mathbf{x}_b$ to $\mathbf{x}_s$ along the link lines of $\mathbf{c}_i$ and are bouncing back a the boundary $\mathbf{x}_w$.

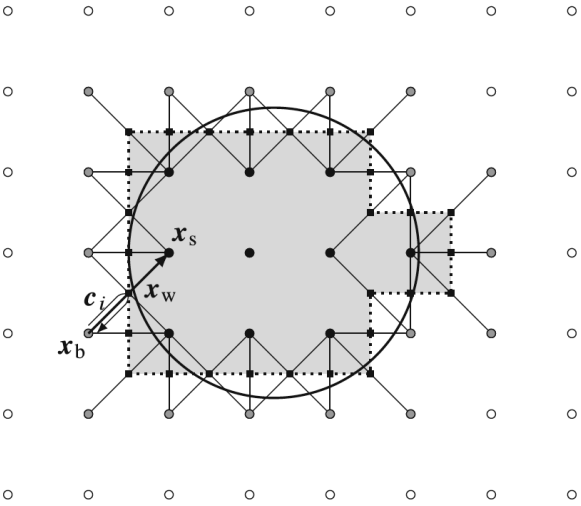

Figure 3.4: A staircase approximation of a circle. A typical curved geometry can be discretized on a lattice by exterior fluid nodes (white circles), external boundary nodes (grey circles) and interior solid nodes (black circles) first.[42]

This can lead to minor problems and in particular a reduction in accuracy due to slightly different object shape. To overcome these problems and increase the accuracy, improved and interpolation bounce-back schemes are proposed. The one used in this study is the interpolated bounce-back boundary proposed by Bouzidi et al. [6]. This method deals much better with curved and inclined boundaries than the regular bounce-back scheme, a more detail description of the method is given in Section 2.3.4. The Bouzidi keeps the non-slip nature of the original bounce-back method so this makes it very useful to apply to the GETS model for the present study. A comparison is made of the bounce-back and Bouzidi schemes in Section 3.3.2.

3.2.3. Turbulence Modelling

Most of the present existing subgrid closure solutions use a crude model developed within NS and implemented in LBM-LES in a straightforward matter, namely the Smagorinsky eddy-viscosity model. Sagaut [66] proposed a new LBM-LES approach away from the eddy-viscosity model and written directly in the LBM framework. However, *OpenLB* is a relative new LBM code so mostly the regular LES models are available.

LES - Smagorinsky model

The choice of turbulence model for this thesis is the consistent Smagorinsky Malaspinas and Sagaut [52] [3]. The method of Malaspinas and Sagaut [52] introduces a consistent way to solve the SGS closure problem in the BGK Boltzmann equation for turbulence flows in large eddy simulations. The method allows the models that are developed in the Navier-Stokes framework to be easily implemented in a straightforward manner. The method showed promising results and a good match with literature in the weakly compressible domain. Also, a consistent way of computing the strain tensor from the velocity distribution function is achieved and showed more accurate results than with the original Smagorinsky model. The choice is for this type of turbulence model is based on the paper by Malaspinas and Sagaut [52], which gives promising results, and through mail correspondence with Patrick Nathen, Ph.D. in turbulence modeling at the Technical University of München, which also works with the *OpenLB* code and has experience with turbulence modeling within the Lattice Boltzmann Method framework.

The Smagorinsky constant is an important parameter that determines the dissipative rate of the turbulence model. Often the constant is used as a calibration parameter to fine tune the model. The Smagorinsky constant commonly takes a value ranging from 0.1 - 0.2 depending on the flow and application [19]. For this study, the choice is made to set the Smagorinsky constant to 0.14. Choosing the right value for the constant requires experience in the field of turbulence modeling but also experience in Lattice Boltzmann Methods. Because the constant is very dependent on the type of flow problem. Nevertheless, due to trial and error but also advise from people in this field the constant is set to $C_s = 0.14$.

3.2.4. Numerical Error & Accuracy

There is an infinite amount of possibilities to get a correct physical flow, that highly depends on how the variables, Δx, Δt and τ^* are balanced in Equation (2.12):

$$\nu = c_s^{*2}\left(\tau^* - \frac{1}{2}\right)\frac{\Delta x^2}{\Delta t}$$

These parameters should be chosen such that a high accuracy is achieved within reasonable computational time. The lattice spacing Δx sets the spacial description error of the simulation and directly influences the model geometry, thus determines the computational cost. The time step Δt will influence the magnitude of the temporal discretization error and sets the total amount of steps needed for the simulation. From the aforementioned parameters relaxation time τ^* is the most important one [18], because it characterizes the time scale behavior of the particles populations and establishes the fluid viscosity. There is no error estimation that can be deduced from a general principle to predetermine the right values for Δx and τ^* for a given Reynolds number. Feng et al. [18] and Krüger et al. [42] suggest the following:

1. Choose Δx considering the spatial resolution to capture relevant flow physics
2. From the stability consideration choose a τ^* that is close to unity if possible. For high Reynolds number it has to obey the following equation $\tau^* > \frac{1}{2} + \frac{1}{8}U^*_{max}$
3. Calculate the time step Δt with Equation (2.12) and the lattice velocity can be determined. To have an accurate solution is should not be above 0.1
4. Run the simulation

[3] Recommend by Patrick Nathen, Ph.D. LBM Turbulence modeling at Technische Universität München

This is a procedure that needs to be taken for a stable simulation. If the chosen parameter gives a stable simulation the lattice velocity needs to be checked if it is within limits, not exceeding 0.4, then an accurate simulation may be achieved. If this is not the case, the grid size needs to be reduced. Reducing the spatial description error often a method of diffusive scaling is used. Diffusive scaling means that the relaxation time is kept constant and the grid size is changed until the error reaches a stable value, often used for grid sensitivity studies. A particular relation that is given by using diffusive scaling is $\Delta t \propto \Delta x^2$. It guarantees that the leading total error scales with Δx^2. This also means that the LBM becomes effectively first-order accurate in time.

Furthermore, when the simulation diverges a larger relaxation time may be needed. The real challenges come with simulation turbulent flows with high Reynolds numbers. The small kinematic viscosity that is associated with turbulence is not applicable for the normal LBM. Hence, the introduction of turbulence models where small scales can be modeled and do not have to be simulated is of an essential to have a stable, accurate and computational efficient application.

Using the procedure that is suggested by Feng et al. [18] and Krüger et al. [42] the parameters for the simulation are chosen. For the lattice spacing size a grid sensitivity study is performed in Section 3.3.1 to determine the best possible voxel size taking the required computational recourses into account. After consulting with Marc Haussman, Ph.D. LBM Turbulence modeling with *OpenLB* at Karlsruhe Institute of Technology, using the procedure and applying knowledge derived from literature the relaxation time is chosen to be $\tau^* = 0.5002$. This applies to all the cases in Section 3.3. The chosen Reynolds number for the simulation basically determines the kinematic viscosity of the flow so this is not something that needs additional investigation.

3.3. Numerical Results

In this section, a mesh sensitivity study is performed. A comparison is made between the Bouzidi and Bounce back boundary condition. The effect of the position of the model is tested and the influence of it shown and discussed. Both the effect of the front-edge rounding and rear-end modification are shown and is discussed in more depth. The simulations of the position and the boundary conditions are performed at a Reynolds number of 8,000 because with all the limitations of *OpenLB* this gives a more accurate result. Furthermore, the effects of the front-edge radius and rear-end tail are only simulated for three Reynolds numbers, 8,000, 24,000, 48,000, respectively. This is because a simulation takes a significant amount of time and a large portion of the HPC of the faculty is used. So, therefore, a choice is made too only simulate three Reynolds number configurations and discuss them more in-depth.

3.3.1. Mesh sensitivity study

Numerical simulations of fluid flows are very dependent on the mesh resolution that is used. Hence, the mesh sensitivity study is performed to determine how the mesh influences the results. Because *OpenLB* generates a uniform mesh so no local grid refinement is added around an area of interest. Seven mesh resolutions, all with different voxel sizes, are studied to determine the effect of the fines of the mesh. The results of the mesh sensitivity study are shown in Figure 3.5. A GETS model with a front-end radius of 24mm (R24) is used to conduct the study, and at a Reynolds number of Re=8,000. A trend can be seen, the drag coefficient is decreasing with increasing mesh resolution. There is also, what it seems, a mesh convergence. With a resolution of N=40 and N=44, there is less than 1% difference or 4 drag counts. The drag values of N=40, N=44 and N=46 are very close, with less than 3% difference. Hence, the choice of a mesh resolution of N=46 is chosen to run the simulations. This will require more computational recourses but will give a more stable simulation at high Reynolds, damping the oscillation more.

Besides the spatial resolution, it is also important that the simulation runs long enough to reach a certain equilibrium. The transient nature of LBM gives the simulation an oscillatory solution. The simulation needs to pass the first transient moment to have an accurate average measurement of the drag coefficient. In Figure 3.5, this is very well visible that there is a hump an the beginning of the simulation, a result of the smooth velocity increase. After 1.9s the maximum velocity is reached and the simulation reaches an oscillatory pattern around a mean value.

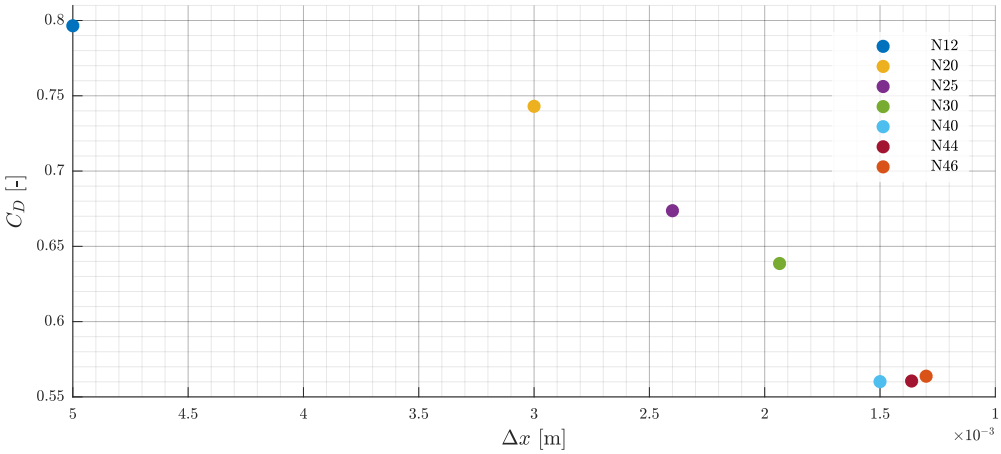

Figure 3.5: Mean drag coefficient as a function of voxel size

In Figure 3.5, for the most mesh resolutions it is chosen to have a long simulation time, of 10 seconds, which is possible due to the large voxels size that is needed to cover the whole domain. However, with the increase of the mesh resolution, a shorter simulation time is preferred due to the limited computation resources that are available at the faculty of aerospace engineering. The averaging window must be large enough so that over a larger window the average drag coefficient does not change. The transient behavior dies out after the maximum velocity is reached at the inlet, therefore it chosen to set the averaging window from 3.0 seconds to 10.0 seconds. Measurements are performed every 0.1 second, so this gives a measurement frequency of 10Hz, this is due to the limited hard disk space that is available for each user at the High-Performance Computation (HPC) facility of the faculty. With a higher sampling frequency, the amount of data that would be generated will be too high and post-processing the entire fluid domain will cost a great amount of time. It was observed that this is also not necessary because of the clear, logical patterns that are visible from the low-frequency measurements.

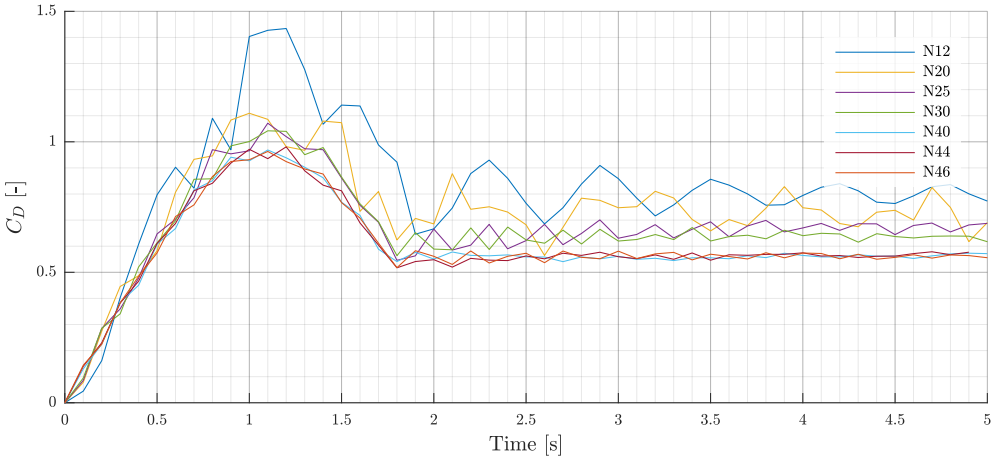

Figure 3.6: Drag coefficient as a function of simulation time for various mesh resolutions

3.3.2. Bounce Back vs. Bouzidi Boundary Condition

In this part, the bounce back and Bouzidi boundary conditions (BC) are compared. As discussed in Section 3.2.2, the bounce back (BB) boundary condition approximates a curved edge with a staircase shape. The Bouzidi boundary condition has a different approach to curved edges. Because of the interpolative nature of the Bouzidi rounded shapes are no longer approximated as a staircase but as interpolated curvature. The effect of both boundary condition on the drag coefficient and the flow characteristics are elaborated in the

following section.

Considering Figure 3.7, where the drag coefficient build-up is plotted against the simulated time. The figure shows that there is a small difference of C_D between the two boundary conditions. The mean C_D is given in Table 3.5. The difference is 42 drag counts or 7.0% if bounce back is compared to Bouzidi.

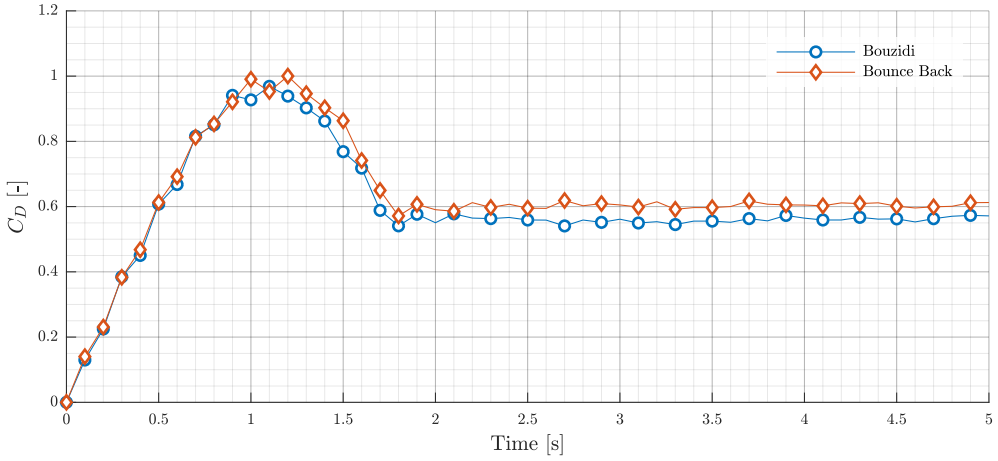

Figure 3.7: Drag coefficient of a Bouzidi and Bounce Back boundary condition applied on the R24 GETS model at a Re=8,000 with N=46

Table 3.5: Mean drag of Bouzidi and Bounce Back boundary condition

	Bouzidi	Bounce Back
Drag	0.565	0.607

In Figure 3.8 a time-average plot of the front-end of an R24 model is shown. Figure 3.8a the Bouzidi BC is applied and in Figure 3.8b the bounce back BC is applied. There is some difference in the shape of the laminar separation bubble but also the strength of the recirculation velocity. The staircase approximation of the BB scheme gives a more disturbed flow over the front-end curvature. This results in a higher pressure gradient and consequently a larger separation bubble over the top of the model. The larger vortex over the front of the model with BB also shows that the velocity in the x-direction is more negative, this is visible by the darker orange color in Figure 3.8b. Considering Figure 3.8a with the Bouzidi BC, there is a smoother transition along the curved edge. The adverse pressure gradient is more favorable which generated a weaker laminar separation bubble and therefore produces less drag. From this point onward the Bouzidi BC will be used as boundary condition for the body.

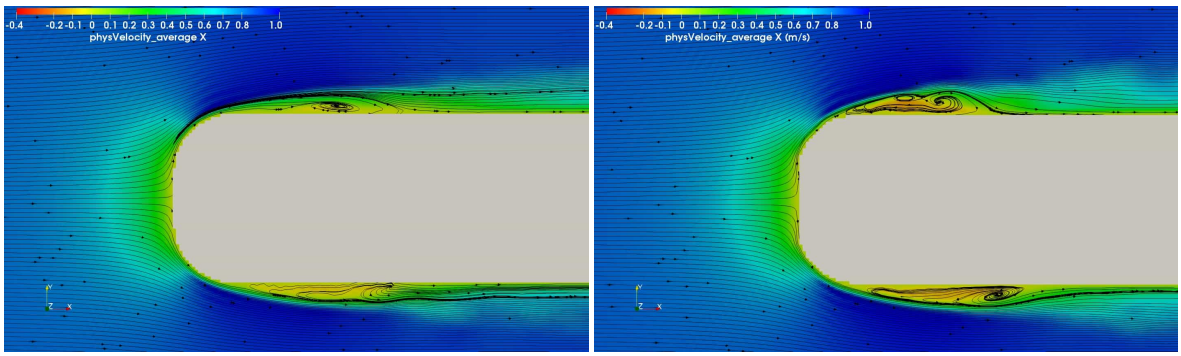

(a) Bouzidi (b) Bounce Back

Figure 3.8: Time-average contour plot of the x-velocity where Bouzidi and Bounce back boundary conditions are applied on a R24 model at a Re=8000 with N=46

3.3.3. Model Position

In the current study, the position of the model in the wind tunnel set-up is slightly different compared to the test performed by van Raemdonck [78]. Because a different wind tunnel facility was used the position of the model needed to be placed somewhat higher to stay clear from the wind tunnel boundary layer. The original test performed by van Raemdonck [78] are at ground proximity where different flow phenomenon may arise when compared to a slightly higher position. Nevertheless, a flow analysis is performed to see what the main differences arise from the model position.

Figure 3.9 shows the drag coefficient with respect to the simulation time and an observation can be made that the drag difference between the two positions does not vary significantly. In Table 3.6 the mean C_D is given. The deviation of the mean drag coefficient is 18 drag counts. Despite very close results for different model positions, some remarks need be addressed from this. First, with the lower model position, the oscillations of the drag coefficient around a mean are much severe than with a higher position. This makes the deviation from the mean is much larger. There are also similarities when it comes to the pressure distribution at the front of the model. Figure 3.9 shows the drag coefficient for both positions. From the plot it can be concluded, although the shape of the pressure distribution is not similar it has some resemblance.

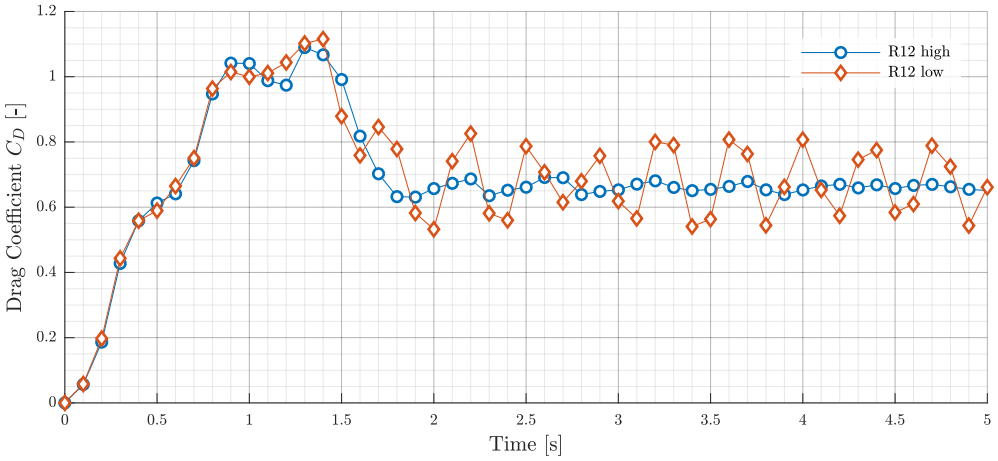

Figure 3.9: Drag of R12 model for different positions in fluid domain at a Re=24,000 with N=46

Table 3.6: Mean drag of high and low position

	High	Low
Drag	0.657	0.675

The pressure is obtained at a constant distance from the surface of the model, this mainly to get the correct values as close to the surface as possible. From experience working with *OpenLB* it has come to the attention that if a point very close to the surface is taken it will give unrealistic results. These simulated results are not viable anymore to make a comparison with literature. There is not the possibility to have the pressure at the model surface due to a lack of a wall model. Therefore, no accurate shear stress on the surface of the model is calculated.

Stagnation point of the model at a higher position is located very close to the center of the model, whereas the model at a low position the stagnation point is slightly off-center as can be seen in Figure 3.10a. The somewhat eccentric location of the stagnation is due to the fact that at one of the edges flow accelerates more than at the other which causes a region of lower pressure. This generates a thrust force for the model that is situated at a lower position, this results in a drag relief at the front. Looking a the pressure plot at the rear, Figure 3.10b. The pressure plot gives a clear explanation that there is drag difference between the two positions. The model at ground proximity has a more negative time-average mean pressure coefficient, compared to the higher position.

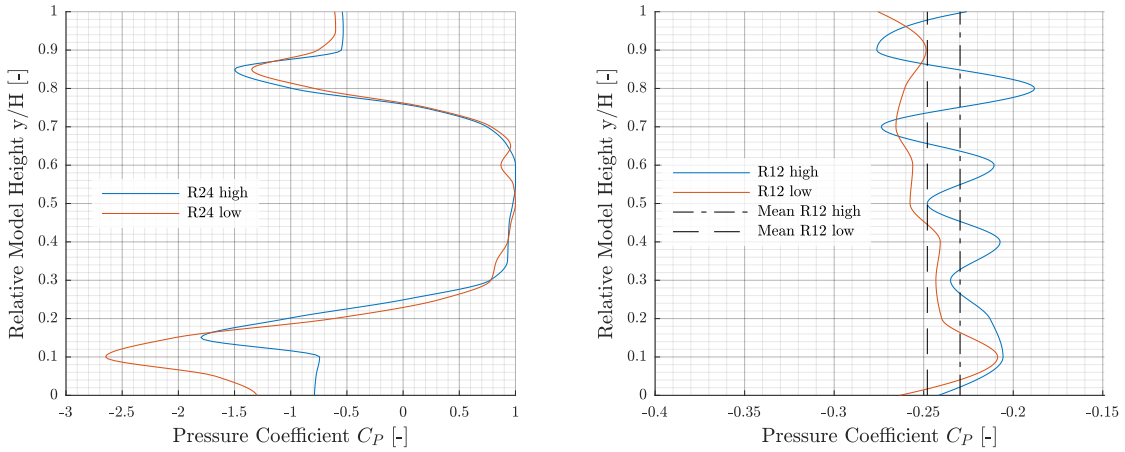

(a) Pressure coefficient front z=0.5W

(b) Pressure coefficient rear z=0.5W

Figure 3.10: Time-average numerical pressure coefficient of the front and rear of a R12 configuration for various elevated positions at a Re=24,000 with N=46

Considering Figure 3.11, where a white line is drawn aft of the model. Along this line, with an equidistant spacing from top to bottom, the pressure and velocity are measured. From the measured quantities, the pressure coefficient can be determined. The transient nature of LBM means that at every time step the pressure distribution will be different, hence, the pressure coefficient will vary. Moreover, due to the use of LES for the turbulence modeling, it will give a more detailed insight in the physical quantities of the model wake. Looking at both contour plots in Figure 3.11, there is far more detail in velocity distribution compared to steady state CFD with RANS turbulence model. The more detailed velocity field also allows for even the smallest vortex to be visible and the effect of it to be studied. These different vortex structures in the wake of the model can be reflected back to the pressure coefficient over the rear.

Every recirculating region in the wake gives a more negative pressure peak. Considering Figure 3.10b, where the pressure coefficient of both positions are plotted. In the plot, it is visible that there are peaks with more negative C_P and peaks that are less negative. The more negative peaks mean that the velocity at the point is higher, this suggests either the flow is moving upstream or downstream of the model. Either way, this shows that there is a vortex. These vortices that cause the pressure peak are nicely illustrated and animated in Figure 3.11.

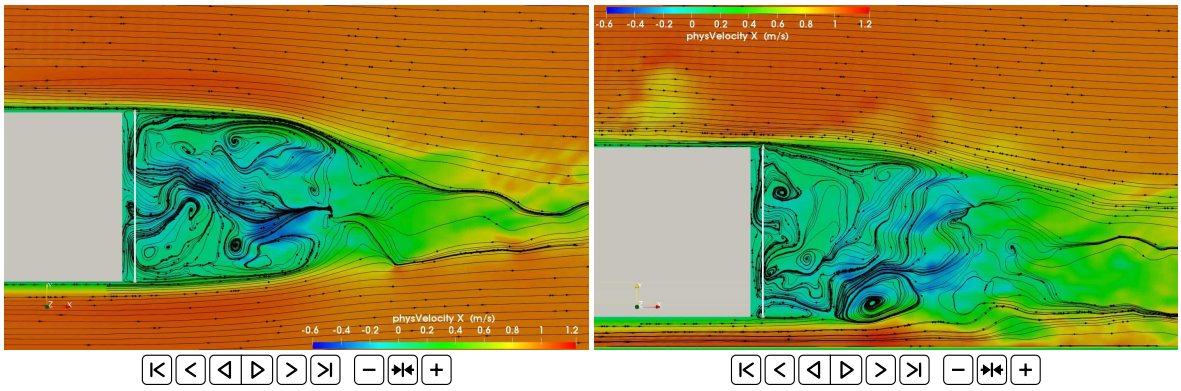

(a) R24 High

(b) R24 Low

Figure 3.11: Animated numerical contour plot of the x-velocity with streamlines of a R12 model both at high and low position at a Re=24,000 with N=46

3.3.4. Effect of Front-Edge Radius

From literature it is stated that the front and rear part of a heavy-duty vehicle generate the same amount of drag [87]. For the GETS model, this is different. The amount of drag generated by the front and rear is not equal as is investigated by [20, 78, 80]. The reason for this the difference is in the shape of the model. The rounded edges at the front cause the flow to accelerate and a low-pressure region to established.

Considering the model position that is used for the current study the effect of the front-edge radius variation is investigated. Because the model and simulated Reynolds numbers do not resemble the real-life operation conditions of a heavy duty vehicle, the variation of the front edge is a validation case of the fundamental flow phenomenon and drag force contribution. However, the ΔC_D compared with the same Reynolds number at a different front-edge radius will give a better insight into the correctness of the drag difference. Furthermore, comparing the drag for the same front-edge radius at various Reynolds numbers will give a better understanding of how and if *OpenLB* simulates the flow quantities correctly. The baseline radius of 4 mm is multiplied a couple of times giving configurations of 8, 12 and 24 mm. The drag coefficient of these configurations at Reynolds numbers of 8,000, 24,000 and 48,000 can be seen in Figure 3.12.

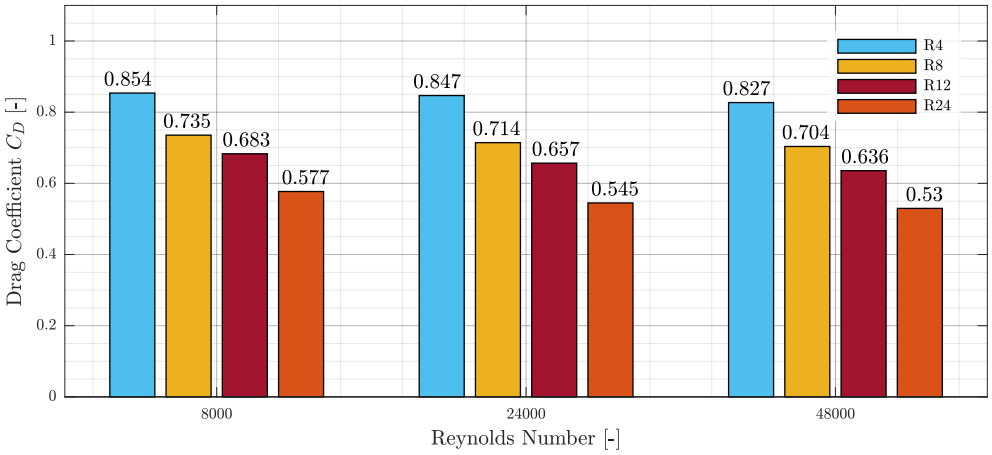

Figure 3.12: Drag coefficient of a GETS model with various front-edge radii at a Re=8,000, 24,000 and 48,000 with N=46

From the same figure, it can be seen that with an increasing Reynolds number there is a decreasing drag coefficient trend. This is better visible in Figure 3.13, where the drag of the simulations with a Re=24,000 and 48,000 are compared to that of the Re=8,000 and the drag reduction is given. Although, the reduction of drag is not significant there is a slight change. This matches the prediction made by Cooper [11], which shows that the drag coefficient in the subcritical region, that is Re=10^3-10^5, is somewhat constantly decreasing. Increasing the Reynolds number gives rise to other Reynolds number effects i.e. a drag-drop at a critical Reynolds number, however, that is beyond the scope of this study.

From Figure 3.12 another trend is visible. With the decrease of front-edge radius the drag coefficient increases. The small edge radius causes a thicker boundary layer that is build up over the side surfaces of the model. This thicker boundary layer has also an effect on the rear-end of the model. The thicker boundary layer causes a decrease in the back pressure which has a drag relieving effect, thus a smaller contribution to the total drag. The mechanism of this effect is shown in wind tunnel tests by van Raemdonck and van Tooren [79]. The increase in drag with decreasing front-edge radius is mainly due to the large stagnation surface, but also due to the suction peak at the front due to the separation of flow.

This influence of the thicker boundary layer on the pressure distribution over the rear of the model can also be seen in the pressure plots. In Figure 3.14b the pressure coefficient of four different radii are plotted against the relative model height at an Reynolds number of 24,000. When the smallest radius is considered, in this case, R4 which is 4mm, the average pressure coefficient will be more negative compared to that of the largest radius, R24 with a 24mm. Although the behavior of thicker boundary layer having an influence on the drag reduction aft of the model it pales in comparison with the drag generated due to the large stagnation surface. Nevertheless, this is not completely consistent when looking at Figure 3.14b. The front-edge of R8 and R12 have the same influence as that of R4, the expectation will be that with increasing radius the boundary layer thickness decreases and therefore the influence it has on the pressure magnitude on the rear

will diminish. According to the numerical and experimental results found by Gheyssens [20], van Tilborg [80] the pressure plots of R8 and R12 should be closer to R24 than R4.

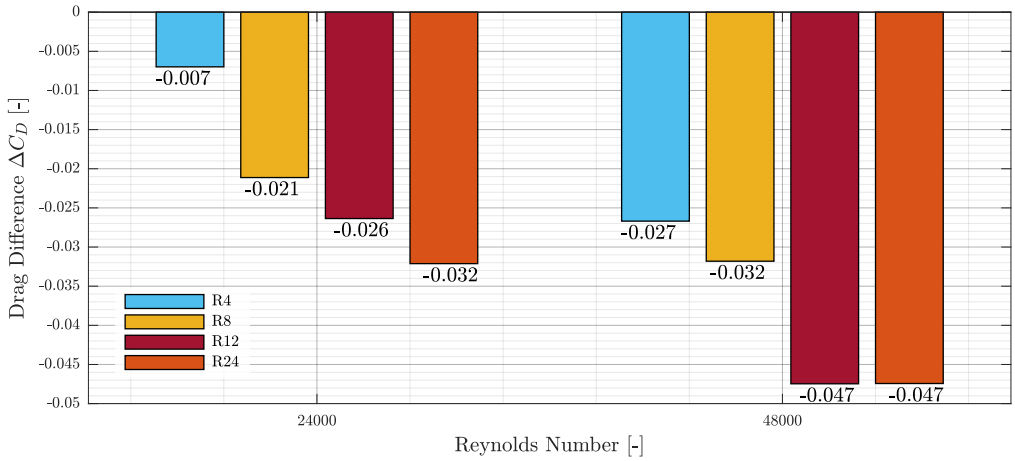

Figure 3.13: Drag gains of GETS model with various radii at Re=24,000 & 48,000 compared to simulation at Re=8,000 with N=46

The change in front-edge radii is also observed in the pressure coefficient. Figure 3.14a show the pressure distribution of the front for various front-edge radii. As the radius increases the minimum pressure coefficient moves gradually to the outer edges. Whereas the smallest curves edges, with the large stagnation surface, has a more abrupt decrease of the pressure. This might be the cause of the flow separation and the steep velocity increase near the edges.

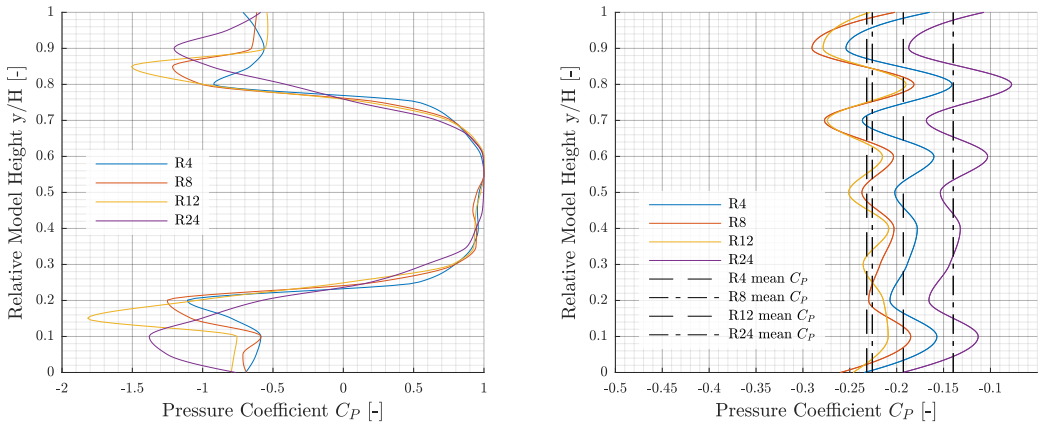

(a) Pressure coefficient front z=0.5W

(b) Pressure coefficient rear z=0.5W

Figure 3.14: Time-average pressure coefficient at the front and rear of a GETS model with various front-edge rounding at a Re=24,000 with N=46

The difference in wake structure between R4 and R24 at a Reynolds number of 24,000 is not that large as can be seen in Appendix B where more contour plots of various configuration can be seen. The pressure coefficient plot in Figure 3.14b already shows that the flow phenomena are comparable only the magnitude is slightly dissimilar. In Appendix C the pressure plots of more configurations and Reynolds numbers can be seen.

The Reynolds number effect is very well visible at the front of the model. The laminar separation bubble decrease in size when the Reynolds number increases. Figure 3.15 shows a R24 model at two distinctive Reynolds numbers, 8,000 and 48,000, respectively. At a low Reynolds number the flow is attached longer to the surface this means that a more elongated bubble appears, see Figure 3.15a. Higher Reynolds number promote earlier transition within the bubble and therefore shorting it. A higher Reynolds number increases the turbulence intensity levels in the boundary layer and hence the separated bubble reattached itself to the

surface again, as can been seen in Figure 3.15b. In general, increasing the Reynolds number also increases the turbulence intensity which in return makes for a smaller bubble. More contour plots of different configuration and other Reynolds number are illustrated in Appendix B.

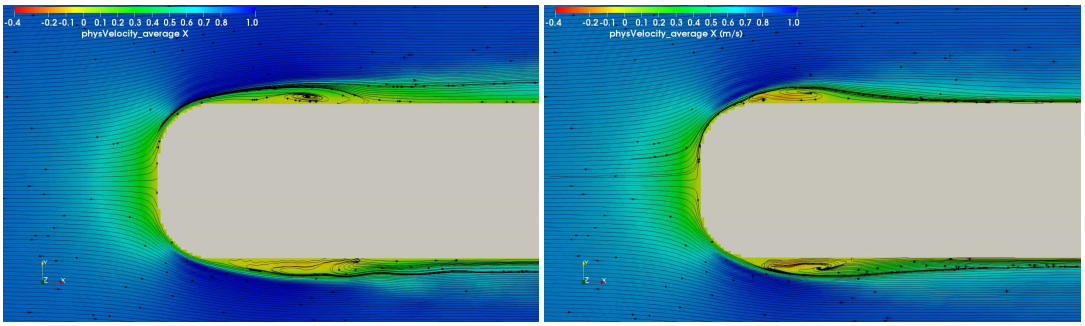

(a) Re=8,000 (b) Re=48,000

Figure 3.15: Time-average illustration of the separation bubble behavior for a R24 model at a Re=8,000 & Re=48,000 with N=46

3.3.5. Effect of Tails

Next step in the investigation the flow behavior and its influences on drag and pressure distribution is the addition of a tail. The GETS model was equipped with 6 different tail. Due to EU regulations, the horizontal length of the tail is limited to 1.5m for the full-scale model so this means that for the 1:50 model the length of the tail will be 30mm. Four different tail angles are used: 6°, 12°, 15° and 18° with a 30mm length. Furthermore, the effect of a shorter tail is investigated. The horizontal length of this shorter tail is 10mm with two tail angles: 12° and 18°. The addition of a tail at the rear-end has the same effect as changing the front-edge radii. Simulation of the wake is of equal importance as the front. A large part of the drag contribution originates in the wake at the rear of the model. Therefore, it is crucial that the flow in the wake in simulated correctly and the flow properties match that of literature. A fundamental flow phenomenon that a wake of such a bluff body contains is the toroidal recirculating region, in which a vortex ring is present. This phenomenon was found by Krajnović and Davidson [40], Ortega et al. [62]. When the flow over the sides enters the wake it is decelerated and drawn in the vortex. There is a suction motion where the flow is reversed and stagnates at the rear surface of the model. This recirculating motion generates two large vortices of un-equal strength, this is also known as the pumping effect. This specific phenomenon is an important aspect in the validation of the flow simulation with *OpenLB*.

R8 base model compared with additional tails

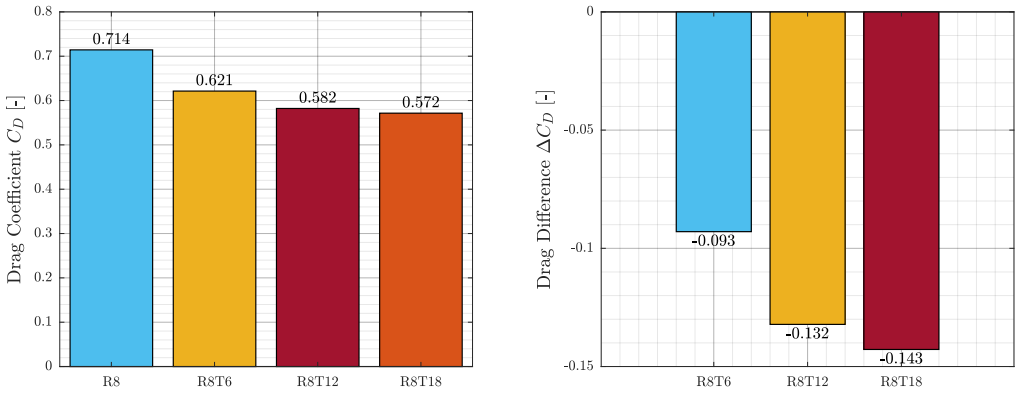

(a) Drag of R8 with various tails (b) Drag difference of R8 with tails compared w.r.t. too the base model R8

Figure 3.16: Numerical drag coefficient and drag difference of R8 with tails angled a 6°, 12° and 18° at Re=24,000 with N=46

In Figure 3.16a the drag coefficient of an R8 model with and without tails is given. The tails used is the simulation are angles at 6°, 12° and 18°. Furthermore, Figure 3.16b the drag difference between the R8 base model and the addition of a tail is given. A clear trend that is visible is that with increasing angle of the tail the drag reduces. Applying a tail of 6° the model loses 93 drag counts (13%). For a tail of 12° a drag reduction of 132 drag counts (18.8%) was measured. For the tail with the steepest angle of 18° the drag loss is 153 counts (21.5%). [20, 78, 80] have also tested the same GETS model with the additional tails at the same angles. Comparing the results of the current study with that of the reference studies it can be concluded that the drag reduction is less with the current study. The main reason for this is that the numerical simulations of the full-scale model are performed at a much higher Reynolds number. At high Reynolds numbers, the pressure drag is a much larger part of the total drag so an addition of a tail is more beneficial at these higher Reynolds number than at lower. The trend that is visible in Figure 3.16a, that with a larger angled tail more drag is reduced is not an obvious one. The steepness that comes with a larger angle is not always beneficial. If the angle is too large the flow will separate and reduce the effectiveness of the tail, as can be seen in Figure 3.16b. From Figure 3.18d it shows that there is separation of flow over the tail, this is because the angle is too large and the flow can not follow the contour of the tail anymore. This reduces the effectiveness of the drag reduction device. However, this does not reflect on the drag coefficient found in Figure 3.16a, so a critical attitude against the result needs to be taken.

In Figure 3.17 the pressure coefficient at the front and rear of the model is plotted. The addition of the tail certainly has an effect on the pressure distribution over the rear-end of the model. From Figure 3.17b it can be seen that an increase in tail angle causes the base drag to rise, this leads to a reduction in pressure drag at the aft part of the model. Surprisingly, there is no major effect seen at the front pressure distribution in Figure 3.17a. Although, the effect of the tail is not visible in the pressure plot there is an effect that the tail has on the separation bubble on top and bottom of the model, this effect is shown further on in this chapter. There is indeed no effect of the tail visible on the front-end pressure distribution, however, this is only true for the R8 models for the R24 models there is some effect of increasing velocity and reduction of the separation bubble. This could be the cause of the thick boundary layer that is generated by the sharp edge. The pressure plots of the R24 models are illustrated in Figure C.8a of Appendix C.

To fully understand how the flow behavior is with the application of a tails aft of the base model, a contour plot with streamlines gives a good insight into various aerodynamic phenomena. In Figure 3.18 the contour plots of the R8 base model and the additional tails are animated. With the animation, the transient behavior of each configuration can be viewed in more detail. The propagation of the flow with the additional vortices, that are generated by the rear part of the body, can be studied in more detail. As van Raemdonck [78] clearly stated in his work, that with the addition of a tail the flow separation occurs further upstream. In addition, a carefully chosen tail, with the right slant angle, narrows the wake by following the contours of the tail. These effects cause the wake to be smaller and the pressure to rise, which in turn reduced the pressure drag. The observation of van Raemdonck [78] can partly be seen in Figure 3.18.

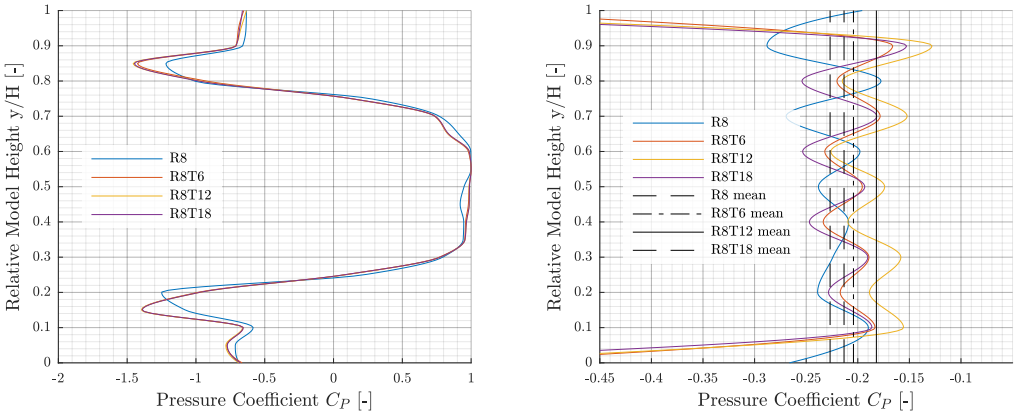

(a) Pressure coefficient front z=0.5W

(b) Pressure coefficient rear z=0.5W

Figure 3.17: Time-average pressure coefficient of R8 with tails angled at 6°, 12° and 18° at Re=24000 with N=46

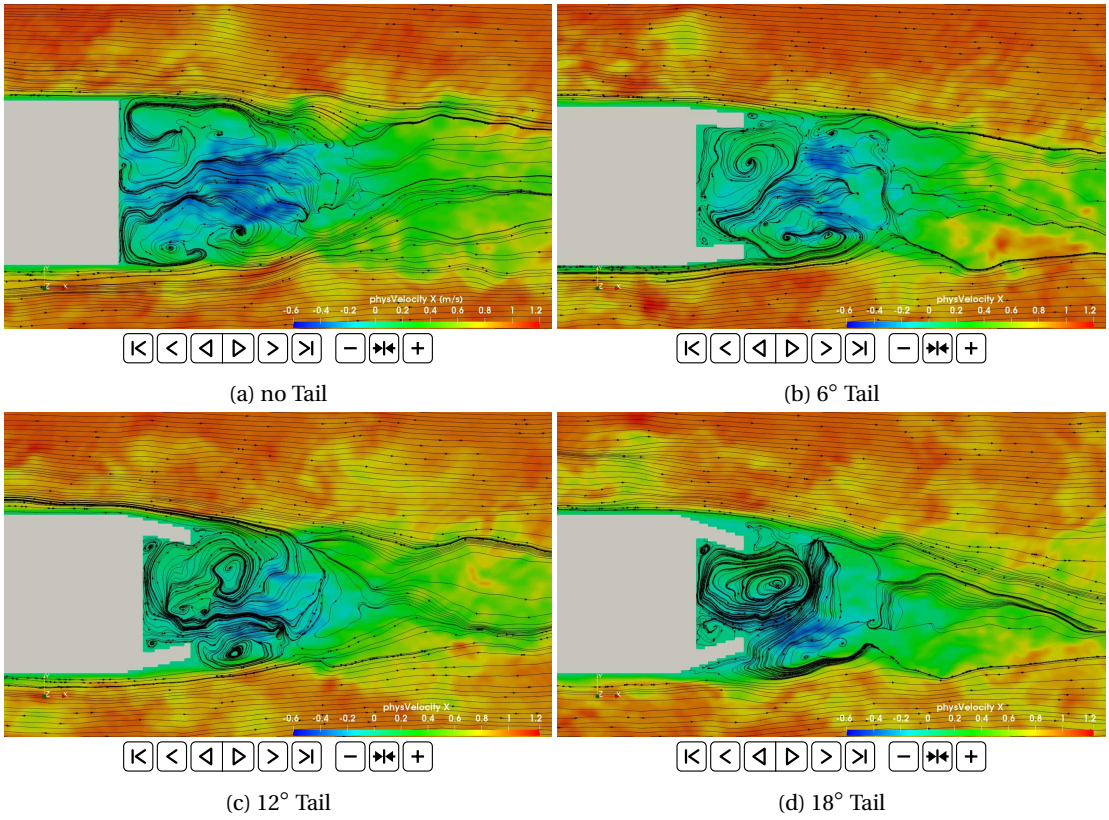

(a) no Tail (b) 6° Tail

(c) 12° Tail (d) 18° Tail

Figure 3.18: Animated numerical contour plot of the x velocity with streamlines for R8 with tails angled at 6°, 12° and 18° at Re=24,000 with N=46

Effect of various front-end rounding and tail angles

In addition, a selected few tails are simulated for this study. This is mainly because simulations cost a large number of resources and time. So a selection of various tails has been made. The selection procedure is mainly based on the wind tunnel tests,conducted in Chapter 4, from which interesting trends are investigated by means of simulations. The configurations that have been considered are: R4t18, R8T18, R12T6 and R24T12. The capital T stands for the long tail and the small letter t stands for the shorter tail. These configurations represent a wide range of flow phenomena that are interesting to investigate. The drag of these configurations can be seen in Figure 3.19.

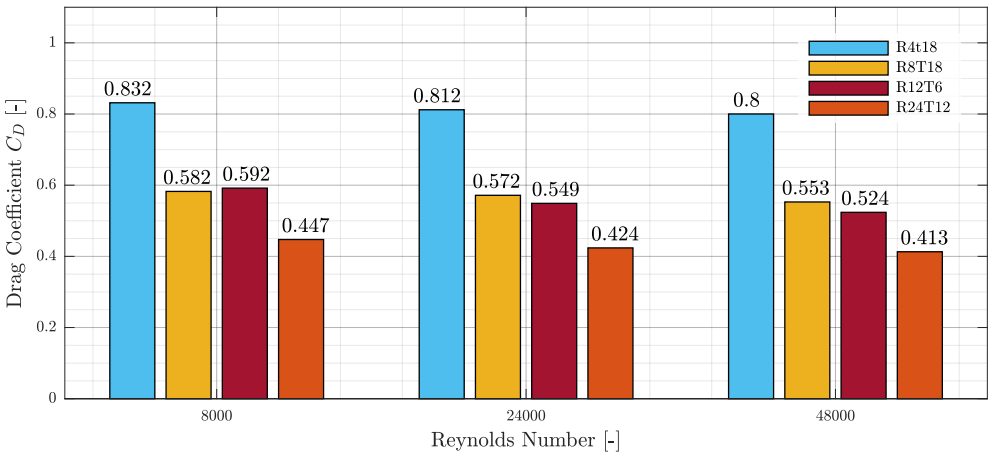

Figure 3.19: Drag coefficient of a GETS model with various rear-end drag reduction devices at a Re=8,000, 24,000 and 48,000 with N=46

As seen in Figure 3.12, the model with the smallest front-edge radius performs the worst when it comes to drag. The opposite applies to the front-edge with the largest radius. The R24T12 configuration has almost half of the drag when compared to R4t18. The combination of the front-edge rounding and a more effective tail has a considerable influence on the efficiency of drag reduction. Furthermore, regarding the other two configurations, R8T18 & R12T6. They seem to have the same effect on the drag reduction capabilities.

To see what the effect of the tail is compared to the base model with the same front-end rounding a drag difference is plotted in Figure 3.20. Here the values of Figure 3.19 and Figure 3.12 are subtracted for the same Reynolds number. The drag difference between the base models and the models with a tail are virtually constant for the different Reynolds numbers. Moreover, the addition of a tail gives a drag reduction, no matter the tail. The shorter tail with an angle of 18°, t18, gives the least drag gain. Whereas, the largest tail angle gives the largest drag reduction.

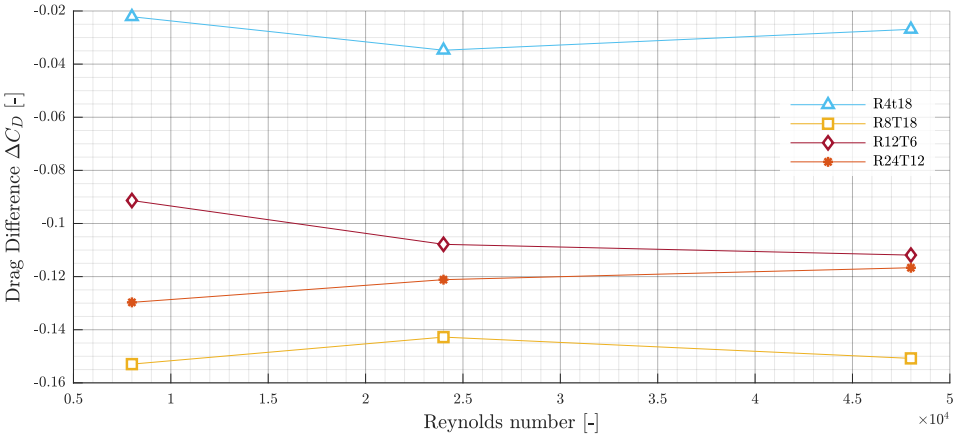

Figure 3.20: Numerical drag difference between the base model and model with tail with N=46

The tail has not the only influence on the flow behavior on the rear of the model but also at the front of the model. Because the flow follows the angle of the tail, it is accelerated. This same phenomenon occurs on airfoils with a flap, where the flow is increased due to the flap and the boundary layer is longer attached to the surface giving it a higher lift at lower velocities. With the addition of the tail, the boundary layer at the rear is accelerated and therefore pulls the flow over the entire model. The pulling motion gives the boundary layer more energy, "energizing" the flow, and this affects regions of low velocity. In these regions of low velocity often a laminar separation bubble is present, so increasing the boundary layer velocity shrinks the bubble and counters the effect of the adverse pressure gradient. This results in less drag contribution from the front. The mechanism is very well illustrated in Figure 3.21. Where the front-end velocity contours with streamlines of an R24 base model is compared to an R24 with a 12° tail attached. The effect of other tails on the separation bubble can be seen in Appendix B.

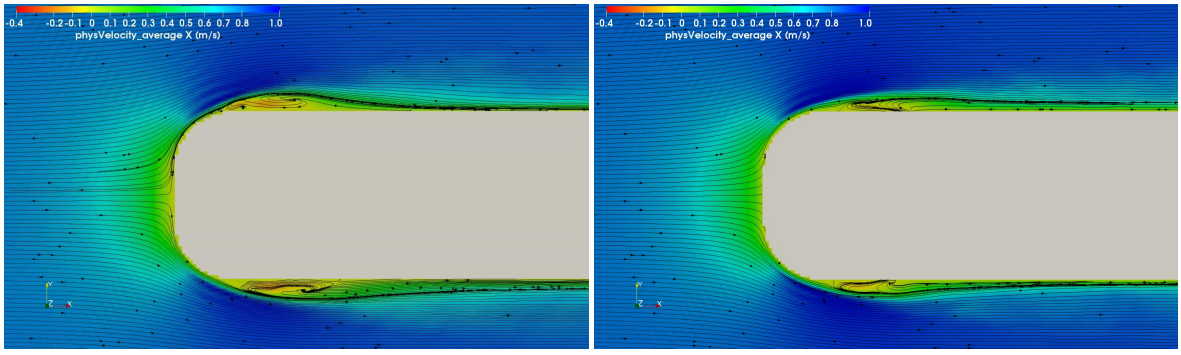

(a) R24 at Re=48,000

(b) R24T12 at Re=48,000

Figure 3.21: Time-average illustration of the separation bubble behavior for a R24 base model and R24T12 with tail at Re=48,000, with N=46

4

Experimental Analysis

4.1. Experimental Setup

Generating data to validate the numerical LBM simulation a small wind tunnel, named the M-tunnel, of the faculty of Aerospace Engineering at the Delft University of Technology, is used. Furthermore, the wind tunnel overview and test setup are shown and explained in more detail. The choice of the front-end rounding and rear-end devices are substantiated with proven concepts but also with a few new insights.

The M-tunnel is a model tunnel at the low turbulence tunnel faculty and is quite extraordinary because it can function as an open jet or a closed wind tunnel. Depending on the configuration, open jet or closed, the maximum velocities are 35 m/s and 50 m/s, respectively. The test section is a 40cm by 40cm square and due to its large contraction ratio, the turbulence levels are quite low. The wind tunnel is used to research drag reduction techniques in turbulent boundary layers of flat plates, basic studies on wind effects on buildings, but also drag measurement on bluff bodies.

4.1.1. Model Setup in Wind Tunnel

In Figure 4.1 the wind tunnel setup is illustrated. With the model in the test section on a rod that is connected to the force balance, recognizable in yellow and blue, placed under the test section. The dimension of the test set up are illustrated in Figure 4.2. The model is slight off-center and this has to do with the pre-drilled, also the slight aft position of the model in the test section has to with that.

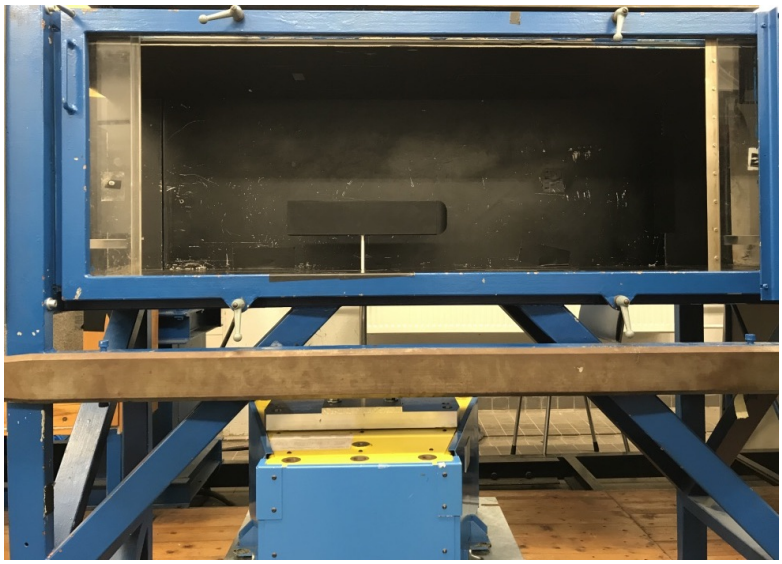

Figure 4.1: M-tunnel test setup with model attached to the force balance

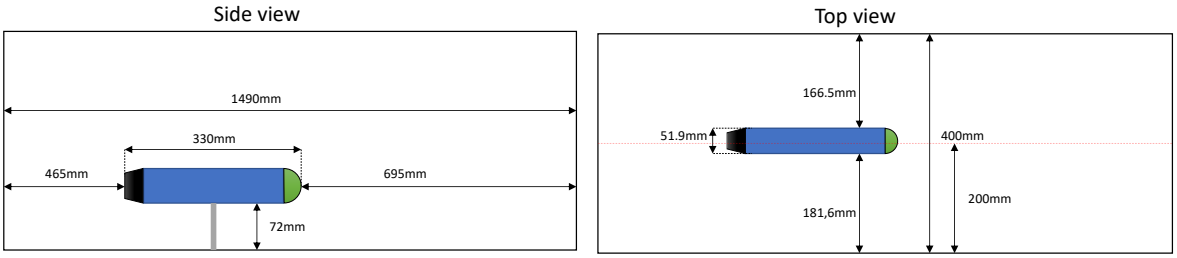

(a) Side view of the model with all the dimensions

(b) Top view of the model with all the dimensions

Figure 4.2: Position of the model w.r.t. to the inlet. With all the dimensions from the side and top view

The position underneath the wind tunnel test section is not ideal, nor spacious. Due to the space restriction, the balance needed to be placed on the structure of the wind tunnel. This subsequently means that the vibrations of the fan will have an influence on the measurements. By raising the force balance and placing it on foam pads improved the measurements, however, this is still not ideal to have reliable and accurate results. Moreover, the rod which connects the model to the balance is made out of aluminum, this is a relatively flexible material in these circumstances. To prevent that the force would be absorbed by the rod rather than by the balance it was reinforced by a stud. There are a great number of factors that played a role to achieve a reliable result as possible.

4.1.2. Front-Edge Rounding

Front-end rounding influences the flow over the entire length of the body so it is imported to investigate which radius has the most impact on reducing the drag. The test is performed at low Reynolds number so for a full-scale application it does not give the satisfactory results that are desired. It demonstrates a useful data collapse from which the optimal front-end radius, for a box-like vehicle shape, can be chosen for a full-scale Reynolds number. The intent for this test is not to have a quantitative comparison of how the radius influences the drag but more to demonstrate how low Reynolds numbers wind tunnel test data can be used to make a choice of the best front-end geometry at full-scale. Furthermore, this is not the only reason to test various front-ends with low Reynolds number, since the *OpenLB* uses a sub-scale LES model to simulate turbulent flows, this limits the method to primarily modeling of low Reynolds number flows. The Reynolds number range is specifically chosen to comply with the limitations of the method and model. The dimensions and radii of the various front-ends used in the test, as seen in Figure 4.3, is a straight result of this. In Figure 4.3 the various front-ends that are tested in the wind tunnel can be seen. The radii are chosen to facilitate a wide range of front-ends to get inherently different flow phenomenon that can be observed.

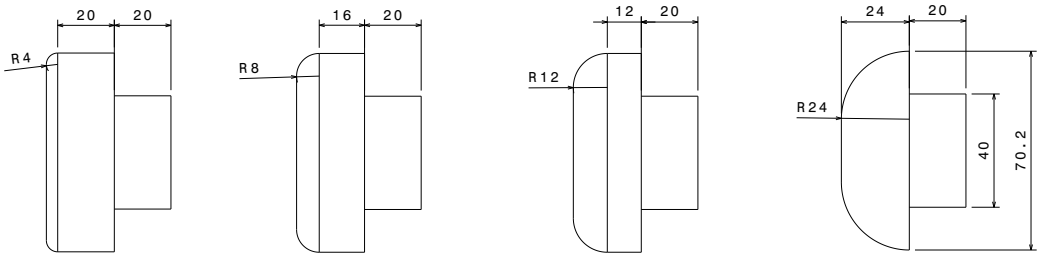

Figure 4.3: Front-end rounding variation

The smallest radius is chosen from an equation that is used to guarantee laminar flow over the front.

$$Re_{crit} = \frac{U \times r_{crit}}{\nu} \tag{4.1}$$

Where the critical Reynolds number is $Re_{crit} = 125000$. The kinematic viscosity is chosen at $20°C$ which gives a $\nu = 1.511E-5m^2/s$. The velocity is set to $U = 10m/s$ so that it would not exceed the Reynolds number limits. This gives values to all the variables shown in Equation (4.1) are known know and therefore the critical radius can be determined in de following equation. The critical radius to obtain laminar flow is for the 1:50 scale model and can be seen as the most far left object in Figure 4.3

$$Re_{crit} = \frac{U \times r_{crit}}{\nu} \Rightarrow r_{crit} = 4mm \tag{4.2}$$

4.1.3. Rear-end Drag Reduction Devices

To investigate the optimum drag reduction device a selection of four different rear-end shapes are used for the study. In Figure 4.4 the rear-end attachment can be seen with a varying angle. The flap angles vary with angles of 6°, 12°, 15° and 18°. These angles are constant along the whole circumference of the rear of the base model, keeping the horizontal lengths at a set value of 30mm at a scale of 1:50. At full-scale, this would be 500mm which is the maximum that is allowed in Europe[16]. In addition, smaller rear-end devices are tested with the purpose of investigating the effectiveness of these smaller devices. The smaller devices are 10mm at the same 1:50 scale as the larger ones, however, there are only two angles, 12° and 18°, tested to obtain a basic effect of the shape on the drag and flow around the body.

The measurements of the devices as shown in Figure 4.4 are similar to that of the base model where they are attached to. The devices are attached using regular office tape because it is thin and strong enough to hold it in place, but also not to disturb the flow ahead of the device and to close any gaps that may occur. The rear-ends are cut into four sections, representing the longer side pieces and the shorter top and bottom pieces, with a waterjet and soldered together.

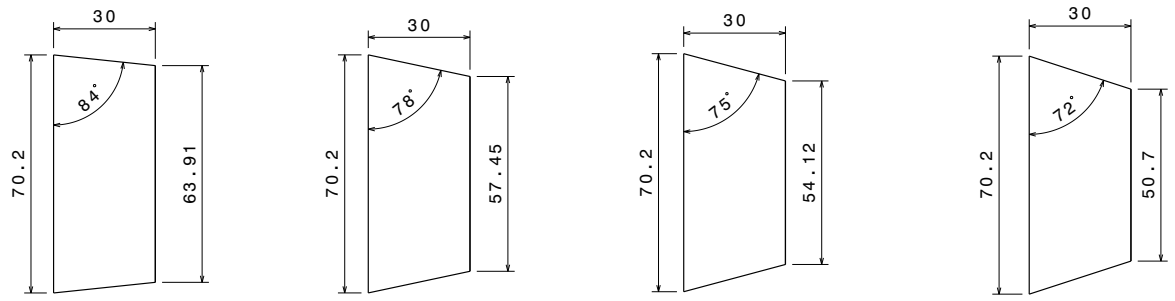

Figure 4.4: Rear-end angle variation

4.1.4. Wind Tunnel Tests

The objective of the wind tunnel test is to obtain force data that can be compared with numerical results. The forces are measured using a forces balancer that is administrated by the Dutch Aerospace Laboratory (NLR) and used in the wind tunnels of the Delft University of Technology. Moreover, flow visualization technique using oil is also performed to envision the streamlines across the various front-end rounding and rear-end angles and/or both influence each other.

Drag Measurement

The force balance measures the force in x-, y- and z-direction but also measures the moment around those axes. The maximum load is around $\pm 250N$, this makes the balance highly qualified for medium to large wind tunnels and models. This is an issue for small models at lower velocities because the uncertainty of the measurements become larger. The standard error margin that is set by the NLR after calibrating the force balance can be seen in Table 4.1, according to [1]. Being in the lower spectrum of the force measurements capabilities gives some insecurities, which have to be noted and taken into account during the analysis of the data.

Table 4.1: Error margin of the force balance for force and momentum

Force		Momentum	
	ϵ [%]		ϵ [%]
F_x	0.06	M_x	0.05
F_y	0.23	M_y	0.05
F_z	0.16	M_z	0.25

Signal measurements are set at a rate of 50000 Hz over an average of 60 second time period to obtain a single measurement. The averaging of the data is essential to filter the peaks out of the unsteady data that is highly oscillatory. Bluff bodies tend to have an unsteady aerodynamic nature, so to manage this behavior and collect valuable data signal averaging needs to be applied.

4.1.5. Test Model Accuracy

The base of the model is made out of plywood. The front-ends with various radii is milled from a block of plastic to have the precise measurement that it is designed for. Hardest to produce were the tails. Due to the size of the metal components, it could not be welded, so it was chosen to solder it. Although the drawing indicates the right measurements of a design it is never the case that a model is exactly the correct size. This also applies to the model that is used in the wind tunnel. The plywood has a certain roughness that can trigger early separation and the tails are soldered by hand, so the angles are not exactly the right value. Furthermore, the tails are added to the rear of the base model with tape which creates an edge between the model and tail. These inaccuracies are not disastrous for the measurements, however, it needs to be taken into account that these could have an effect on the measured values and need to be accounted for in the validation of the model.

4.2. Experimental Results

In the plots, the radius of the front-end is marked with a capital (R) followed by the radius in mm. The rear-end devices are denoted with the letter T, capital for the long version and small for the shorter version. So as an example, a 4 mm radius at the front and 18° flap angle at the rear-end would be written as: R4T18, and with the shorter version, it would be: R4t18. This section will discuss the effect of the fluctuation on the measurements. Furthermore, the drag coefficient of all the possible combinations of front-end rear-ends is given with respect to the Reynolds number. The Reynolds number effects on the various geometries are investigated and this is connected to literature to make sure the measurements make sense. To make sure the measurements are consistent every time and no unexpected divinations occur during each test or during the change of geometry, several retests are performed to estimate the error margin.

4.2.1. Wind Tunnel Velocity Fluctuation Effects

The column of air that is generated by the wind tunnel is never constant, there are always fluctuations in the air velocity. This instability of the wind tunnel can have an influence on the measured force that is applied to the model. In Figure 4.5 the velocity of the wind tunnel, that is measured with a pitot tube, and the measured force by the force balance are plotted. From the figure is it can be seen that the velocity fluctuation are rather small and don't have a large influence on the measured force. The oscillation of the force does not follow the velocity fluctuation in amplitude.

The oscillation that is measured by the force balance is partly from the wind tunnel itself, due to the limited space and the position of the model the force balance was constrained to the position on the base of the wind tunnel test section. This is a part of the wind tunnel and therefore resonates the propeller vibrations to the balance. There have been attempts to damp the vibration by placing the balance on foam pads, this had significant improvement in suppressing the noise. Nevertheless, the measurements were satisfactory and could be used to investigate the influence of the various front and rear-ends on the drag coefficient.

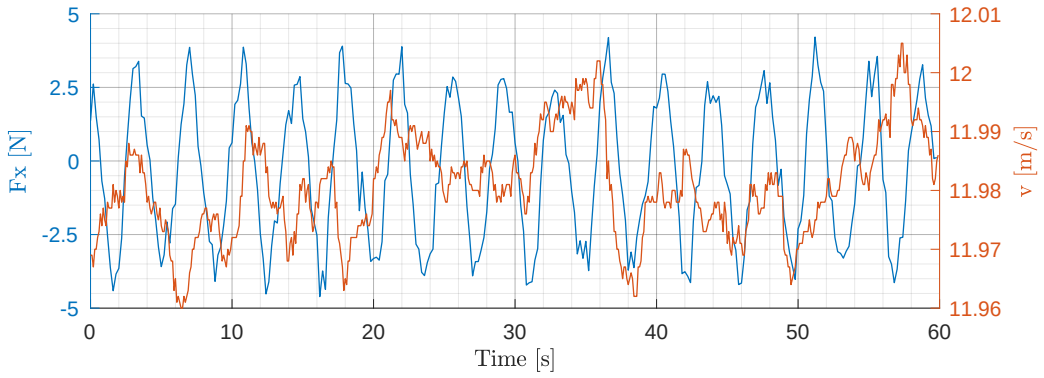

Figure 4.5: Effect of velocity fluctuations on the measured force in x-direction by the force balance

4.2.2. Error Margin

The force balance used to measure the forces that act on the model is not build to measure these small forces as with this test. The tests are performed at the lowest limit of the balance and to make sure that the tests are consistent every time, certain configurations are retested to determine what the error margin is, and if there are major variations in the measured forces. In Figures 4.6 to 4.9 the retest are show in graph form, each plot the front-end is constant and the rear-end device is changed. Often only two tests of the same configurations are performed, however, if there is a major deviation between the runs, as in Figure 4.6, more runs are carried out to make sure there is consistency in the measurements.

The largest drag uncertainty is found with the smallest front-edge radius, according to Figure 4.6. In Table 4.2 the mean and standard deviation of an R4 model configuration is given at various Reynolds numbers. The data to calculate the mean and standard deviation is obtained from the retests of Figure 4.6. There is a downward trend of the drag coefficient with increasing Reynolds number, this is also the case of the standard deviation. This means that with increasing inlet velocity of the wind tunnel the obtained results are within a smaller band of uncertainty. For most of the model configurations this trend is true, however, for the R4 there is a larger spread of measured results. This could be as a result of the small front-edge radius. With a small radius it is hard to maintain a large section of attached flow, this makes the flow over the front-end is very unsteady and therefore very random in certain cases. This is the reason that there is a widespread of results for the R4 configuration. To be on the conservative side, the standard deviation of the base model with a 4mm front-edge radius is taken to account for the uncertainty of all the measured drag coefficients.

Table 4.2: Drag uncertainty of the GETS model with a R4 front-end at various Reynolds numbers

Run	**Drag Coefficient** C_D [-]			
	Re=8000	Re=24000	Re=48000	Re=60000
1	1.0421	0.9848	0.9679	0.9503
2	0.8489	0.9194	0.9452	0.9351
3	0.9743	0.9117	0.9060	0.8925
4	1.0710	0.9509	0.9280	0.9117
Mean	0.9841	0.9556	0.9416	0.9224
Standard Deviation	0.0988	0.0578	0.0318	0.0255

First thing that stands out if looked at Figures 4.6 to 4.9, is that with a larger leading-edge radius the measurements inaccuracy is significantly less throughout the whole Reynolds sweep. This can be the cause of longer attached boundary layer with the larger radius, the advert pressure gradient is lower and there is no sudden burst in the flow bubble, hence making it less uncertain in how the flow over the model behaves. The opposite is true for the smaller leading-edge curvature. There is higher adverse pressure gradient and this makes the flow over the front of the model less predictable and this reflects on the measured values in Figure 4.6. This seems mostly applicable on the R4 front-end without a tail.

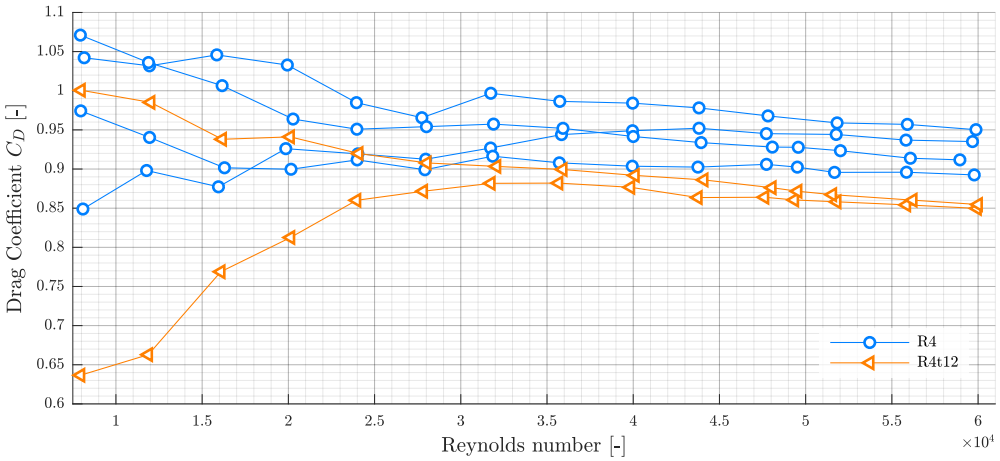

Figure 4.6: Drag coefficient of multiple retests with 4 mm front-end and various rear-ends

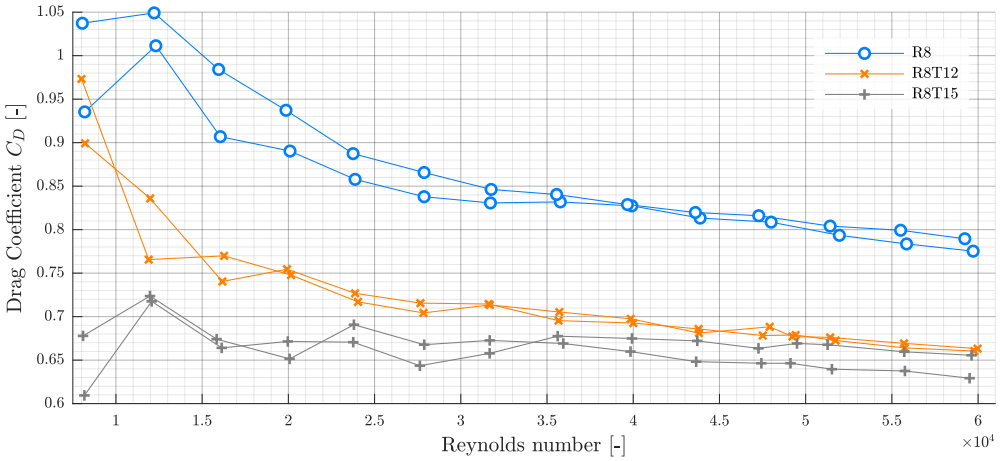

Figure 4.7: Drag coefficient of multiple retests with 8 mm front-end and various rear-ends

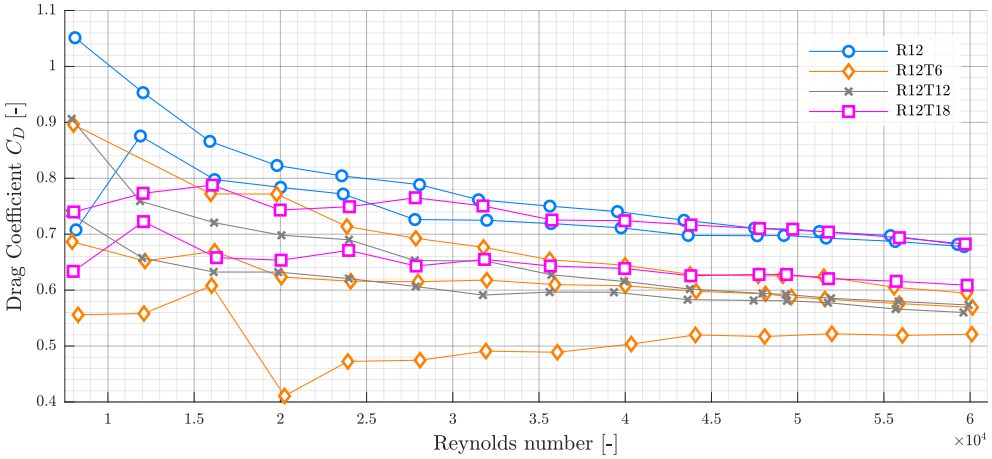

Figure 4.8: Drag coefficient of multiple retests with 12 mm front-end and various rear-ends

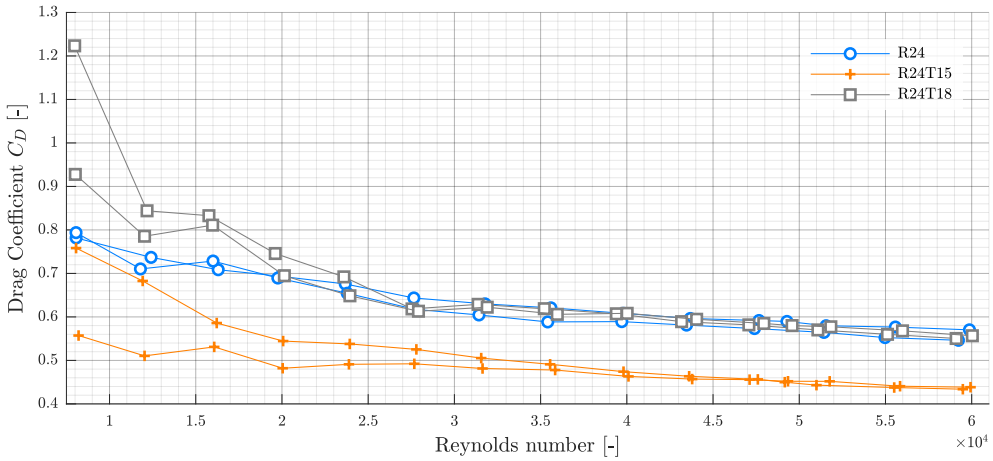

Figure 4.9: Drag coefficient of multiple retests with 24 mm front-end and various rear-ends

4.2.3. Reynolds Number Sweep

A Reynolds sweep is performed to get an overview on how the shape of the bluff body and the Reynolds number have an influence on the drag coefficient. To change the Reynolds number during the test, the wind tunnel inlet velocity was altered to increase the Reynolds number. The results of the sweep are given in Figures 4.10 to 4.13. In the four plots that are presented below, the front-ends are kept constant and the rear-ends are changed to observer how the constant front influences the aft and vice versa.

Considering Figure 4.10 with a front-end of 4mm, a very clear trend can be seen. At a low Reynolds number, the drag is at its maximum and decreases with increasing inlet velocity. Furthermore, the decrease of C_D is not as drastic at higher Reynolds numbers as with the lower ones, this can be a result of the accuracy of the force balance at very low forces. At the lowest Reynolds number of $Re = 8000$ or $2m/s$ inlet velocity, there is a lot of discrepancy with the decreasing drag coefficient or increasing Reynolds number. These inconsistencies are visible with every test and measurements, see Figures 4.10 to 4.13. It looks like that with the increasing velocity of the wind tunnel the force on the model is more constant comparing with low velocities. Although this is an obvious statement the consequence is not trivial. In the previous section more is already explained in how the error margin of the various tests are observed and what the impact of measurement error is on the results.

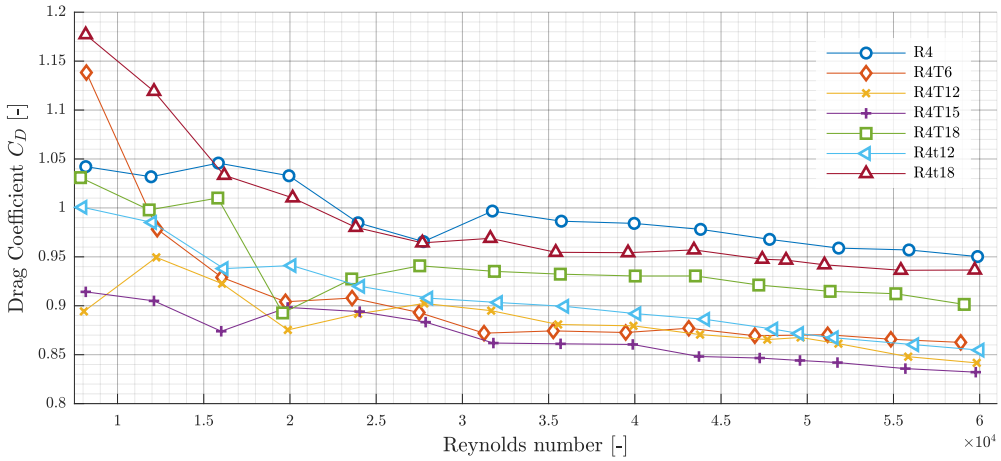

Figure 4.10: Reynolds number sweep for model configurations with front-end radius of 4 mm

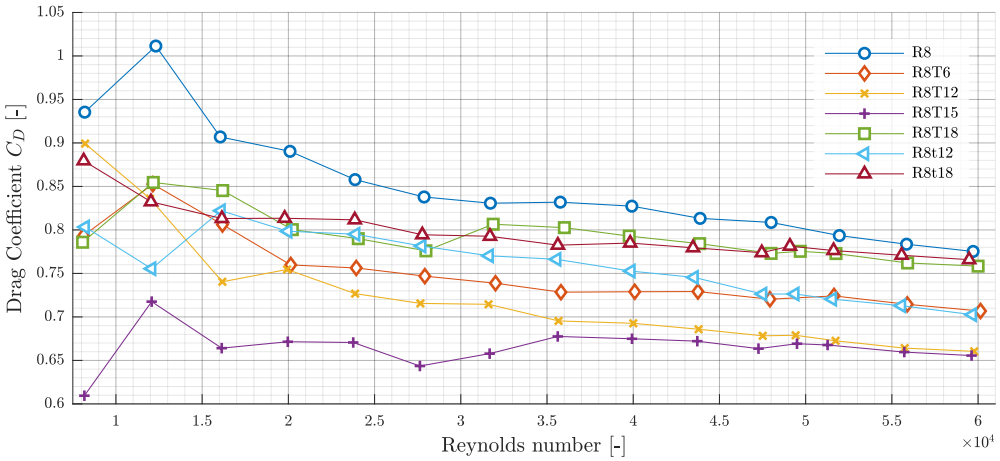

Figure 4.11: Reynolds number sweep for model configurations with front-end radius of 8 mm

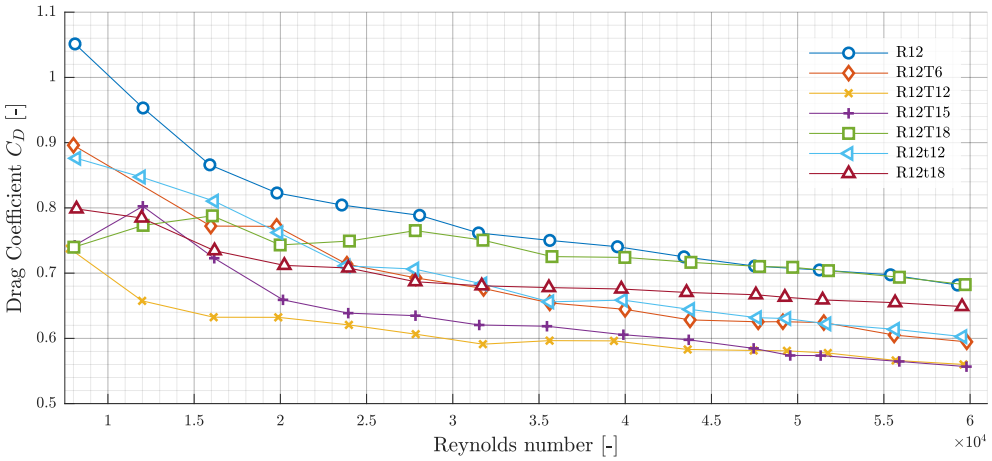

Figure 4.12: Reynolds number sweep for model configurations with front-end radius of 12 mm

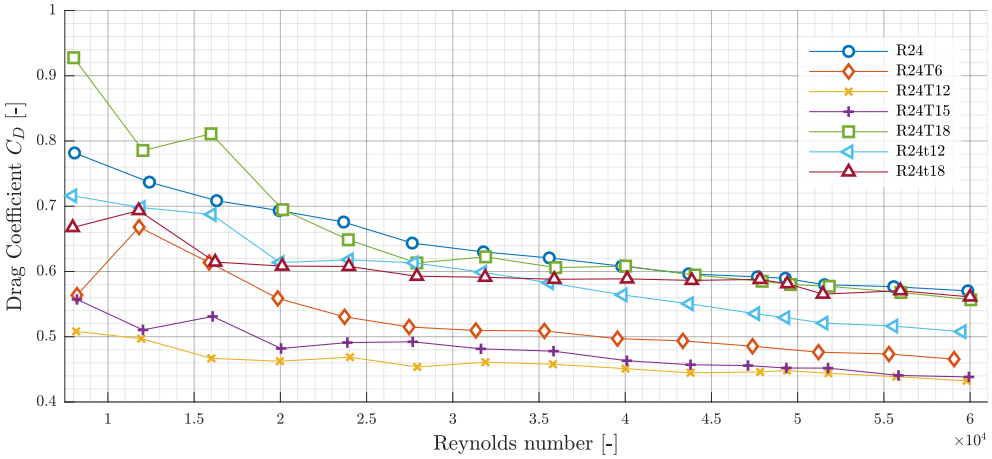

Figure 4.13: Reynolds number sweep for model configurations with front-end radius of 24 mm

In all the figures of the Reynolds sweep something remarkable can be observed. There are three trending groups that the measurements converge to. This is very well visible in Figure 4.11, where the rear-ends with an angle of 18°, both the long and short version (T18 & t18), together with the base model form the first group. The second group consisting of the long rear-end with an angle of 6°(T6) and the short version of 12°(t12) drag reduction devices. The last group, that has the best aerodynamic performance, are the rear-end modification with an angle of 12° & 15° (T12 & T15). With this observation, it can be concluded that the use of T18 or t18, as a rear-end drag reduction device, is just as effective as the base model without these devices. In addition, the T12 and T15 are the most efficient by reducing the drag and this is true no matter what the front-end radius is. Furthermore, the small front-end radius causes the flow in a sub-critical region to separate earlier and create a large area with high drag, this is considerably less when a larger front-end radius is used. A clear comparison can made if Figures 4.10 and 4.13 are compared.

4.2.4. Drag Difference

In Figures 4.14 to 4.17 the drag of the base models are subtracted of the configurations with tails. This gives the drag reduction effectiveness of the tail. The addition of a boat tail to the rear part of the model shows that there is drag reduction over the entire range of slant angles and tail lengths, with an exception of one or two configurations. This shows that that addition of tail has beneficial effects no matter what the front-edge radius is and no matter the tail angle. However, there are degrees of efficiency. As discussed before there are three main groups at which the drag difference converge to. According to the findings of Yi [89], for a tail of 15° a drag coefficient reduction of 130 drag counts can be achieved compared to no tail. In the experiments, it can be seen that this is indeed the case of the tails of 12° and 15°, as the Reynolds number increases, the drag coefficient moves to a constant value. At low Reynolds numbers, there are somewhat chaotic results. The issue with this already covered in the previous sections. So If we only look at higher Reynolds numbers the observation of Choi et al. [10] justifies the results. Only Figure 4.14 where a front-edge radius of 4mm is used there is somewhat deviation to that observation. No matter what tail is mounted on the base of the model the differences between tails are not that prominent as with the others. This could be due to the sharp edge which reduces the effectiveness of the tails.

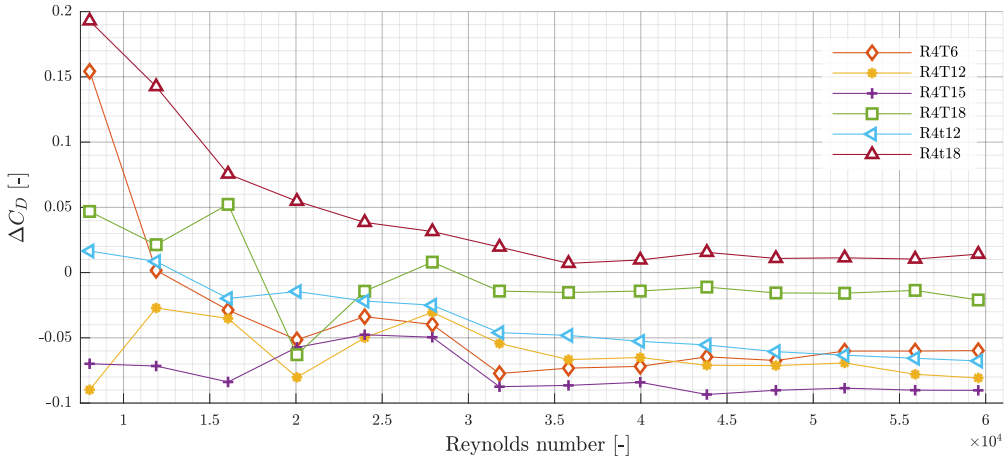

Figure 4.14: ΔC_D of an R4 with various boat tails

The trend seen at the front-edge rounding is also seen with the drag difference. The best results are gained with a radius of 24mm and either a 12° or 15° tail. The separation at the front helps the flow to stay attached to the body so when it reaches the tail it is not disturbed and therefore performs better. It must be said that with a front-edge radius of 8 or 12mm similar difference are found, although the reduction of an addition tail is comparable the base drag is larger so the overall drag coefficient is still higher. All in all, Figures 4.15 to 4.17 show that the effect of the tails are comparable not matter the front-edge radius.

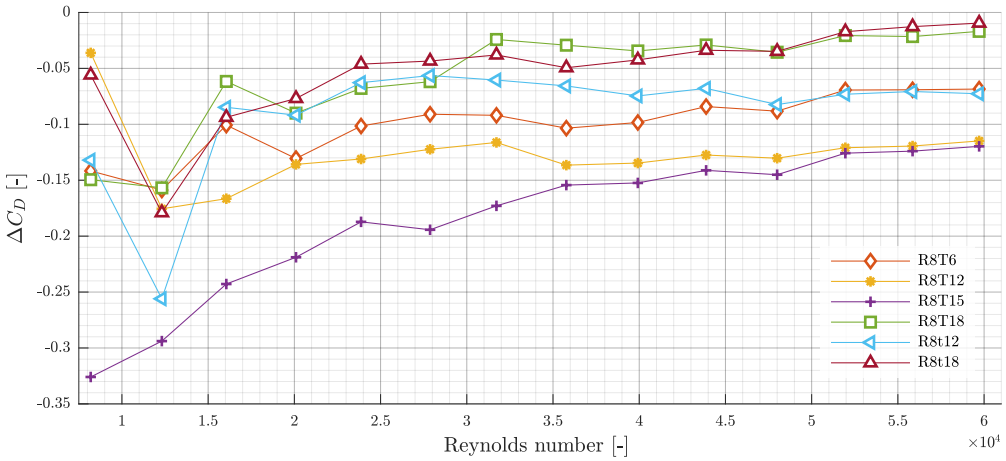

Figure 4.15: ΔC_D of a R8 with various boat tails

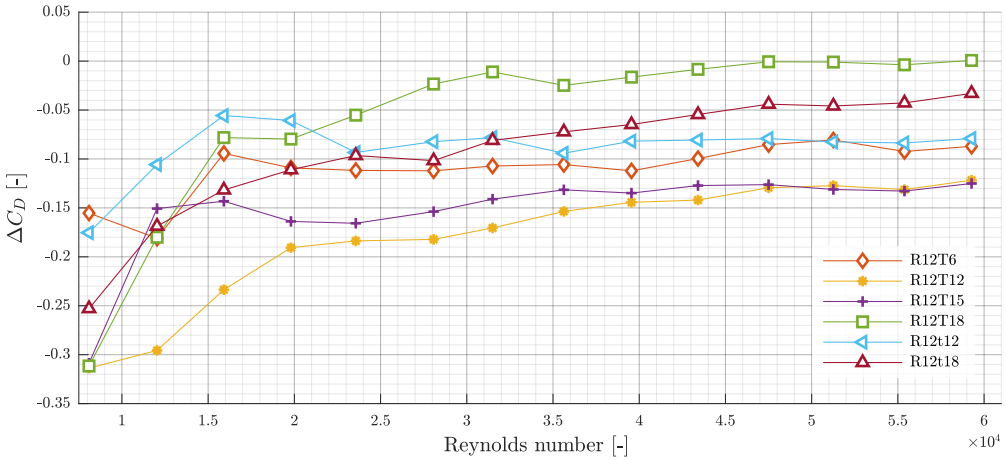

Figure 4.16: ΔC_D of a R12 with various boat tails

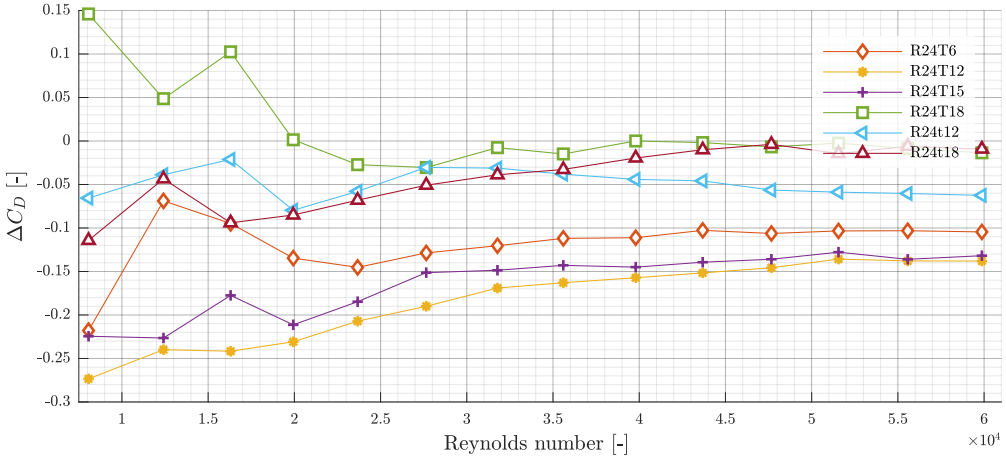

Figure 4.17: ΔC_D of a R24 with various boat tails

5

Discussion of Results

In this chapter, the numerical and experimental results are discussed. The obtained results from both analysis approaches are compared with each other, but also to literature. An explanation of the difference between the numerical and experimental results is given on the basis of gained experience working with *OpenLB* and applying knowledge derived from literature. The guideline throughout this chapter will be the subquestion that is presented in Section 1.4.

5.1. Drag Comparison of Numerical and Experimental Analysis

There have been many studies performed on the GETS model, both numerical and experimental [20, 78–80]. These studies are conducted on either a full-scale model, numerically, or scale model, experimentally. Very useful results are obtained from these studies regarding, the influence of front-edge rounding and rear-end modification on the drag contribution. In addition, the change in flow behavior due to these adjustments are presented in these studies. Unfortunately, it can not be fully used in the present study mainly because a much higher Reynolds number is used and further the model scale is also multiple magnitudes larger than in the present work. Although, the scale and simulated conditions are different the trends and flow characteristics can be compared to validate the obtained results.

The first subquestion that is discussed in this chapter is the drag. A juxtaposition of the numerical and wind tunnel drag coefficient determination is performed. The effect of the front-edge radius and rear-end modification is shown and how they relate to the obtained results from both analysis methods. Finally, a few possible factors that have an influence on the drag determination of both analysis methods are discussed.

5.1.1. Effect of Front-Edge Radius

The drag coefficient of both numerical and experimental for varying front-edge radius at a Reynolds number of 8,000 are shown in Figure 5.1. From the figure, it can be seen that there is a reasonable difference between the simulated and experimental values, even when the experimental uncertainty is accounted for. The trend of the simulated variation in front-edges is that with an increasing radius the drag gradually decreases. Whereas the experimental results the drag gradually increases with increasing radius. At the largest radius, there is a sudden decrease in drag. This has a few possible causes. First, as mentioned before in Chapter 4 the force balance used to perform the measurements is designed for large models and thus larger forces. This means that at low velocities and smaller models the measurements are not that accurate, hence, the large measurement uncertainty that is shown in Figure 5.1. The second possibility that contributes to the difference in results is leading edge separation. van Tilborg [80] indicates in his work that with the simulation of a 1/8 scale GETS model no front-edge separation occurs, whereas with the wind tunnel test there is separation. Leading edge separation bubble is a contributor to the drag. The separation bubble is more probable to exist at low Reynolds numbers, where there is a transition from laminar to turbulent boundary layer, than with high Reynolds numbers where there is a fully turbulent boundary layer. From these type of differences, the drag coefficient of the simulated and wind tunnel tests can vary significantly. For the wind tunnel test performed for this study the used material for the model also plays a role. The front is made from plastic and the base from plywood. Because the interchangeable front-ends were create after the plywood base, the measurements of the plastic fronts are adjusted to have a near seamless transition without tripping the flow

into septation. The possible reason for the low drag prediction for simulated results are given in Section 5.4.

In addition, to the mentioned possible contributions to the drag difference between the numerical and experimental analysis, there is a source of drag generator that is not discussed yet. For the wind tunnel experiment, the model is attached to an aluminum rod, to transfer the forces that are exerted on the model to the force balance. Although, the rod if not large it has some effect on the drag contribution. With a length of 72 mm that is situated in the wind tunnel and a 10mm diameter, the additional drag count is in the range of 1 to 15. This is based on the applied force and velocities between 2 to 15m/s. Furthermore, there is also interference drag but that it hard to determine because the force on the rod is rather small. The contribution of the rod to the total drag may not be significant, however, it is mentioned for completeness.

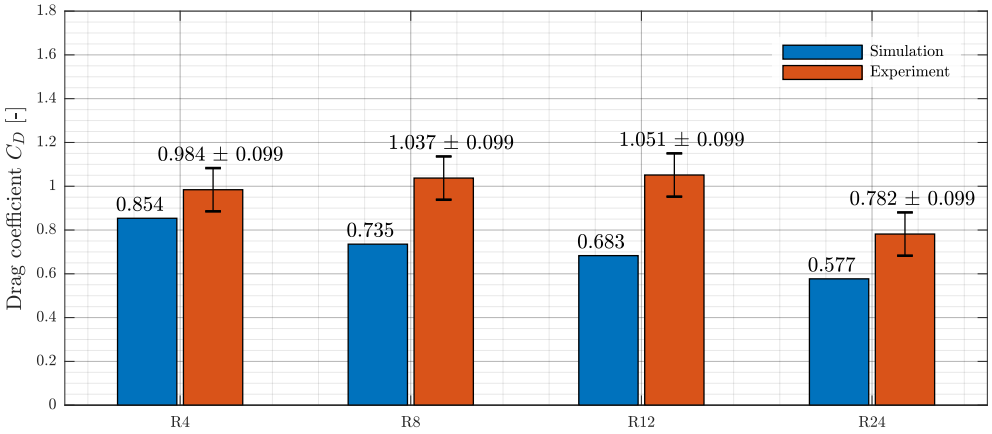

Figure 5.1: Experimental and numerical drag coefficient for various front-edge radii at Re=8,000 with N=46

To see how the drag of the numerical and experimental analysis relate with respect to the Reynolds number an overview is given in Figure 5.2. Here the experimental drag value is divided by the numerical obtained drag coefficient to create a ratio. As concluded from Figure 5.1, for low Reynolds numbers the difference between the numerical and experimental results are significant. However, this large difference is decreasing to a steady offset of 10% between the two for a Reynolds number of 48,000, this applies to all the variations of front-edge radii. For a radius of 4mm, it seems that there is a steady difference between the two, with values ranging from 10% to 14%. The steady deviation could be due to the sharp front-edge, where the flow separates immediately and generates the same flow phenomena at all Reynolds numbers. The remaining front-ends go from a difference as high as 55% to a steady 10% offset.

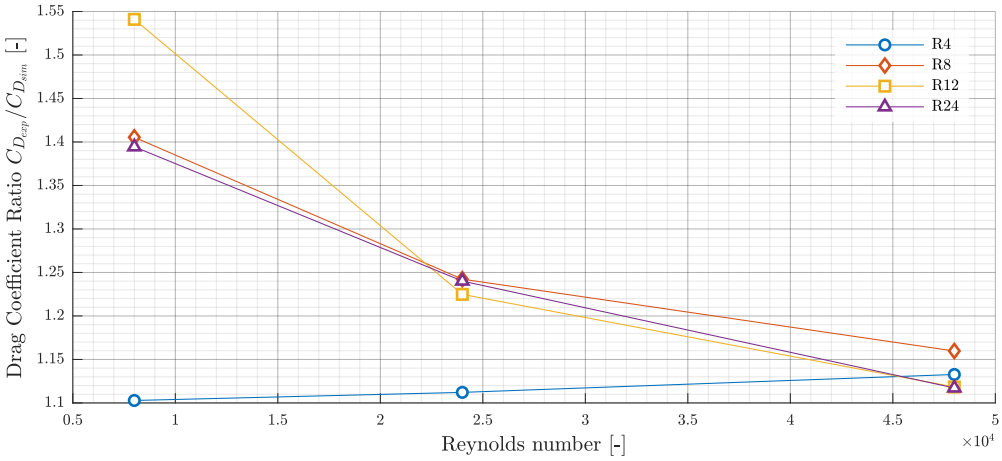

Figure 5.2: Ratio between the experimental and numerical drag coefficient for various front-edge radii at Re=8,000, 24,000 and 48,000, with N=46

This confirms the observation that is made in Chapter 4. That for low Reynolds number, or low velocities, there is a large amount of scattering in the obtained measurements. With the increase of Reynolds number, the measurements give a more constant value. This is mainly due to the force balance used for the test. The balance is designed for a larger model and higher velocities and with this test, it is at the lower limit of its initial design. This makes the balance less sensitive at the tested velocities and gives more scatter in the results.

In Figure 5.3, the simulated and the experimental obtained drag at a Reynolds number of 24,000 is shown. From this figure it can be seen that with increasing velocity and therefore increasing the force on the balance the same trend is observed as in Figure 5.2. With increasing front-edge radius the drag is reduced. This was already the case with the simulated results as shown in Figure 5.1, however, the fluctuations in experimental results did not follow the drag reduction with increasing radii. The comparison of simulated and experimental drag for a Reynolds number of 48,000 is illustrated by Figure A.1 can be seen in Appendix A.

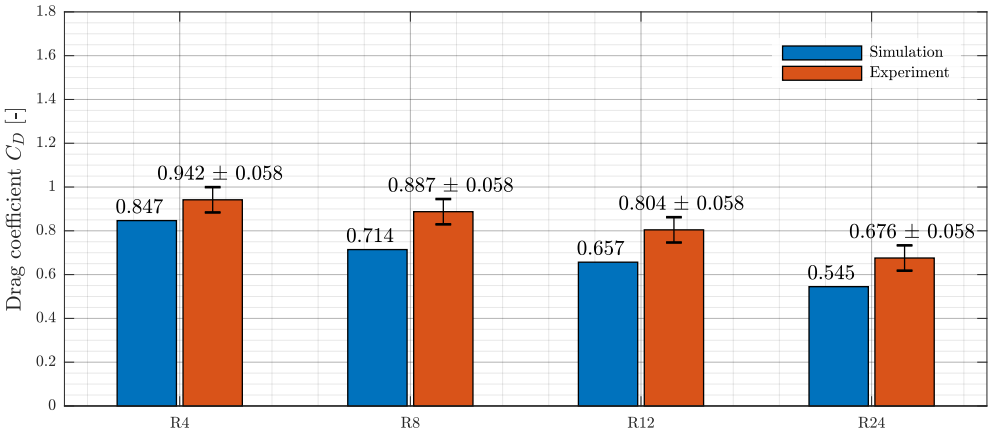

Figure 5.3: Experimental and numerical drag coefficient for various front-edge radii at Re=24,000 with N=46

5.1.2. Effect of Rear-End Shaping

The trend that is observed for the front radius variation in the previous section also applies for the comparison with the addition of tails, in Figure 5.4. This is valid if the comparison is made at a Reynolds number of 8,000. The drag of the numerical simulation is underestimated compared to the wind tunnel test. However, the numerical results follow the same trends as the experimental one. R4t18 , where the small t stands for the shorter tail and capitol T for the long tail, has the worst performance if it comes to drag reduction. The configuration with the largest front radius of 24mm and a tail with a slant angle of 12° gives the best results. The difference between the simulation and experiment is only 61 drag counts, which is only 12%. This value is the closest that both analysis methods achieve. This can be due to the large radius at the front, where the separation at the front-end is more gradual or very small. Also, the addition of a tail, that has a high drag efficiency, stabilizes the flow significantly and fluctuations in drag force are more within smaller margins. The configurations R8T18 and R12T6 perform similarity with the numerical simulation but vary more wind tunnel tests. The R8T18 configuration slightly under-performs compared to the R12T6 which complies with was is seen in Figure 5.4. In Appendix A the comparison between numerical and experimental results are shown for Re=24,000 & 48,000, in Figures A.3 and A.4.

In Figure 5.5 the drag reduction ratio is given for various Reynolds numbers. The drag of the base model is subtracted from the drag of the model with the same front-edge radius but with an attached tail. This is performed for both numerical and experimental results, where a ratio can be determined. From this ratio, a better insight is given in how the drag differences of both analyses method relate to each other. The drag difference ratio is a better comparison than the absolute values as shown in Figure 5.4. Herewith, the relative difference is given and the performance of the numerical simulation can be better put into perspective when it comes to validation.

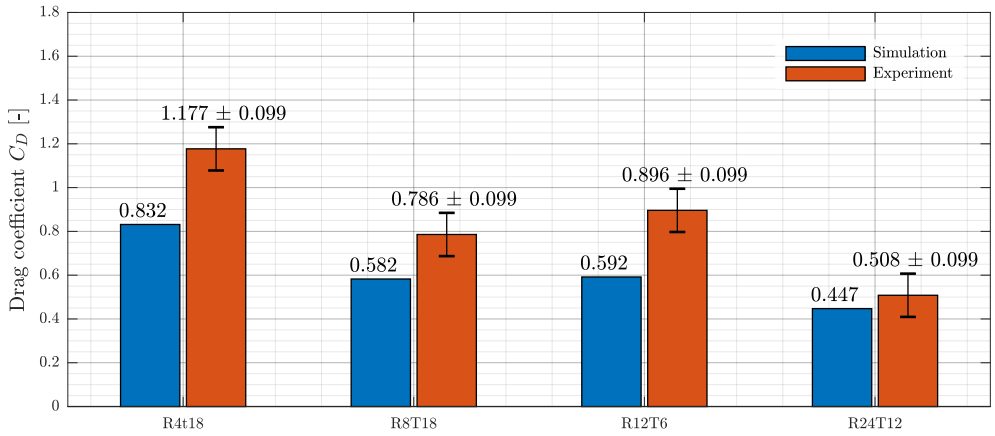

Figure 5.4: Experimental and numerical drag coefficient for various front-edge radii and tails at Re=8,000 with N=46

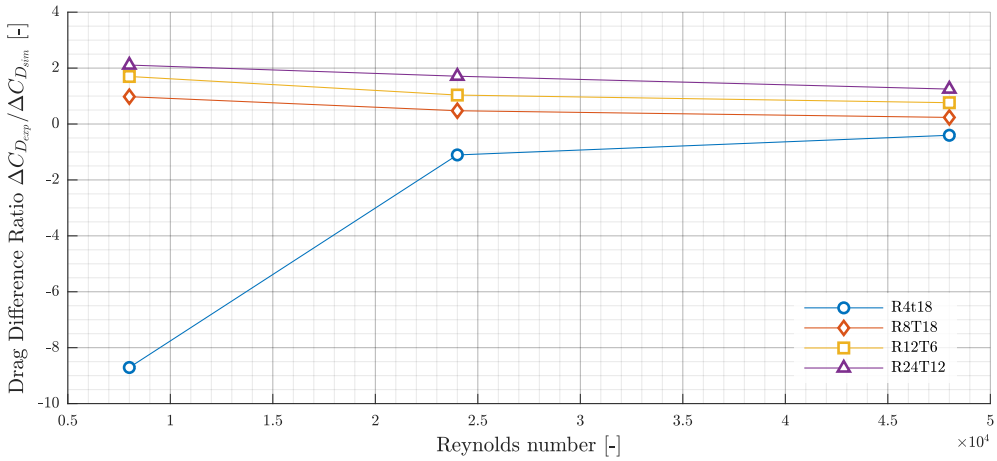

Figure 5.5: Ratio between the experimental and numerical drag coefficient difference for various front-edge and rear-end configurations at Re=8,000, 24,000 and 48,000, with N=46

As mentioned before in Section 3.3.5, the tail with an angle of 18° is where separation is expected. In Figure 5.6, where the drag of the experiment and numerical simulation form a ratio, closer to 1 means similar results. I can be seen that with increasing Reynolds number the configuration R4t18, R12T6 and R24T12, are converging to a somewhat steady value. The configuration with the steepest tail, R8T18, diverges from the others. This means that the experimental value shows separation over the tail and with the numerical simulation this is not the case. However, the poor performance of the 18° tail is visible when the pressure distribution over the rear-end of the model is considered. Further on in this chapter, in Figure 5.15, the pressure influence will be discussed. However, the remarkably improved performance of the R8T18 configuration in the simulation are not fully understood and no conclusive explanation can be given for this behavior.

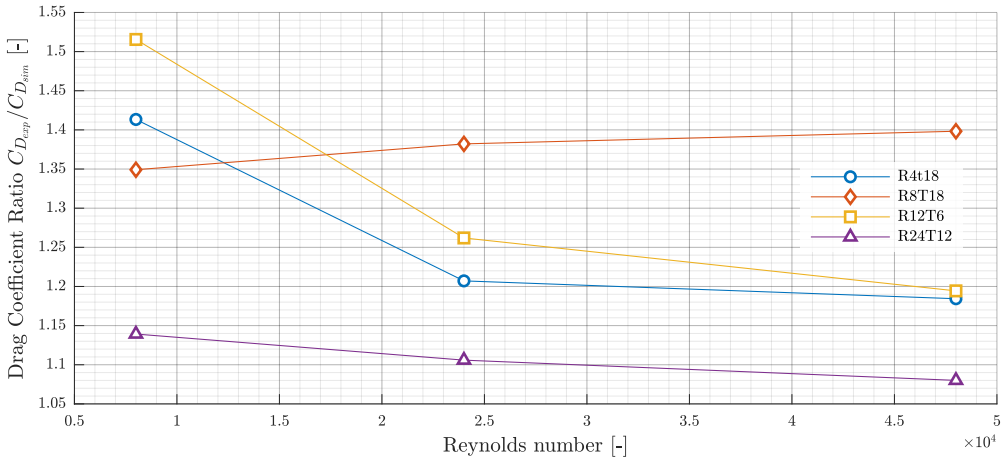

Figure 5.6: Ratio between the experimental and numerical drag coefficient for various boat tails at Re=8,000, 24,000 and 48,000, with N=46

In addition to various configurations with changing front-edge radii and tail slant angles, there have also been simulations performed with constant radius and three different tail angles. In Figure 5.7 the drag coefficient of an R8 front with an additional tail slanted at angles of 6°, 12° and 18° is shown. The drag difference of Figure 5.7 with the base model R8 can be seen in Figure A.6. The results are compared at a Reynolds number of 24,000. The general trend for the simulated results is, that with an increasing slant angle the drag decreased. With the wind tunnel results, there is only one difference and that is that with the largest slant angle, of 18°. The drag increases to a value that is higher than with the other two angles. The possible reason for this is, that with the wind tunnel test the tail is attached with tape on the rear of the model. As mentioned in Section 4.1.5, the tails needed to be soldered due to there small size. Therefore, the alignment of the tail is not completely flush with the base of the model which can cause early separation and increase in pressure drag. This also applies to the other tails, however, a slant angle of 18° has already a tendency to create separated flow, as can be seen in Section 5.2. The inaccuracy in the model build trips the flow to separate earlier, hence, increasing drag.

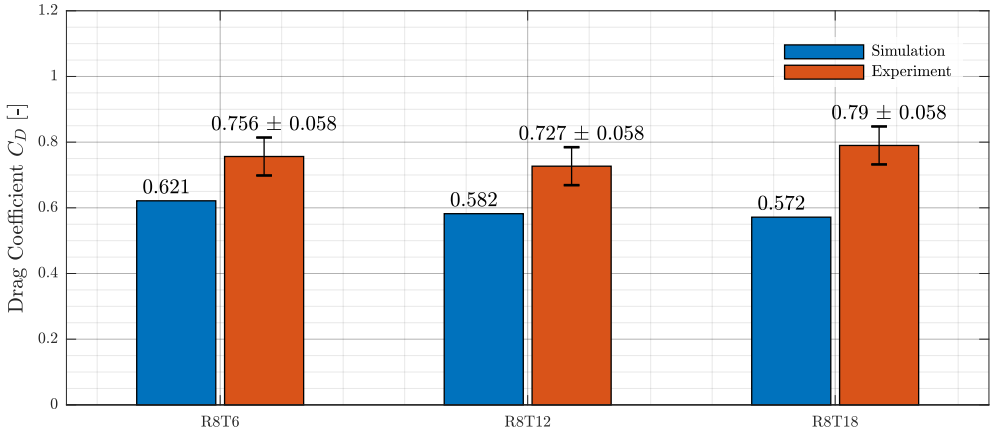

Figure 5.7: Experimental and numerical drag coefficient for a R8 with various tails at Re=24,000 and with N=46

Comparing the drag found by both numerical and experimental analysis with previous studies one thing that comes predominantly forward. That is the magnitude of the drag coefficient. The drag coefficient of the current study is double and in some cases threefold. In other studies, the Reynolds number used is multiple magnitudes higher compared to the current investigation. The limitation of the Reynolds number is due to the used open source CFD solver, *OpenLB*. Nevertheless, the influence of Reynolds number on the drag

is very prominent as Anderson [2] explains in his book. Drag is composed of two parts: pressure drag and skin friction drag. For bluff bodies large contribution to the drag is due to pressure, that is a consequence of massive regions of separation. These massive regions of separative flows become smaller with increasing Reynolds number. Partly because boundary layers at high Reynolds number are often more turbulent, which are known to "stick" longer to the surface. With the additional fact that high Reynolds number flows have a lower friction coefficient, so the relative contribution to the total drag is much lower than with low Reynolds number flows. Moreover, skin friction drag is relatively high at low Reynolds numbers, ergo the drag coefficient is higher. Wood [86] investigated the source of the pressure and friction drag contribution, for various Reynolds number, by vehicle-like bluff bodies and explains how to reduce them.

5.2. Flow Characteristics

In this section, the simulated flow characteristics of the simulation are compared to literature. With the wind tunnel tests only force measurements are performed, hence no knowledge of the flow field is known. This makes it hard to compare and validate the results. On top of that, the GETS model was designed by van Raemdonck and van Tooren [79] for a Ph.D. research, which restricts the number of scientific papers about this specific model available. However, since that time there have been Master students that have used the model to conduct numerical and experimental research [20, 32, 80, 84]. Either to be used in a platoon configuration to investigate which front-edge radius and rear-end tails perform the best, or how both ends of the model can be adjusted to have a more aerodynamic efficient design. These studies all start from the Ph.D. research conducted by van Raemdonck [78]. Nevertheless, the shape of the GETS model is a bluff vehicle body where a lot of research is performed giving enough available literature for validation. An additional note, the simulations are at conditions with relatively low Reynolds number, compared to other studies. At these low Reynolds number other force in the boundary layer play a larger role than at much higher Reynolds numbers.

5.2.1. Effect of Front-Edge Radius

Figure 5.8 shows the velocity in the x-direction, with additional streamlines to illustrate the behavior of the flow over the leading edge of the body. The first thing that is noticed is that with increasing the radius the magnitude of recirculation flow becomes significantly less. In close connection to the magnitude of the velocity, in the negative x-direction, is the size of the separation bubble. Due to the sharpness of the small front-edge radius adverse pressure gradient cause the flow to separate much sooner. With the reattachment point located much further downstream generated a larger bubble over the front-end. With a larger radius, the change in curvature is more gradual so the pressure gradient is more favorable in preventing separation and reducing the bubble.

A note has to be made regarding the geometry that is used in the simulation. The automated mesh generation used with *OpenLB*, plus the relatively large voxel size, creates a geometry that has a staircase shape of the curved edges. Although an appropriate boundary condition is used, Bouzidi, that interpolates between the voxels create as smooth as possible curve. There are more advanced boundary conditions with higher order schemes, however, these are not yet available in *OpenLB*. This does not change the fact that it has an influence on the flow behavior over the front-end of the model. One has to be careful in how the results are interpreted, because these could, to some extent, be different compared to the physical behavior.

Keeping the influence of geometry within the simulation in mind a general statement can be given on change in front-edge radius. This implies that with an increasing radius the bubble over the top is reduced and with this the drag contribution from the front decreases. There is a limit to how large the radius can be. Cooper [11] performed some research on how the front-edge radius has an effect on the drag. The intention of the survey was to demonstrate how low Reynolds number wind tunnel test data can be used to select the best possible radius for a full-scale vehicle. He found that for yaw angle of 0° and a square-shaped bluff vehicle a radius that is half the hight of the vehicle. That means that the front-end will be a complete round shape. For moderate Reynolds numbers, in the order of 10^5, this applies but for higher Reynolds numbers the radius can be reduced and still have a large drag reduction. This has to do with the turbulent nature of the flow at higher Reynolds numbers.

In addition, Veldhuis and Henneman [81] performed an experimental and numerical study on the leading edge separation of blunt bodies. The goal of the study was to find the separation point of a rounded front edge bluff bodies with relatively simple means. Using RANS and wind tunnel test the following finding were presented. Due to a lack of decent turbulence models the length of the separation bubble is underpredicted. Furthermore, the drag of various front-edge radii are investigated and compared with Cooper [11]. There is a

decent agreement with the work of Cooper [11] but only in the low turbulence cases. From the wind tunnel experiment it is shown that the reattachment length of the separation bubble is reducing with increasing radius, which is also the case what is observed with the current study,see Figure 5.8. The determined reattachment length by Veldhuis and Henneman [81] was in the sub critical Reynold range, this makes it the observation in the current study more reliable.

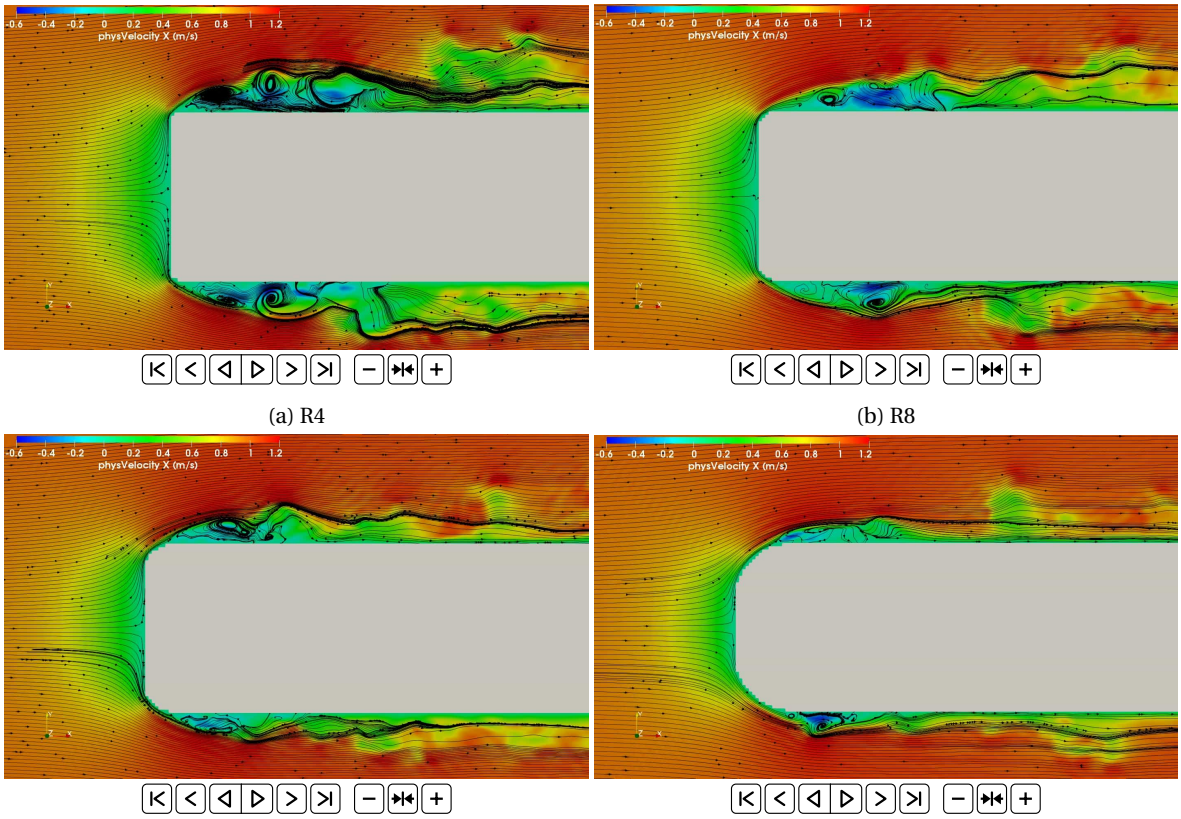

(a) R4 (b) R8

(c) R12 (d) R24

Figure 5.8: Animated numerical contour plot of the x velocity with streamlines for front-edges R4, 8, 12 and 24 at Re=24,000

5.2.2. Effect of Rear-End Shaping

If we compare Figure 5.9 with each other. One being a simulated result with *OpenLB* and the other a PIV measurement performed by van Raemdonck [78]. There is some resemblance of flow characteristic with the two, although the Reynolds numbers are far apart. In Figure 5.9b an GETS model at a scale of 1/15 is used with an front-edge radius of 36mm. For the 1/50 model that is used for this study it would mean that the radius must be 10.8mm, unfortunately, this not the case so the closest configuration is used. The time-average wake structure of a GETS model with a front-edge radius of 12mm is shown in Figure 5.9a. The time-average is obtained by taking every simulated value at each time-step adding them tougher and dividing it by the total amount of time step. Both are elevated from the ground so that the ground proximity has less influence on the flow behavior. Both figures show a large vortex structure on the lower side of the model and a small vortex at the top. The saddle point in Figure 5.9a is located at a point where most of the streamlines merge end of the wake, which is not very exactly at the same point as with the PIV measurements. Although, the large Reynolds number difference, $Re_{exp} = 8.3x10^5$ and $Re_{sim} = 2.4x10^4$ which are determined by the square root of the frontal surface, the flow characteristics are very similar. However, as mentioned before these results have to be viewed with a critical attitude due to the large Reynolds number difference and the accompanying flow phenomena that play a role in these different regimes.

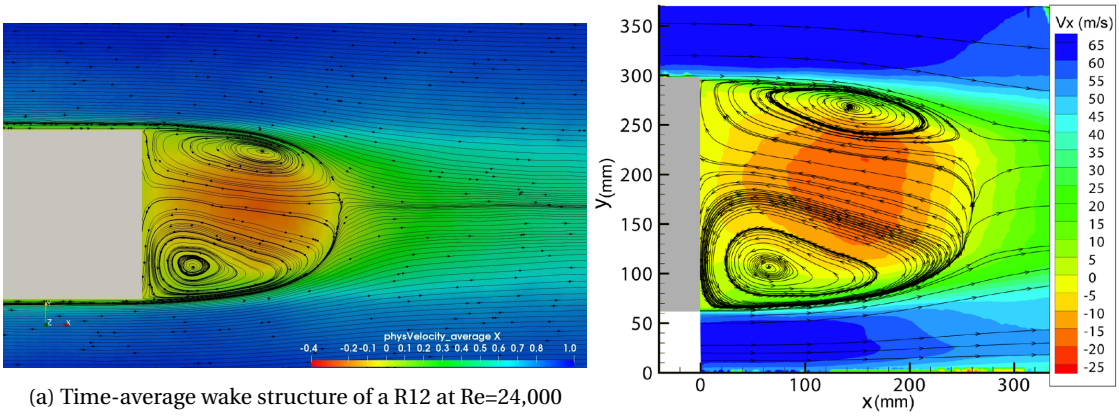

(a) Time-average wake structure of a R12 at Re=24,000

(b) Experimental wake structure obtained with PIV measurements [78]

Figure 5.9: Time-average wake structure comparison of *OpenLB* numerical simulation with experimental measurements of van Raemdonck [78]

It has been considered that boat tails and base cavities (boat tails at 0°), are the most effective and practical devices for drag reduction. Balkanyi et al. [3], Verzicco et al. [82], Yi [89], among others, have done research to find the optimal device. The core principals of these devices are to push the wake as far downstream as possible and reduce the size of the wake. Delaying separation over the tail and guiding the flow more inward, the wake size is reduced and thereby the recirculation area. These phenomena can be seen in Figure 5.11, where tails with a slant angle of 6°, 12°, 18° at a length of 30mm and one tail with a length of 10mm at an angle of 18°.

First the regimes that are suggested by Yi [89] are discusses with the help of Figure 5.10. A better understanding is gained to explain the flow characteristic that can be observed in Figure 5.11. The first region that is mention is with a slant angle varying from $0° < \alpha \leq 15°$. Here the flow separation is delayed till it reaches the trailing edge. this gives a drag reduction accordingly to the figure. Nearing a slant angle of 15°, the flow starts to separate on the junction of the boat tail and the base. This is all due to strong near-wall momentum increase which has a tremendous drag reducing effect, as illustrated in Figure 5.10. The second regime is at a tipping point, ranging from $16° \leq \alpha \leq 19°$. In addition to the starting separation of the flow over the tail, vortices have formed that roll over the tail reducing the effectiveness of the tail. The third and last regime where $\alpha \geq 20°$. Is where the flow is fully separated and the effect of the tail is completely diminished, the drag is even larger or equal to no tail at all. The numerical simulations and wind tunnel experiments all address these regimes of flow over the boat tail. To see if the flow characteristic match with that described above a brief discussion is given, even if the front-edge radii are different an useful observation can be made:

- **R12T6:** The tail with a slant angle of 6° is actually doing what it is designed for. The wake is pushing more downstream and the wake is narrowed down. Due to the relatively small deflection angle, the effect it has is also small. The tail of 6° falls in the first regime., where the separation of the flow is delayed to the trailing edge of the tail. With this tail, there are actually four vortices in the wake, two inside the tail cavity and two outside. The two vortices in the cavity are rather small compared to the vortices trailing the tail. This type of flow behavior is also caught by [80] in his numerical study of additional boat tails for a GETS model.
- **R24T12:** At a slant angle of 12° the drag is almost reduced to its minimum, according to the plot in Figure 5.10. This is certainly the case, numerical and experimental analysis shows that with either a 12° or 15° slant angle the highest drag reduction effectiveness is reached. The starting separation over the tail that is described by Yi [89] is not prominently visible in Figure 5.11b. Sporadically, there is flow separation on the lower side of the tail. For the large part of the time, there is only one large vortex contained within the tail. However, when separation occurs, on the bottom, a second small vortex develops. There is an interaction going on between the small vortex and the separated flow. On the top side, there is no vortex generated so the flow stays attached there. At this angle, the strength of the recirculating velocity over the entire rear part of the model is reduced considerably.
- **R8T18:** A tail of 18° fits in flow characteristics of the second regime with slant angle between $16° \leq \alpha \leq$

19°. Looking at Figure 5.11c there is definitely some separation visible over the tail. Additionally, the wake is narrowed down but it is not constant. Due to the bubble bursting over the tail in momentarily causes the wake to expand and increase the drag. This is also what Yi [89] describes what happens in that regime. The tail also decreases the magnitude of the recirculation velocity in the wake. The migration vortex into the cavity of the tail reduced the influence it has on the guided flow over the tail. This in return is beneficial for the aerodynamic efficiency of the design.

- **R4t18:** A tail that is not considered in the analysis of Yi [89] but also not mentioned in Choi et al. [10], is the shorter tail as in Figure 5.11d. The short tail partly reduces the size of the wake. Due to the length and angle of the tail, the separation bubble does not have the surface to reattach and have a drag reducing effect. There are some conflicting results in relation to numerical and experimental findings. From the simulation, the drag is lower compared to the wind tunnel test. Considering Figure 5.11d, the tail has certainly an effect, even if it is not that evident. The wake is narrower compared to the wake without a tail. This mismatch between the two is hard to pinpoint too one or two sources, there is a causality that needs more investigation.

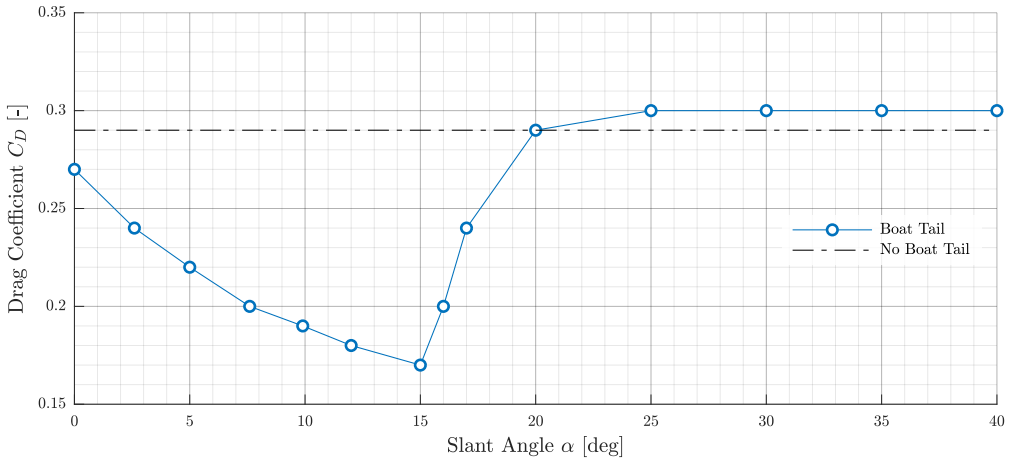

Figure 5.10: Variation of drag coefficient with slant angle for a GTS model Yi [89]

The dimensions of the tail are not exactly the same as used in the wind tunnel test. The thickness of the tail in the simulation is primarily determined by the voxels size. Due to the staircase approximation of curves and sloped boundaries by *OpenLB*, the thickness of the tail needed to be adjusted to have a closed tail. In the simulation, the tail is 8mm thick whereas with the wind tunnel test model the tail is 1.5mm. This obviously has an influence on the flow behavior around and inside the tail. Considering these discrepancies in geometry, which is a result of the limitation of the used package and have to be accepted as they are. The results still come close to representing the correct flow phenomenon. It can be stated that *OpenLB* gives an accurate representation of the flow field, to a certain extent.

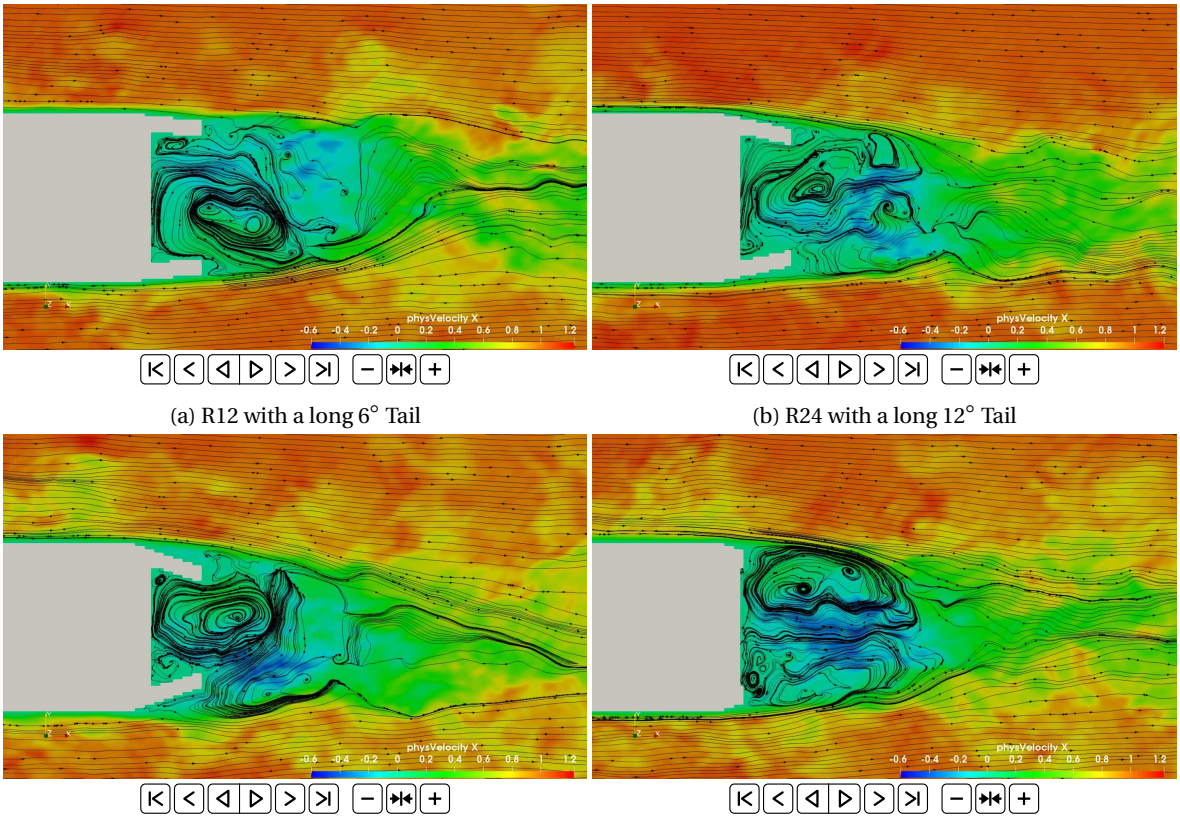

(a) R12 with a long 6° Tail

(b) R24 with a long 12° Tail

(c) R8 with a long 18° Tail

(d) R4 with a short 18° Tail

Figure 5.11: Animated numerical contour plot of the x velocity with streamlines for R8 with tails angled at 6°, 12° and 18° at Re=24,000

5.2.3. Model Position

As seen in fig. 3.9, the position of the model does not influence the drag. van Raemdonck [78] investigated the effect of ride height on the drag and concluded that with increasing ride height the drag coefficient is increased. However, this mainly due to the longer struts that are needed to secure the model to the floor of the wind tunnel. In addition, the drag increase with ride height is not significant, in de order of 10 to 15 drag counts. From which we can conclude that with increasing height the drag is somewhat constant.

This may be true for the drag but the flow characteristics do change with ride height, as can be seen in Figure 5.12. The wake structure shift from a large vortex on the top to a large vortex on the bottom part of the model with increasing height. The migration of the largest vortex is also observed in Section 3.3.3. Because of the model size and the subsequently used wind tunnel, it was not possible to place the model that close to the ground. The buildup of the boundary layer has an influence on the experimental results. In hindsight, due to the fact that no flow field measurements were performed with the wind tunnel test, there is also no need to place the model that close to the ground. The only downside is that no real comparison can be made, only a general one.

From this general comparison the effect of the model position w.r.t. the ground is very well visible in the *OpenLB* simulations illustrated in Figure 5.13a & Figure 5.13b. The simulation is of an R12 at a Re=24,000 with N=46. Converting the scale used in this investigation to that used by van Raemdonck [78], it can be said that Figure 5.13a, is placed around h=0.33. The position of the R12 model as shown in Figure 5.13b is higher than the maximum measured by van Raemdonck [78]. These two simulated ride heights show practically the same flow characteristic behavior as with the PIV measurements. Although, there is a large difference in Reynolds number the same flow patterns emerge.

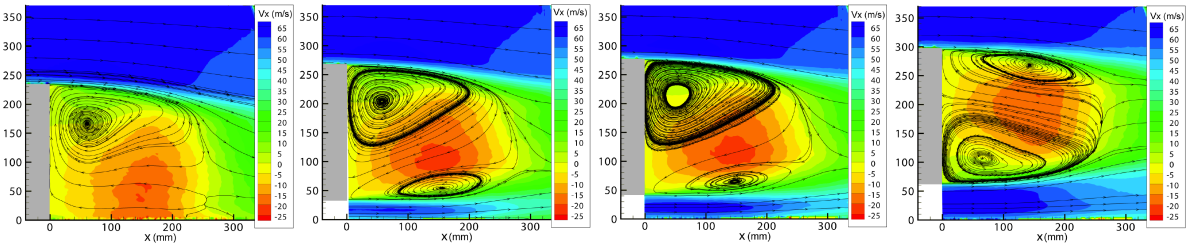

(a) h= 0mm (b) h= 33mm (c) h= 42mm (d) h= 62mm

Figure 5.12: Experimental wake structure visualization of GETS model at various ride heights,van Raemdonck [78]

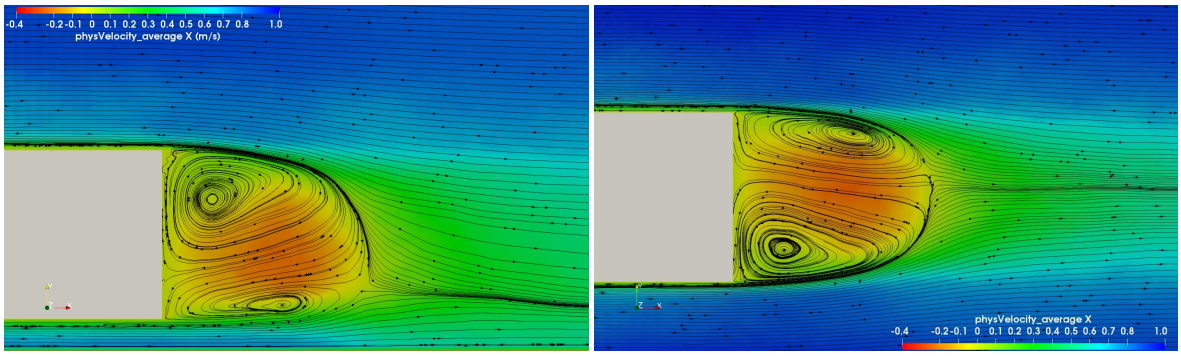

(a) Wake structure of a R12 in ground proximity at Re=24,00 (b) Wake structure of a R12 in higher position at Re=24,000

Figure 5.13: Time-average wake structure comparison of *OpenLB* numerical simulation at different heights with Re=24,000 and N=46

5.3. Pressure Coefficient

From *OpenLB* the total pressure of the fluid domain can be retrieved. Due to a lack of a wall model function, the pressure on the body itself cannot be determined. Also close to the body the pressure does not represent physical values. Therefore, it is chosen to measure the velocity at a fixed distance from the base of the model. The applies to the model without a tail and with a tail. The pressure measured is at a fixed length behind the tail and not inside the tail cavity. The combination of the tail thickness and the closeness to the wall it was a logical choice to measure the pressure behind the tail. Partly by the lacking of wall model function and the measurement location, it is not possible to have a quantitative and qualitative comparison. Besides the mentioned reason above, in addition to that is, that the Reynolds numbers are fairly apart so that on his own gives different results.

For the base GETS model there is a pressure coefficient distribution on the rear part of the model. The experiment performed by van Raemdonck and van Tooren [79] is often subjected to validation cases for numerical simulation, as can be seen in Figure 5.14a. As illustrated in the figure the RANS simulation shows an over and underprediction of the pressure coefficient, whereas the LBM simulation gives a reasonably good result. The LBM simulation uses a VLES turbulence model so a somewhat more accurate turbulence model is used. As mentioned before no true comparison can be made with the pressure distribution plotted in Figure 5.14a. The mean pressure presented in Figure 5.14b gives a better comparison. With a large Reynolds number difference, the mean pressure coefficient is still close to that of numerical and experimental results. A true comparison can be if the pressure is measured at the same location and Reynolds number. Nevertheless, this gives a good indication that the pressure prediction of *OpenLB* is close to that of literature.

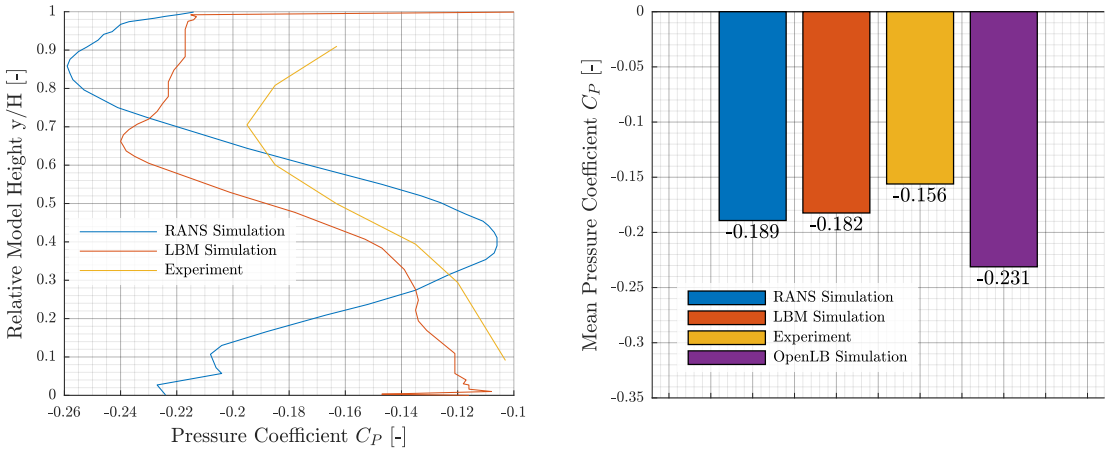

(a) Pressure coefficient rear z=0.5W

(b) Mean Pressure Coefficients

Figure 5.14: Numerical and experimental base pressure distribution from literature. RANS simulations by Gheyssens [20], LBM simulation by van Tilborg [80], experiment by van Raemdonck and van Tooren [79] and *OpenLB* for R12 at a Re=24,000 with N=46

In Figure 5.15 the mean pressure aft of a R24 model with various boat tails is given over simulation time. The influence on the additional tail is very prominent visible in the figure. The base model R24 without a tail has lowest pressure coefficient, that oscillates around $C_P = -0.14$, and the R24T12 model has the highest pressure coefficient, which fluctuates around $C_P = -0.08$. This shows that the tail with an angle of 12° has the largest drag relieve at the rear of the model. However, this does not show in the drag predicted by *OpenLB*, which is peculiar and the reason for this deviant behavior is unknown. Figure 5.15 also shows the period patterns over the aft of the model. The oscillating behavior has to do with the pumping effect, where the vortices encapsulated by the shear layer are shed generating a pressure fluctuation.

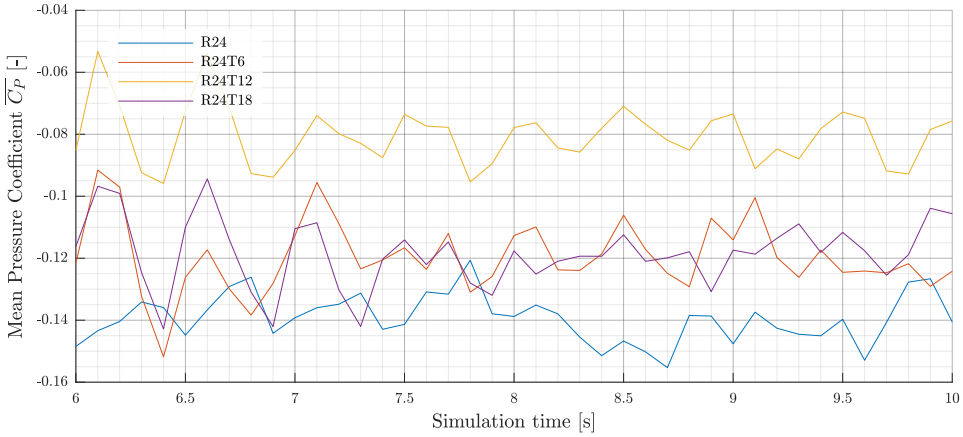

Figure 5.15: Mean pressure over the aft part of various R24 configurations plotted against simulation time at a Re=24,000 and with N=46

An attempt is made to obtain the Strouhal number, Equation (5.1), from the pressure oscillations shown in Figure 5.15. The results are given in Table 5.1 and shows that the model with the lowest drag, R24T12, has also the lowest Strouhal number. R24T18 has the highest Strouhal number which means that the frequency of vortex shedding is increased. The increase in Strouhal number suggests that due to instabilities more vortices are shed. However, the increase in Strouhal number for the configurations with boat tails angled at 6° & 18° is not in line with literature, because with the addition of a tail the fluctuations should reduce and therefore decrease the non-dimensional frequency [37].

$$St = \frac{fL}{U_\infty} \tag{5.1}$$

Table 5.1: Strouhal number of R24 with various tails at a Re=24,000 with N=46

	R24	R24T6	R24T12	R24T18
St	0.0833	0.0857	0.0706	0.0947

Duell and George [14] conducted an LES study of a three-dimensional bus-shape model at ground proximity and obtained a Strouhal number of 0.069. Khalighi et al. [37] also conducted a study that is comparable with Duell and George [14] and obtained Strouhal numbers of 0.07 and 0.073 from an unsteady base pressure analysis. The Strouhal numbers determined in this study are close to that found in literature, however, there has been noted that the accuracy of the obtained values is arguable. The frequency of measured pressure is too low to capture the full unsteady flow behavior. Although the accuracy of the Strouhal number is not what is expected, a basis for future investigation is created.

5.4. Influence of Chosen Simulation Parameters on the Results

Choosing the parameters for a numerical simulation always need to be supported by an explanation of why and with which purpose are these parameters selected. The methods used and the values chosen have to match with the problem otherwise the results could not represent the physical behavior. In this section, the effects of the chosen parameters are elaborated in more detail and a practical view is given.

5.4.1. Mesh Resolution

The relation between the relaxation time and the mesh resolution is clearly stated in Section 3.2.4, and the effect it has on the accuracy and stability of an LBM simulation. The choice of mesh resolution is a more practical one. Selecting a smaller voxel size means that the number of cells will increase quadratically. The computational resources that it requires will also increase. Due to the limitation of time and resources, a trade-off is made to select a mesh resolution that acknowledges these limitations and still have an as accuracy simulation as possible. Moreover, increasing the resolution of the mesh a few problems arise. There are a few options in how *OpenLB* converts an STL file into a mesh. The first option is fast and less accurate and the other option is slow but more stable. From experience the latter option is more stable, however, even using that option the simulated mesh generated some error due to a numerical mismatch of array quantities. This was also one of the limitations for having a finer grid.

5.4.2. Relaxation Time

The effect of choosing the right relaxation time parameter has significant influence in how the simulation performs. With the right relaxation time, the stability of the simulation is determined. For the mesh sensitivity study, the relaxation time is kept constant and the voxel size is adjusted to see the effect it has on the stability and accuracy of the simulation, this is often called diffusive scaling. An evident statement is that the relaxation time has to be above 0.5, however, with high Reynolds number this threshold of 0.5 comes close be being chosen. Working with these high Reynold number the kinematic viscosity tends to be very low, so selecting a relaxation time that considers the lattice spacing, Reynolds number and the stability is a tough one. Therefore, a more iterative process needs to be taken in order to select the right relaxation time that is both stable and safeguards the accuracy of the simulation. There is an infinite possible combination of values that can be chosen to still have a physical solution.

5.4.3. LES: Model and Smagorinsky constant

Some practical aspects of LES need to be discussed. Practical applications and results evaluation of large eddy simulation hold some difficulties. As Pope [64] brings forward in his book that a sound LES simulation should resolve a minimum of 80% of the turbulent kinetic energy. Numerical simulations are often used as prediction tools in engineering applications. To have a good understanding of how an design impacts the flow and other important quantities. For this type of design assessment, numerical methods give a good insight at relatively low cost. For LES simulations the flow field and the total amount of kinetic energy are unknown, which complected the assessment of uncertainty. Determining the uncertainties with RANS is easier because grid studies are performed to evaluate the quality of various meshes. Theoretically, within LES there is no grid independence since the grid size correlates to the filter width. A grid independence with LES is practically a DNS simulation where are the scales are resolved and the philosophy of LES is lost with grid independence

[8].

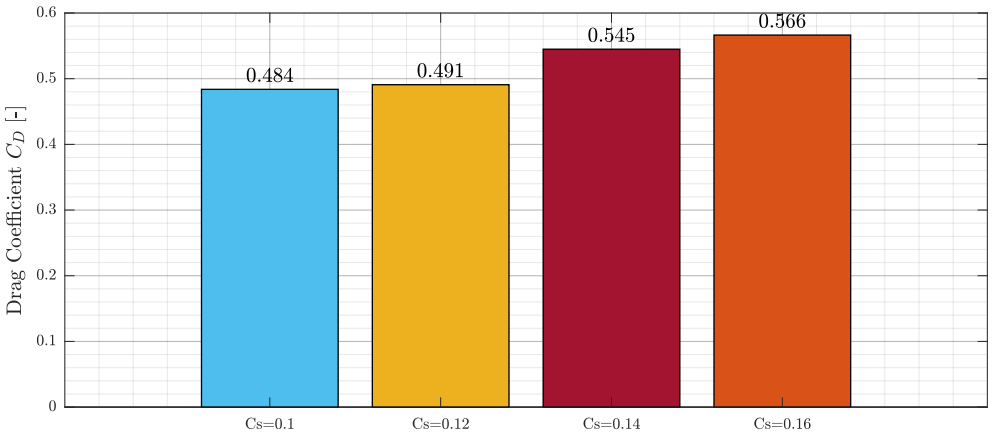

Figure 5.16: Drag of R24 for various Smagorinsky constants at Re=24,000 with N=46

The choice for an LES model also determines the accuracy and correctness of the simulated flow. Although the grid size has an influence on the obtained results there is one more parameter that can be fine-tuned to achieve satisfactory results, that is the Smagorinsky constant. The Smagorinsky constant has an effect on the amount of dissipation within the LES model that is used in this study, which is the consistent Smagorinsky method. The amount of dissipation partly determines the magnitude of the drag coefficient, so to investigate the effect of the Smagorinsky constant, simulation with varying constants are executed. For a R24 model the following Smagorinsky constants, C_s = 0.1, 0.12, 0.14 and 0.16, are simulated. The effect of this can be seen in Figure 5.16. From the figure, it can be concluded that the Smagorinsky certainly has an effect on not only the drag coefficient but probably also on the flow behavior. With increasing the constant the drag coefficient is increased as well. The drag coefficient for the wind tunnel test for an R24 configuration at a Re=24,000 is C_D = 0.676. There is still a difference of more than 100 drag counts so with this it can be concluded that the Smagorinsky constant has some effect on bringing the numerical and experimental results closer together but actually a different LES model needs to be considered.

6

Conclusions and Recommendations

The aim of this study was to investigate the performance of the open source Lattice Boltzmann Method package, *OpenLB*. The simulation is performed on a 3D bluff vehicles at moderate Reynolds numbers. The aim is simultaneously the main question that was formulated at the start of the research. As a guideline throughout the investigation sub-question are constructed:

1. *Are the flow characteristics of a typical bluff vehicle captured by OpenLB simulations?*
2. *How well does OpenLB predict the drag coefficient when compared to wind tunnel test of a bluff vehicle with various front- and rear-end configurations?*
3. *Does the pressure coefficient simulated by OpenLB match with patterns found in literature, for the front- and rear-end of the bluff body?*

First conclusions that can be drawn from this investigation are stated in Section 6.1. These will answer the main and sub-questions of this research project. In conclusion to the whole, recommendations are made for further research topics and improvements to the current study in Section 6.2

6.1. Conclusion

In a general sense one conclusion can be drawn from this investigation. *OpenLB* is not yet at a level that it is useful for general engineering applications. To begin with, even the simulations at moderate Reynolds numbers required a relatively fine grid over the whole domain. The absence of local grid refinement means that the whole domain is meshed with a uniform grid. Secondly, using LES for turbulence modeling is a smart due to the time-depended nature of LBM. This combines the two strengths of both methods to exploit its advantages. However, LES has major drawbacks when it comes to computational resources it requires and the accompanying limitation on Reynolds number it imposes by the enforces small grid sizes, which is essential to capture relevant flow scales. These limits LBM-LES combination too only being cost-effective at low to moderate Reynolds numbers. The difficulty of this study, hence also with *OpenLB*, is that a few methods are combined which are researched intensively nowadays. To name a few, Lattice Boltzmann Method, Transient flows (which is inherently LBM but nevertheless) and Large Eddy Simulation. These are very difficult subject on there own, however, to combine them and making it useful in general engineering would be a great leap in Computer Fluid Dynamics. In conclusion, the potential of *OpenLB* to grow and become a very useful CFD tool that provides an alternative to not only commercial LBM packages but also for conventional CFD packages, both commercial and open source, is very much present. To achieve this a few improvements and additions to the tool are required. The recommendations are further discussed in Section 6.2.

To support this conclusion and answer the sub-questions a further elaboration of the research is given in the remaining part of this section.

Flow Characteristics
A wide range of configuration is simulated to show the effect of the body modification, but also to investigate the correctness of the flow field. In general, *OpenLB* simulates the flow characteristics fairly accurately. The trend visible for the front-edge modification matches that of literature. With increasing radius, the separation bubble over the front is reduced and therefore the drag contribution from the frontal surface is smaller. The Reynolds number has definitely influence on the flow characteristics. With increase Reynolds number the separation bubble at the front is also reduced and can even fully disappear. Addition of the boat tail not only has an influence on the rear part of the flow field but also at the front. The attachment of the elongated boat tail ensured that the flow over the tail accelerated. This energized the boundary layer over the entire model and thereby affecting the bubble at the front by reducing it. From experiments and numerical simulations, it can be concluded that the tail with an angle of 12° or 15° has the best drag reduction capabilities. This is supported by literature, by comparing the flow characteristics for certain regimes with varying boat tail slant angle. Furthermore, the position of the model, at ground proximity or at higher positions, also resembles the flow field patterns seen in the study of van Raemdonck [78]. All in all, it can be concluded that the flow patterns simulated by *OpenLB* are accurate to a certain extent. The Reynolds number and the mesh resolution play a vital role in the accuracy of the flow field behavior. To truly compare the results higher Reynolds numbers need to be simulated.

Drag Prediction
Comparing the drag for only the base models with changing front-edge radii it can be stated that there is a relatively large difference between numerical simulation and experiment results, especially for low Reynolds numbers. A difference between the experiment and numerical simulation is varying from 10-50% for Reynolds number of 8,000 to a deviation of 16% for Reynolds number of 48,000. The discrepancy in the numerical and experimental results at low Reynolds number is a consequence of the sensitivity of the force balance used to measure the force in the wind tunnel. The force balance is normally used for much larger models and higher velocities so the forces applied on the balance are higher. At higher velocities, there are a lot fewer fluctuations in measured force to a threshold is passed where the force on the balance is registered more accurately. This affects both the configurations with and without a tail. The drag coefficient of the model configuration with the additional tail follows the same general trend for both numerical simulation and experiments, with increasing slant angle the drag is decreased. There is only a difference in results when a slant angle of 18° is considered. In the simulation no major regions of separation over the tail at a slant angle of 18° are observed, so the drag is the lowest at this angle. Whereas in the experimental results the drag at this slant angle has a much higher drag contribution. Furthermore, the regimes described by Yi [89], show that there must be some increase in drag coefficient. The simulations at such a low Reynolds number may have an effect on the flow behavior and on the drag coefficient. The discrepancy in results can also be the cause of the chosen LES model. Considering an LES model that performs better in determining the shear stresses on a body would help to have a more accurate representation of the forces.

Pressure Patterns
The pressure patterns do not completely match what is found in literature. The pressure coefficient value and pattern at the front of the model fairly represent the expected patterns. The stagnation pressure at the front is simulated very nicely and change with the increase of the front-edge radius. Increasing the radius means that there is less frontal surface so the stagnation pressure gradually reduces as it moves from the middle to the edge. With the smallest radius, the transition from a stagnation pressure of $C_p = 1$ to negative pressure is more abrupt due to the sudden separation that occurs at small radii. The pressure coefficient values at the rear of the model, with or without a tail, are somewhat on the more negative side. For a base model the pressure coefficient is around $C_p = -0.24$ and with an additional tail, it can increase to $C_p = -0.15$. This pressure difference for a model with or without a tail has major influence on the drag coefficient. An addition of a tail almost reduced the drag to half of its original value. The reason for the difference of pressure coefficient is the location of where the pressure is measured. Due to an absence of a wall model within *OpenLB* there is no possibility to obtain the pressure at the surface of the model, as is done in literature. Furthermore, very close to the model the values are not representing physical values, so the pressure is obtained at a constant distance from the front and rear of the model. This difference in measured position obviously influences the pressure pattern and the magnitude of the pressure coefficient. However, trends are observed when there is a change in model configuration, this gives generally a good insight into how the tail influences the pressure aft of the model.

6.2. Recommendations

A first attempt is made to investigate the performance of *OpenLB* for bluff vehicles at moderate Reynolds numbers. This does not mean the research into this topic is complete. Based on the insight gained from the performed work a few recommendations can be made for future studies:

- **Local Grid Refinement:** An important feature missing within the *OpenLB* framework is the option of local grid refinement. Now the whole fluid domain is represented by a uniform grid, this is not computationally efficient. Refining the grid at places of importance give not only a more accurate flow behavior but also reduced the computational cost.

- **Wall Function:** To further reduce the computational cost of a simulation an addition of a wall function can be a step in the right direction. A wall function analytically approximates the very thin region of the boundary layer, called the buffer layer, with a nonzero velocity at the wall. With this function, the comparison of pressure over the surface of the model can be done in a genuine fashion. The correlation between the simulations and the experimental results are better to detect

- **Higher Reynolds Numbers:** For this investigation moderate Reynolds numbers were considered due to the limitations of the *OpenLB* package. With the recommendations implemented above, higher Reynolds numbers can be investigated to have simulations that can be used to truly compare real-life applications. The Lattice Boltzmann Method implemented in *OpenLB* could have a proper validation study with existing numerical and experimental results of the GETS model. Simulating higher Reynolds numbers could have contributed more to increase the aerodynamic efficiency of a heavy-duty vehicle.

- **Hybrid Turbulence Modeling:** Using LES as a turbulence model limits the Reynolds numbers that be simulated. LES still requires intensive research to reach a level of maturity that it is used for mainstream engineering and industrial computation. If an intermediate step can be taken, with the transient nature of LBM in mind, this would make OpenLB a more used open source software tool. A hybrid turbulence model that is also used by EXA's Powerflow, with VLES and a κ-ϵ Renormalization group (RNG) to model the boundary layer, can be an intermediate step to eventually full LES simulation. However, the choice for a certain turbulence model is also made out of a particular belief in a method so it is up to the developers of *OpenLB* to choose what they think is the best path to take.

- **Better Wind Tunnel Test:** Due to the setup of the whole wind tunnel experiment the results at low Reynolds number had a wide spread of results. This had to do with the position of the force balance and that the force balance was not very sensitive for small models and low inlet velocities. Therefore, wind tunnel test needs to be performed with a larger model that produces results that are in a smaller band of uncertainty than with the current investigation. If the results are more reliable, from the wind tunnel, then a better validation case could be made for the numerical simulation. To have a full investigation, PIV measurements to should be performed to have a complete image of flow behavior and real comparison can be made. In addition, the model should be more accurate when it comes to the alignment of the tail with the base of the model, to prevent prematurely tripping the flow too early separation.

- **Compare with Commercial Codes:** A validation and performance of *OpenLB* is not only depended on the wind tunnel tests. An interesting study would be if a one on one comparison can be made with commercial codes. Either a comparison with a commercial Finite Volume Method (Fluent) or a Lattice Boltzmann Method (PowerFlow) or both would give an indication where *OpenLB* stands in the fields of, computational efficiency, prediction of flow behavior and force prediction.

Bibliography

[1] H. J. Alons. *OJF External Balance*. National Aerospace Laboratory (NLR), November 2008.

[2] John Jr. D. Anderson. *Fundamentals of Aerodynamics*. McGraw-Hill Education, 2010. ISBN 978-0-07-339810-5.

[3] Szabolcs R. Balkanyi, Luis P. Bernal, and Bahram Khalighi. Analysis of the near wake of bluff bodies in ground proximity. In *Fluids Engineering*. ASME, 2002. doi: 10.1115/imece2002-32347.

[4] Ilhan Bayraktar, Drew Landman, and Oktay Baysal. Experimental and computational investigation of ahmed body for ground vehicle aerodynamics. In *SAE Technical Paper Series*. SAE International, nov 2001. doi: 10.4271/2001-01-2742.

[5] P. L. Bhatnagar, E. P. Gross, and M. Krook. A model for collision processes in gases. i. small amplitude processes in charged and neutral one-component systems. *Physical Review*, 94(3):511–525, may 1954. doi: 10.1103/physrev.94.511.

[6] M'hamed Bouzidi, Mouaouia Firdaouss, and Pierre Lallemand. Momentum transfer of a boltzmann-lattice fluid with boundaries. *Physics of Fluids*, 13(11):3452–3459, nov 2001. doi: 10.1063/1.1399290.

[7] M. Breuer, J. Bernsdorf, T. Zeiser, and F. Durst. Accurate computations of the laminar flow past a square cylinder based on two different methods: lattice-boltzmann and finite-volume. *International Journal of Heat and Fluid Flow*, 21(2):186–196, apr 2000. doi: 10.1016/s0142-727x(99)00081-8.

[8] I. B. Celik, Z. N. Cehreli, and I. Yavuz. Index of resolution quality for large eddy simulations. *Journal of Fluids Engineering*, 127(5):949, 2005. doi: 10.1115/1.1990201.

[9] Sydney Chapman and T. G. Cowling. *The Mathematical Theory of Non-uniform Gases: An Account of the Kinetic Theory of Viscosity, Thermal Conduction and Diffusion in Gases (Cambridge Mathematical Library)*. Cambridge University Press, 1970. ISBN 0521075777.

[10] Haecheon Choi, Jungil Lee, and Hyungmin Park. Aerodynamics of heavy vehicles. *Annual Review of Fluid Mechanics*, 46(1):441–468, jan 2014. doi: 10.1146/annurev-fluid-011212-140616.

[11] Kevin R. Cooper. The effect of front-edge rounding and rear-edge shaping on the aerodynamic drag of bluff vehicles in ground proximity. In *SAE Technical Paper Series*. SAE International, feb 1985. doi: 10.4271/850288.

[12] K.R. Cooper. Bluff-body aerodynamics as applied to vehicles. *Journal of Wind Engineering and Industrial Aerodynamics*, 49(1-3):1–21, dec 1993. doi: 10.1016/0167-6105(93)90003-7.

[13] L. G. Dodge and J. A. Schwalb. Fuel spray evolution: Comparison of experiment and CFD simulation of nonevaporating spray. *Journal of Engineering for Gas Turbines and Power*, 111(1):15, 1989. doi: 10.1115/1.3240218.

[14] Edward G. Duell and A. R. George. Experimental study of a ground vehicle body unsteady near wake. In *SAE Technical Paper Series*. SAE International, mar 1999. doi: 10.4271/1999-01-0812.

[15] European Commission. *EU Transport In Figures – Statistical Pocketbook*. Publications Office of the European Union, 2017. ISBN 978-92-79-62311-0. doi: 10.2832/147440.

[16] European Parliament. Directive (eu) 2015/719 of the european parliament and of the council. *Official Journal of the European Union*, 115, April 2015. URL `http://eur-lex.europa.eu/legal-content/EN/TXT/PDF/?uri=CELEX:32015L0719&from=EN`.

[17] *Powerflow user's guide*. Exa Corporation, 2017b edition, 2017.

[18] Y. T. Feng, K. Han, and D. R. J. Owen. Coupled lattice boltzmann method and discrete element modelling of particle transport in turbulent fluid flows: Computational issues. *International Journal for Numerical Methods in Engineering*, 72(9):1111–1134, 2007. doi: 10.1002/nme.2114.

[19] E. Garnier, N. Adams, and P. Sagaut. *Large Eddy Simulation for Compressible Flows*. Springer Netherlands, 2009. doi: 10.1007/978-90-481-2819-8.

[20] Thomas Gheyssens. Aerodynamic analysis of a platoon ofblu bodies subjected to cross wind: A numerical investigation on the eect of drag reduction devices. Master's thesis, TU Delft, 2016.

[21] Zhaoli Guo, Chuguang Zheng, and Baochang Shi. An extrapolation method for boundary conditions in lattice boltzmann method. *Physics of Fluids*, 14(6):2007–2010, jun 2002. doi: 10.1063/1.1471914.

[22] Hans Götz. On the aerodynamic development of the experimental vehicles c 111 i–IV (mercedes). *Journal of Wind Engineering and Industrial Aerodynamics*, 9(1-2):3–21, nov 1981. doi: 10.1016/0167-6105(81)90074-X.

[23] S. Haeri and J.S. Shrimpton. On the application of immersed boundary, fictitious domain and body-conformal mesh methods to many particle multiphase flows. *International Journal of Multiphase Flow*, 40:38–55, apr 2012. doi: 10.1016/j.ijmultiphaseflow.2011.12.002.

[24] J. Halliday, C. Teixeira, and C. Alexander. Simulation of engine internal flows using digital physics. *Oil & Gas Science and Technology*, 54(2):187–191, mar 1999. doi: 10.2516/ogst:1999013.

[25] M. Hammache and F. Browand. On the aerodynamics of tractor-trailers. In *The Aerodynamics of Heavy Vehicles: Trucks, Buses, and Trains*, page 185–205. Springer Berlin Heidelberg, 2002. doi: 10.1007/978-3-540-44419-0_20.

[26] J. Hardy, Y. Pomeau, and O. de Pazzis. Time evolution of a two-dimensional model system. i. invariant states and time correlation functions. *Journal of Mathematical Physics*, 14(12):1746–1759, 1973. doi: 10.1063/1.1666248.

[27] Harwell and Didcot. Good practice guide: Truck aerodynamic styling. Technical Report 308, Department for Transport, June 2001. URL `http://www.transport-research.info/sites/default/files/project/documents/20060210_121817_04842_GPG308.pdf`.

[28] Xiaoyi He and Gary Doolen. Lattice boltzmann method on curvilinear coordinates system: Flow around a circular cylinder. *Journal of Computational Physics*, 134(2):306–315, jul 1997. doi: 10.1006/jcph.1997.5709.

[29] Xiaoyi He and Gary D. Doolen. Lattice boltzmann method on a curvilinear coordinate system: Vortex shedding behind a circular cylinder. *Physical Review E*, 56(1):434–440, jul 1997. doi: 10.1103/PhysRevE.56.434.

[30] Xiaoyi He, Li-Shi Luo, and Micah Dembo. Some progress in lattice boltzmann method. part i. nonuniform mesh grids. *Journal of Computational Physics*, 129(2):357–363, dec 1996. doi: 10.1006/jcph.1996.0255.

[31] Sighard F. Hoerner. *Fluid-Dynamic Drag: Practical information on Aerodynamic Drag and Hydrodynamic Resistance*. Sighard F. Hoerner, 1965.

[32] M.L. Hoogendoorn. Base drag reduction ofheavy duty vehicles bycombining a tail andguide vanes: A numerical and experimental analysis. Master's thesis, Delft Univercity of Technology, 2018.

[33] Takaji Inamuro. Lattice boltzmann methods for moving boundary flows. *Fluid Dynamics Research*, 44(2):024001, feb 2012. doi: 10.1088/0169-5983/44/2/024001.

[34] Takaji Inamuro, Masato Yoshino, and Fumimaru Ogino. A non-slip boundary condition for lattice boltzmann simulations. *Physics of Fluids*, 7(12):2928–2930, dec 1995. doi: 10.1063/1.868766.

[35] Shin K. Kang and Yassin A. Hassan. The effect of lattice models within the lattice boltzmann method in the simulation of wall-bounded turbulent flows. *Journal of Computational Physics*, 232(1):100–117, jan 2013. doi: 10.1016/j.jcp.2012.07.023.

[36] P.-H. Kao and R.-J. Yang. An investigation into curved and moving boundary treatments in the lattice boltzmann method. *Journal of Computational Physics*, 227(11):5671–5690, may 2008. doi: 10.1016/j.jcp.2008.02.002.

[37] Bahram Khalighi, S. Zhang, C. Koromilas, S. R. Balkanyi, Luis P. Bernal, G. Iaccarino, and P. Moin. Experimental and computational study of unsteady wake flow behind a bluff body with a drag reduction device. In *SAE Technical Paper Series*. SAE International, mar 2001. doi: 10.4271/2001-01-1042.

[38] Yusuke Koda and Fue-Sang Lien. The lattice boltzmann method implemented on the gpu to simulate the turbulent flow over a square cylinder confined in a channel. *Flow, Turbulence and Combustion*, 94 (3):495–512, dec 2014. doi: 10.1007/s10494-014-9584-y.

[39] Manfred Krafczyk, Jonas Tölke, and Li-Shi Luo. Large-eddy simulations with a multiple-relaxation-time lbe model. *International Journal of Modern Physics B*, 17(01n02):33–39, jan 2003. doi: 10.1142/S0217979203017059.

[40] Siniša Krajnović and Lars Davidson. Numerical study of the flow around a bus-shaped body. *Journal of Fluids Engineering*, 125(3):500–509, 2003. doi: 10.1115/1.1567305.

[41] Mathias J. Krause. *OpenLB User Guide Associated to Release 1.1 of the Code*, April 2017. URL `http://www.openlb.net/`.

[42] Timm Krüger, Halim Kusumaatmaja, Alexandr Kuzmin, Orest Shardt, Goncalo Silva, and Erlend Magnus Viggen. *The Lattice Boltzmann Method*. Springer International Publishing, 2017. doi: 10.1007/978-3-319-44649-3.

[43] Anthony J. C. Ladd. Numerical simulations of particulate suspensions via a discretized boltzmann equation. part 1. theoretical foundation. *Journal of Fluid Mechanics*, 271:285, jul 1994. doi: 10.1017/s0022112094001771.

[44] L. D. Landau and E. M. Lifshitz. *Fluid Mechanics: Landau and Lifshitz: Course of Theoretical Physics, Volume 6*. Pergamon, 1987. ISBN 9781483161044.

[45] Jonas Lätt. *Hydrodynamic limit of lattice Boltzmann equations*. PhD thesis, Université de Genève, 2007.

[46] Jonas Latt. *Choice of units in lattice Boltzmann simulations*. Palabos, 2008. URL `http://wiki.palabos.org/_media/howtos:lbunits.pdf`.

[47] Jonas Latt and Bastien Chopard. Lattice boltzmann method with regularized pre-collision distribution functions. *Mathematics and Computers in Simulation*, 72(2-6):165–168, sep 2006. doi: 10.1016/j.matcom.2006.05.017.

[48] Jonas Latt, Bastien Chopard, Orestis Malaspinas, Michel Deville, and Andreas Michler. Straight velocity boundaries in the lattice boltzmann method. *Physical Review E*, 77(5), may 2008. doi: 10.1103/PhysRevE.77.056703.

[49] J. Leuschen and K.R. Cooper. *Summary of full-scale wind tunnel tests of aerodynamic dragreducingdevices for tractor-trailers*, pages 451–462. Springer, 2009.

[50] E. Lévêque, F. Toschi, L. Shao, and J.-P. Bertoglio. Shear-improved smagorinsky model for large-eddy simulation of wall-bounded turbulent flows. *Journal of Fluid Mechanics*, 570:491, jan 2007. doi: 10.1017/S0022112006003429.

[51] Orestis Malaspinas and Pierre Sagaut. Advanced large-eddy simulation for lattice boltzmann methods: The approximate deconvolution model. *Physics of Fluids*, 23(10):105103, oct 2011. doi: 10.1063/1.3650422.

[52] Orestis Malaspinas and Pierre Sagaut. Consistent subgrid scale modelling for lattice boltzmann methods. *Journal of Fluid Mechanics*, 700:514–542, apr 2012. doi: 10.1017/jfm.2012.155.

[53] Renwei Mei, Li-Shi Luo, and Wei Shyy. An accurate curved boundary treatment in the lattice boltzmann method. *Journal of Computational Physics*, 155(2):307–330, nov 1999. doi: 10.1006/jcph.1999.6334.

[54] Renwei Mei, Wei Shyy, Dazhi Yu, and Li-Shi Luo. Lattice boltzmann method for 3-d flows with curved boundary. *Journal of Computational Physics*, 161(2):680–699, jul 2000. doi: 10.1006/jcph.2000.6522.

[55] Rachel Muncrief and Ben Sharpe. Overview of the heavy-duty vehicle market and co2 emissions in the european union. Technical report, ICCT, 2015.

[56] NASA. Global temperature. Website, 2017. URL `https://climate.nasa.gov/interactives/climate-time-machine`.

[57] Patrick Nathen, Daniel Gaudlitz, Mathias Krause, and Jonas Kratzke. An extension of the lattice boltzmann method for simulating turbulent flows around rotating geometries of arbitrary shape. In *21st AIAA Computational Fluid Dynamics Conference*. American Institute of Aeronautics and Astronautics, jun 2013. doi: 10.2514/6.2013-2573.

[58] Patrick Nathen, Daniel Gaudlitz, Mathias J. Krause, and Nikolaus A. Adams. On the stability and accuracy of the bgk, mrt and rlb boltzmann schemes for the simulation of turbulent flows. *Communications in Computational Physics*, 23(3):846–876, March 2018. doi: 10.4208/cicp.OA-2016-0229.

[59] P.S. Newnham. *The influence of turbulence on the aerodynamic optimisation of bluff body road vehicles*. PhD thesis, Loughborough University, 2007. URL `https://dspace.lboro.ac.uk/2134/14381`.

[60] X.D. Niu, C. Shu, Y.T. Chew, and Y. Peng. A momentum exchange-based immersed boundary-lattice boltzmann method for simulating incompressible viscous flows. *Physics Letters A*, 354(3):173–182, may 2006. doi: 10.1016/j.physleta.2006.01.060.

[61] Wabco OptiFlow. Wabco optiflow tail., 2018. URL `http://www.wabco-auto.com/products/category-type/trailer-aerodynamics/optiflow-tail/`.

[62] Jason M. Ortega, Tim Dunn, Rose McCallen, and Kambiz Salari. Computational simulation of a heavy vehicle trailer wake. In *The Aerodynamics of Heavy Vehicles: Trucks, Buses, and Trains*, pages 219–233. Springer Berlin Heidelberg, 2004. doi: 10.1007/978-3-540-44419-0_22.

[63] R.K. Pachauri and L.A. Meyer. Climate change 2014: Synthesis report, 2015.

[64] Stephen B. Pope. *Turbulent Flows*. Cambridge University Press, 2000. ISBN 978-0-521-59886-6.

[65] W. Rodi, J. H. Ferziger, M. Breuer, and M. Pourquie'e. Status of large eddy simulation: Results of a workshop. *Journal of Fluids Engineering*, 119(2):248, 1997. doi: 10.1115/1.2819128.

[66] Pierre Sagaut. Toward advanced subgrid models for lattice-boltzmann-based large-eddy simulation: Theoretical formulations. *Computers & Mathematics with Applications*, 59(7):2194–2199, apr 2010. doi: 10.1016/j.camwa.2009.08.051.

[67] M. Schäfer, S. Turek, F. Durst, E. Krause, and R. Rannacher. Benchmark computations of laminar flow around a cylinder. In *Notes on Numerical Fluid Mechanics (NNFM)*, pages 547–566. Vieweg + Teubner Verlag, 1996. doi: 10.1007/978-3-322-89849-4_39.

[68] T. S. Shao, T. C. Chen, and R. M. Frank. Tables of zeros and gaussian weights of certain associated laguerre polynomials and the related generalized hermite polynomials. *Mathematics of Computation*, 18(88):598–598, 1964. doi: 10.1090/s0025-5718-1964-0166397-1.

[69] P. A. Skordos. Initial and boundary conditions for the lattice boltzmann method. *Physical Review E*, 48 (6):4823–4842, dec 1993. doi: 10.1103/physreve.48.4823.

[70] J. Smagorinsky. General circulation experiments with the primitive equations. *Monthly Weather Review*, 91(3):99–164, mar 1963. doi: 10.1175/1520-0493(1963)091<0099:GCEWTP>2.3.CO;2.

[71] S. Stolz and N. A. Adams. An approximate deconvolution procedure for large-eddy simulation. *Physics of Fluids*, 11(7):1699–1701, jul 1999. doi: 10.1063/1.869867.

[72] Sauro Succi. *The Lattice Boltzmann Equation for Fluid Dynamics and Beyond (Numerical Mathematics and Scientific Computation)*. Clarendon Press, 2001. ISBN 9780198503989.

[73] Sauro Succi. Lattice boltzmann 2038. *EPL (Europhysics Letters)*, 109(5):50001, mar 2015. doi: 10.1209/0295-5075/109/50001.

[74] K. Suga, Y. Kuwata, K. Takashima, and R. Chikasue. A d3q27 multiple-relaxation-time lattice boltzmann method for turbulent flows. *Computers & Mathematics with Applications*, 69(6):518–529, mar 2015. doi: 10.1016/j.camwa.2015.01.010.

[75] Michael C. Sukop and Daniel T. Thorne. *Lattice Boltzmann Modeling*. Springer Berlin Heidelberg, 2006. doi: 10.1007/978-3-540-27982-2.

[76] Christopher M. Teixeira. Incorporating turbulence models into the lattice-boltzmann method. *International Journal of Modern Physics C*, 09(08):1159–1175, dec 1998. doi: 10.1142/s0129183198001060.

[77] United Nations Framework Convention on Climate Change UNFCCC. Paris climate agreement. united nations treaty collection, 2015. URL `https://treaties.un.org/pages/ViewDetails.aspx?src=TREATY&mtdsg_no=XXVII-7-d&chapter=27&clang=_en`.

[78] G. M. R. van Raemdonck. *Design of low drag bluff road vehicles*. PhD thesis, Delft university of Technology, 2012.

[79] G.M.R. van Raemdonck and M.J.L. van Tooren. Time avaraged phenomenological investigation of a wake behind a bluff body. In *BBAA VI International Colloquium on: Bluff Bodies Aerodynamics & Applications*, pages 20–24, 2008.

[80] Frank van Tilborg. Flow analysis between two bluff bodies in a close distance platooning configuration: A numerical and experimental study. Master's thesis, TU Delft, 2018.

[81] L. L. M. Veldhuis and B. Henneman. Experimental and numerical study of leading edge separation on blunt bodies. *SAE Transactions*, 116:360–371, 2007. ISSN 0096736X.

[82] R. Verzicco, M. Fatica, G. Iaccarino, P. Moin, and B. Khalighi. Large eddy simulation of a road vehicle with drag-reduction devices. *AIAA Journal*, 40(12):2447–2455, dec 2002. doi: 10.2514/2.1613.

[83] Alexander Thomas White and Chuh Khiun Chong. Rotational invariance in the three-dimensional lattice boltzmann method is dependent on the choice of lattice. *Journal of Computational Physics*, 230(16):6367–6378, jul 2011. doi: 10.1016/j.jcp.2011.04.031.

[84] R. Wildvank. Aerodynamic effects offrontal elongation appliedto a bluff body: According to a cfd design study. Master's thesis, Delft Univercity of Technology, 2018.

[85] Richard Wood. A review of reynolds number effects on the aerodynamics of commercial ground vehicles. *SAE International Journal of Commercial Vehicles*, 5(2):628–639, sep 2012. doi: 10.4271/2012-01-2045.

[86] Richard M. Wood. Impact of advanced aerodynamic technology on transportation energy consumption. In *SAE Technical Paper Series*. SAE International, mar 2004. doi: 10.4271/2004-01-1306.

[87] Richard M. Wood. A discussion of heavy truck advanced aerodynamic trailer system. In *The international forum for road transport technology (IFRTT)*, 2006.

[88] World Resources Institute. Paris agreement tracker. Website, 2018. URL `http://cait.wri.org/indc/#/ratification`.

[89] W. Yi. *Drag reduction of a three-dimensional car model using passive control device*. PhD thesis, Seoul National University, 2007.

[90] Luoding Zhu, Guowei He, Shizhao Wang, Laura Miller, Xing Zhang, Qian You, and Shiaofen Fang. An immersed boundary method based on the lattice boltzmann approach in three dimensions, with application. *Computers & Mathematics with Applications*, 61(12):3506–3518, jun 2011. doi: 10.1016/j.camwa.2010.03.022.

[91] Qisu Zou and Xiaoyi He. On pressure and velocity boundary conditions for the lattice boltzmann BGK model. *Physics of Fluids*, 9(6):1591–1598, jun 1997. doi: 10.1063/1.869307.

A

Drag comparison

In this appendix the experimental and numerical simulated drag values are shown.The plots in this appendix are supplementary to the drag contribution and drag difference of various configuration mentioned in the main body.

Effect of Front Rounding

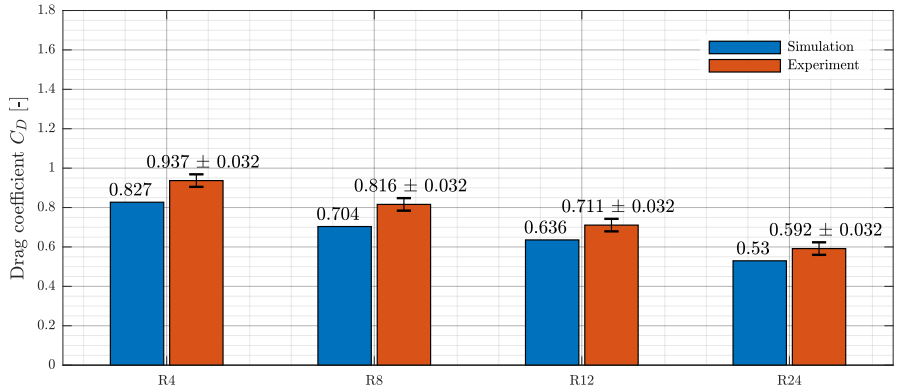

Figure A.1: Experimental and numerical drag coefficient for various front-edge radii at Re=48,000 with N=46

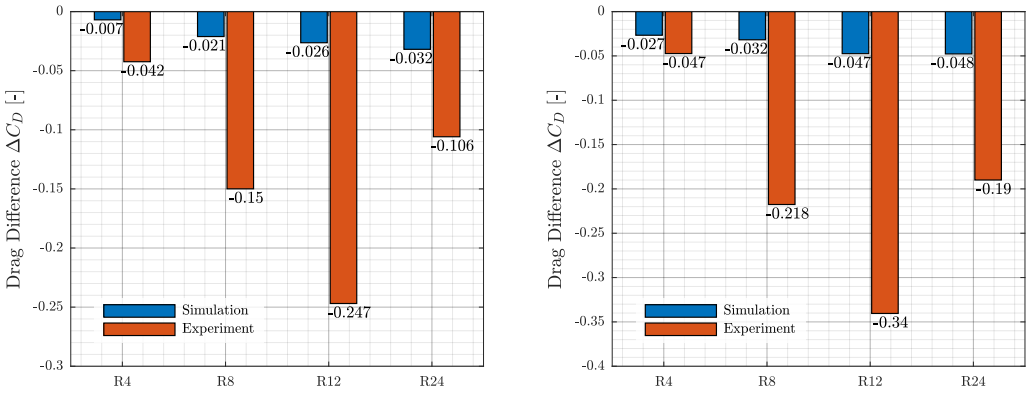

(a) Drag difference at Re=24000

(b) Drag difference at Re=48000

Figure A.2: Experimental and numerical drag coefficient difference of GETS model with various front-end radius at Re=24,000 & 48,000 w.r.t. to the reference value of Reynolds number of 8000

Effect of Tail

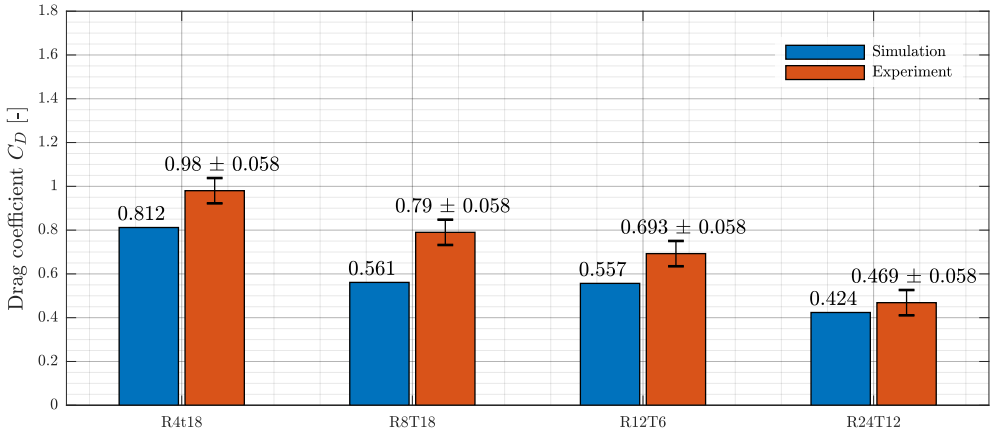

Figure A.3: Experimental and numerical drag coefficient for various front-edge radii and tails at Re=24,000 with N=46

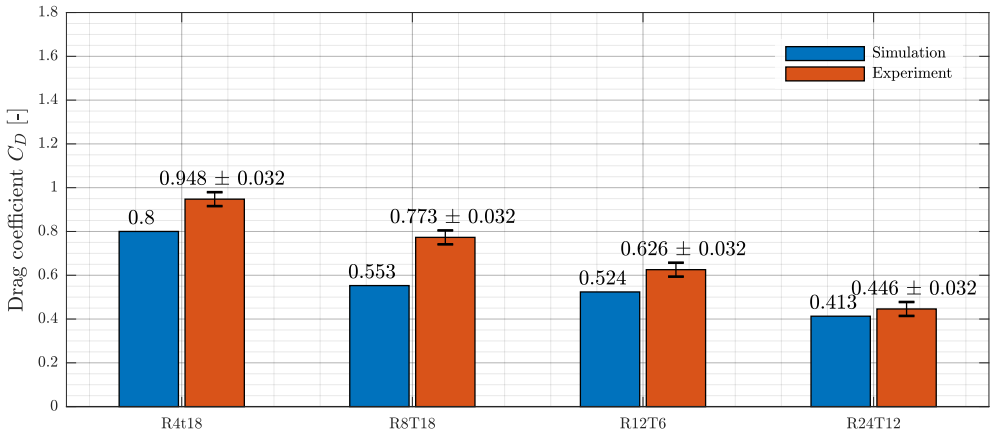

Figure A.4: Experimental and numerical drag coefficient for various front-edge radii and tails at Re=48,000 with N=46

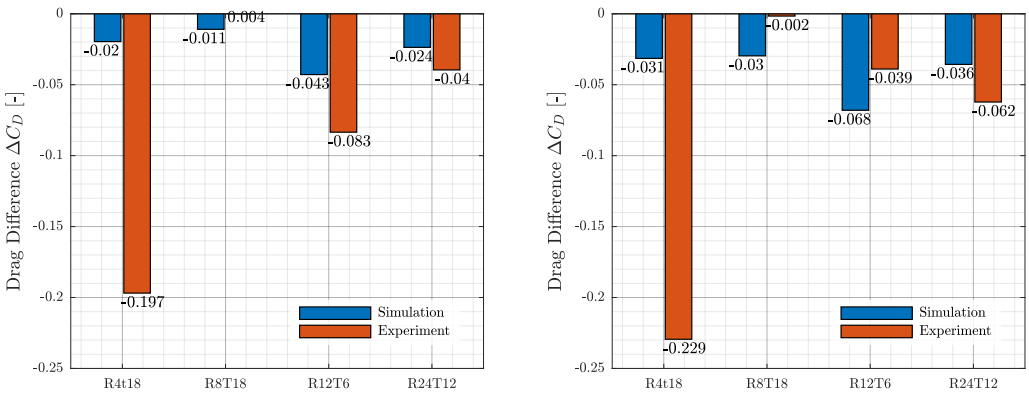

(a) Drag difference at Re=24,000

(b) Drag difference at Re=48,000

Figure A.5: Experimental and numerical drag coefficient difference of GETS model with various tails at Re=24,000 & 48,000 w.r.t. to the reference value of Reynolds number of 8,000

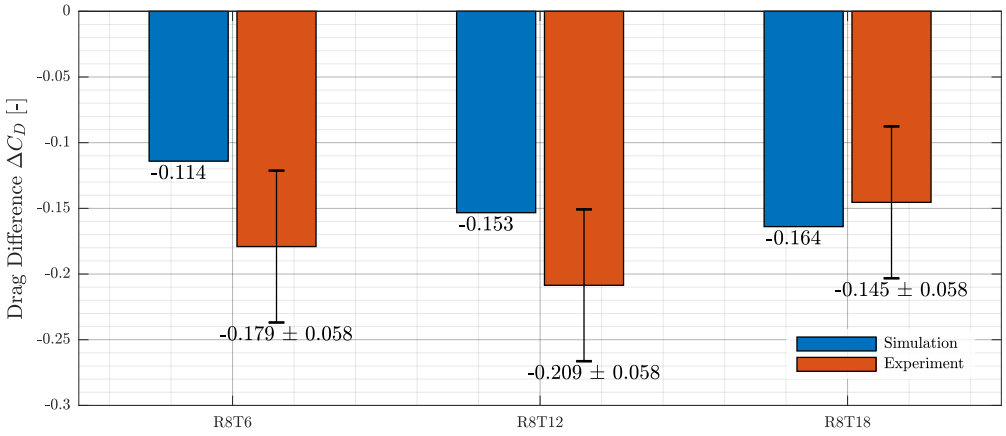

Figure A.6: Experimental and numerical drag coefficient difference of GETS model R8 with tails of 6°, 12° and 18° at Re=24,000 w.r.t. to the reference value of base model R8

B

Contour Plots

This appendix shows the contour plot of all the configurations at every Reynolds number that are simulated. The front and rear of the models are shown, accompanied with stream lines of the flow.

R4t18

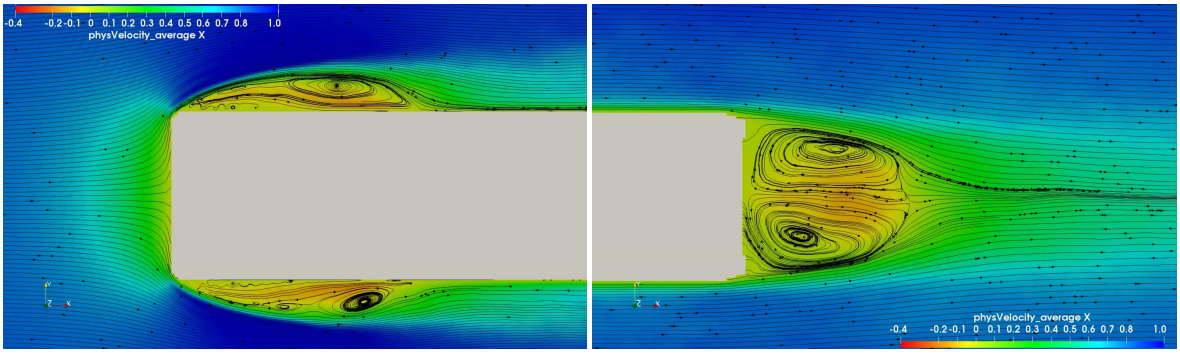

(a) Front-end of R4t18 model, Re=8,000 (b) Rear-end of R4t18 model, Re=8,000

Figure B.1: Time-average contour plot of x-velocity of R4t18 at a Re=8,000 with N=46

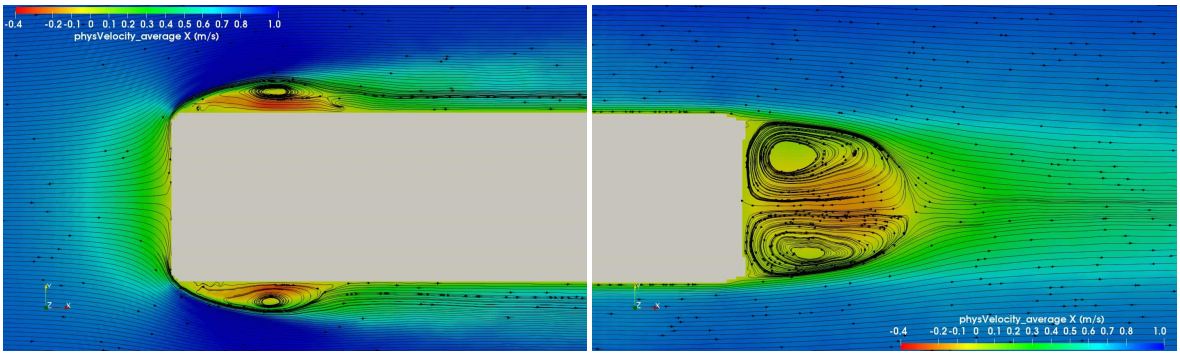

(a) Front-end of R4t18 model, Re=24,000 (b) Rear-end of R4t18 model, Re=24,000

Figure B.2: Time-average contour plot of x-velocity of R4t18 at a Re=24,000 with N=46

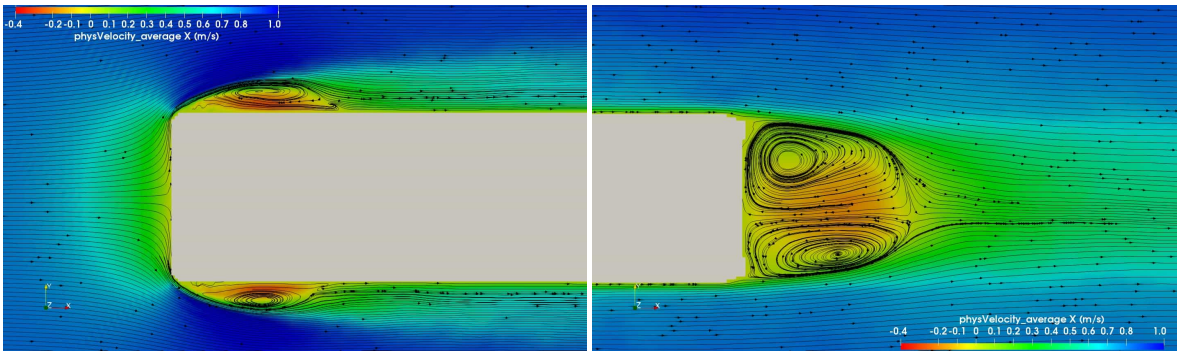

(a) Front-end of R4t18 model, Re=48,000 (b) Rear-end of R4t18 model, Re=48,000

Figure B.3: Time-average contour plot of x-velocity of R4t18 at a Re=48,000 with N=46

R8

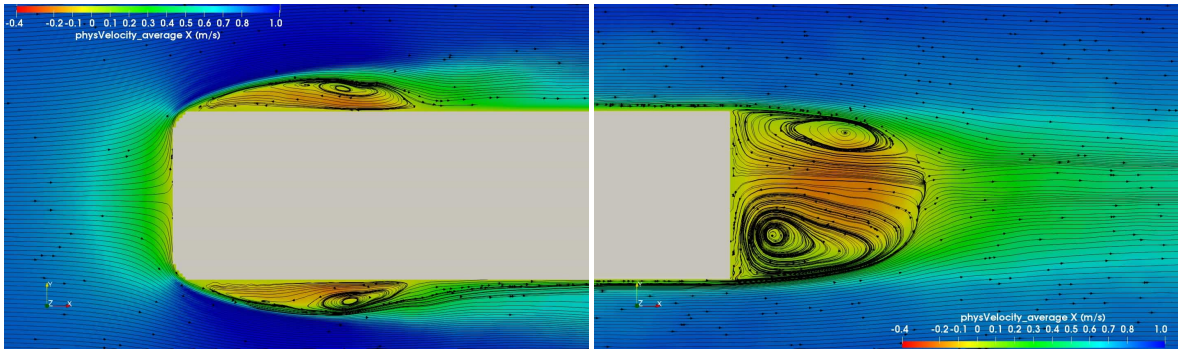

(a) Front-end of R8 model, Re=8,000 (b) Rear-end of R8 model, Re=8,000

Figure B.4: Time-average contour plot of x-velocity of R8 at a Re=8,000 with N=46

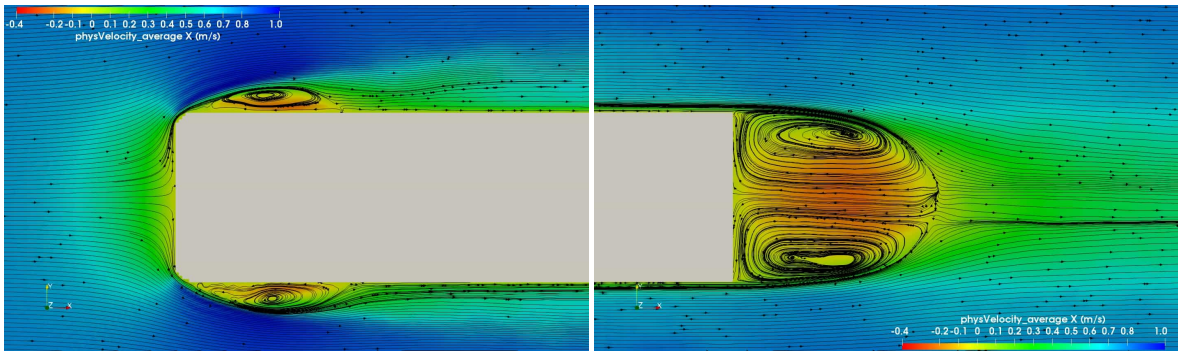

(a) Front-end of R8 model, Re=24,000 (b) Rear-end of R8 model, Re=24,000

Figure B.5: Time-average contour plot of x-velocity of R8 at a Re=24,000 with N=46

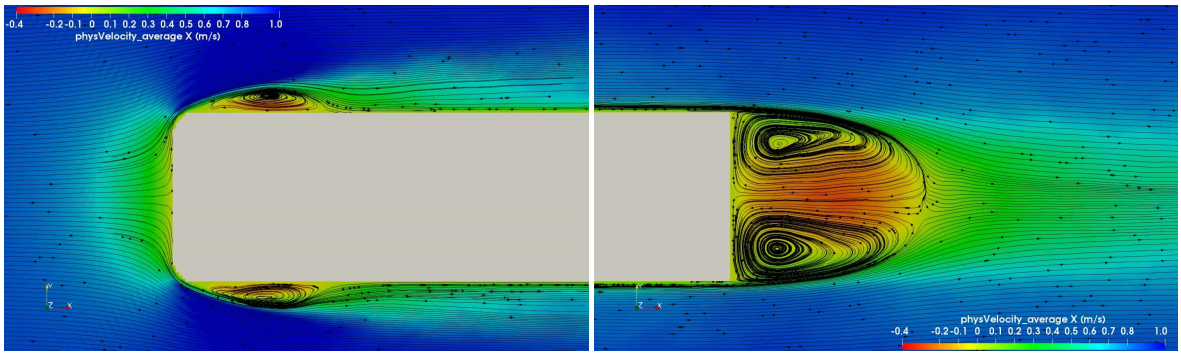

(a) Front-end of R8 model, Re=48,000 (b) Rear-end of R8 model, Re=48,000

Figure B.6: Time-average contour plot of x-velocity of R8 at a Re=48,000 with N=46

R8T18

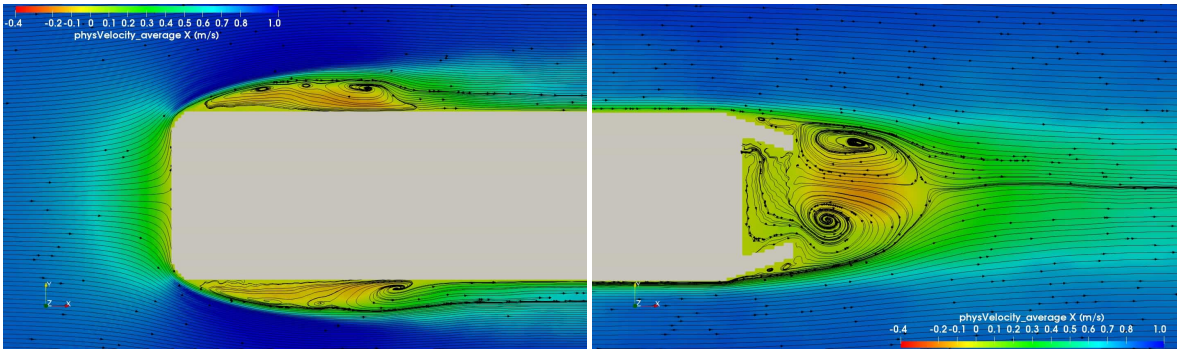

(a) Front-end of R8T18 model, Re=8,000 (b) Rear-end of R8T18 model, Re=8,000

Figure B.7: Time-average contour plot of x-velocity of R8T18 at a Re=8,000 with N=46

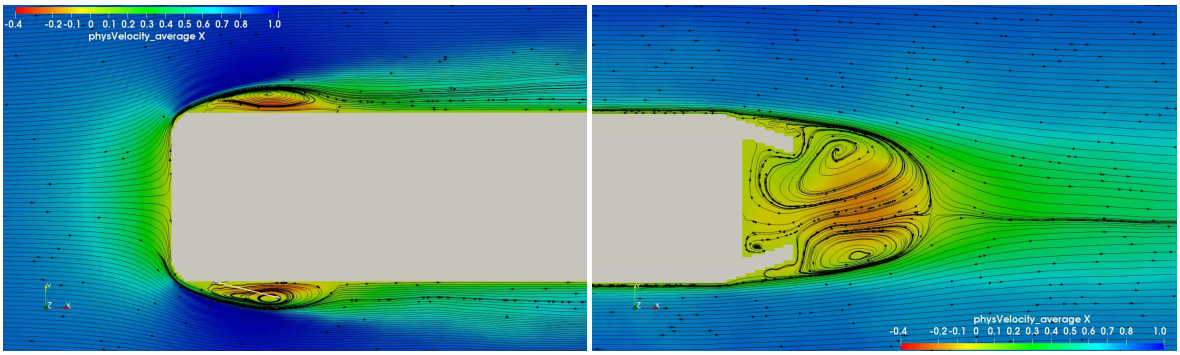

(a) Front-end of R8T18 model, Re=24,000 (b) Rear-end of R8T18 model, Re=24,000

Figure B.8: Time-average contour plot of x-velocity of R8t18 at a Re=24,000 with N=46

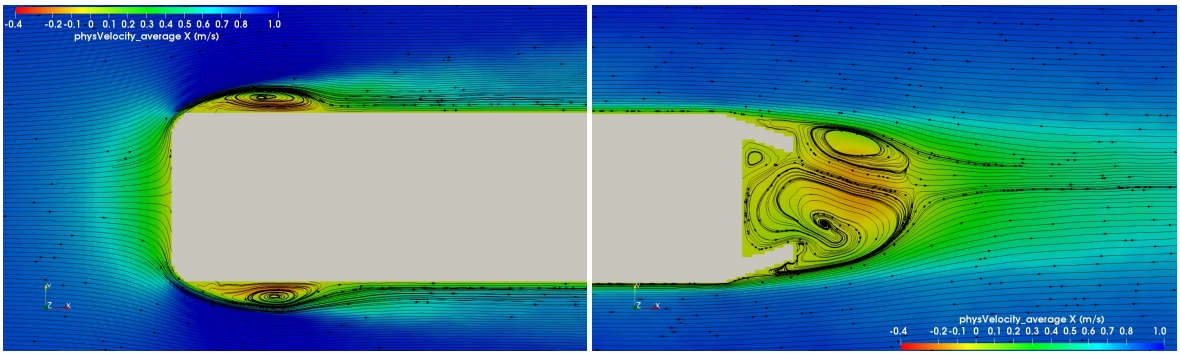

(a) Front-end of R8T18 model, Re=48,000 (b) Rear-end of R8T18 model, Re=48,000

Figure B.9: Time-average contour plot of x-velocity of R8T18 at a Re=48,000 with N=46

R12

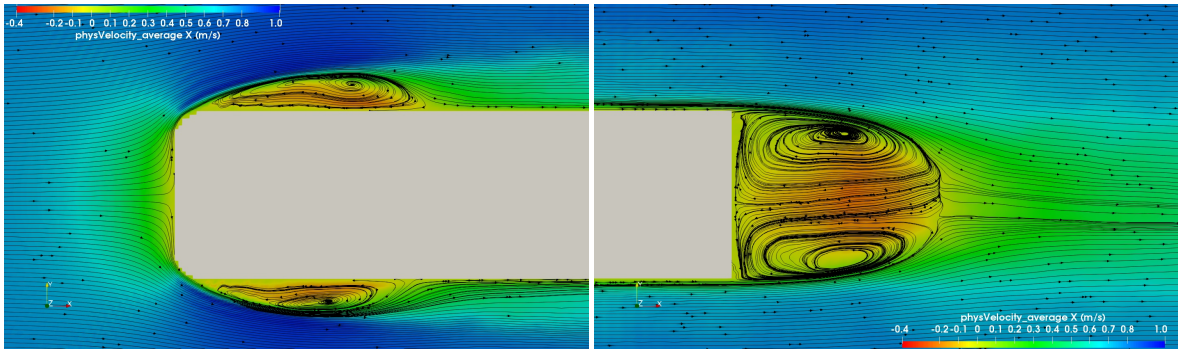

(a) Front-end of R12 model, Re=8,000 (b) Rear-end of R12model, Re=8,000

Figure B.10: Time-average contour plot of x-velocity of 12 at a Re=8,000 with N=46

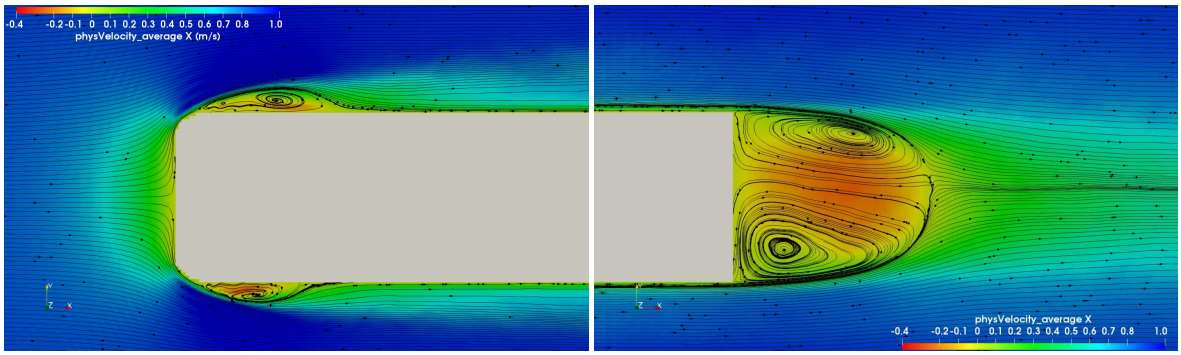

(a) Front-end of R12 model, Re=24,000 (b) Rear-end of R12 model, Re=24,000

Figure B.11: Time-average contour plot of x-velocity of R12 at a Re=24,000 with N=46

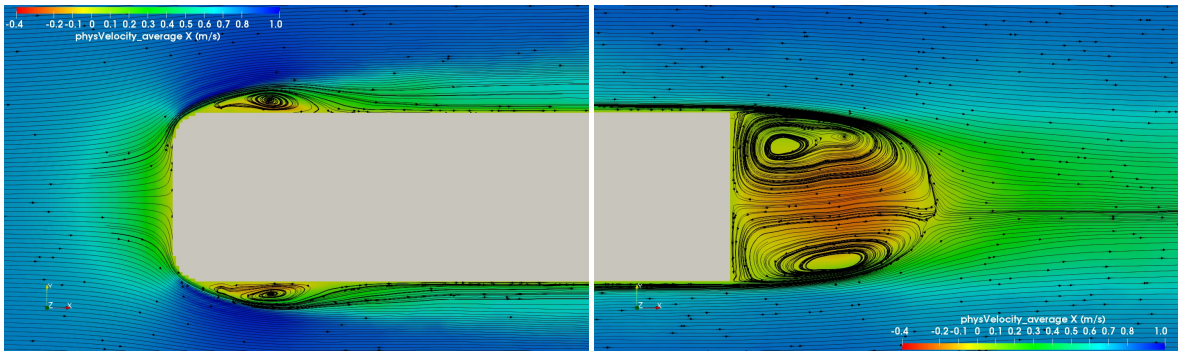

(a) Front-end of R12 model, Re=48,000 (b) Rear-end of R12model, Re=48,000

Figure B.12: Time-average contour plot of x-velocity of 12 at a Re=48,000 with N=46

R12T6

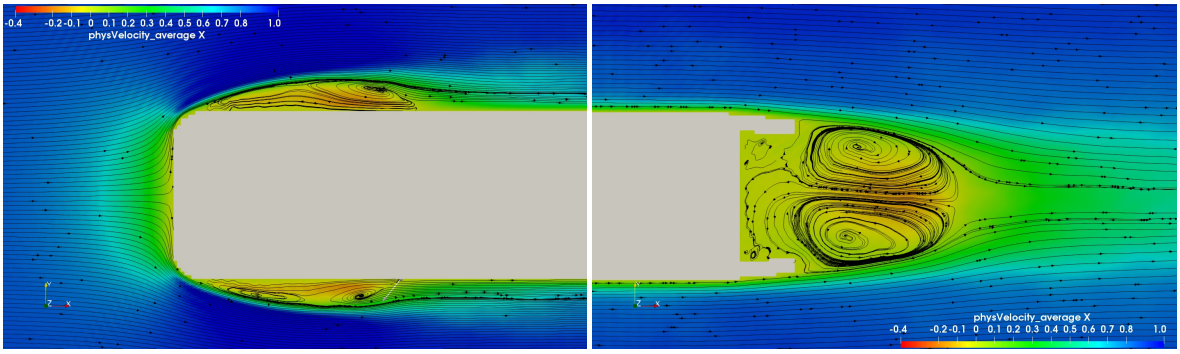

(a) Front-end of R12 model, Re=8,000 (b) Rear-end of R12model, Re=8,000

Figure B.13: Time-average contour plot of x-velocity of 12 at a Re=8,000 with N=46

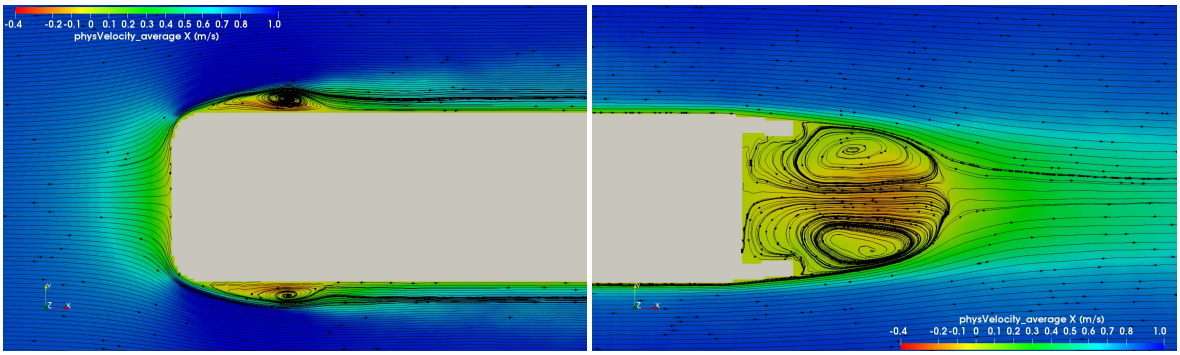

(a) Front-end of R12 model, Re=24,000 (b) Rear-end of R12 model, Re=24,000

Figure B.14: Time-average contour plot of x-velocity of R12 at a Re=24,000 with N=46

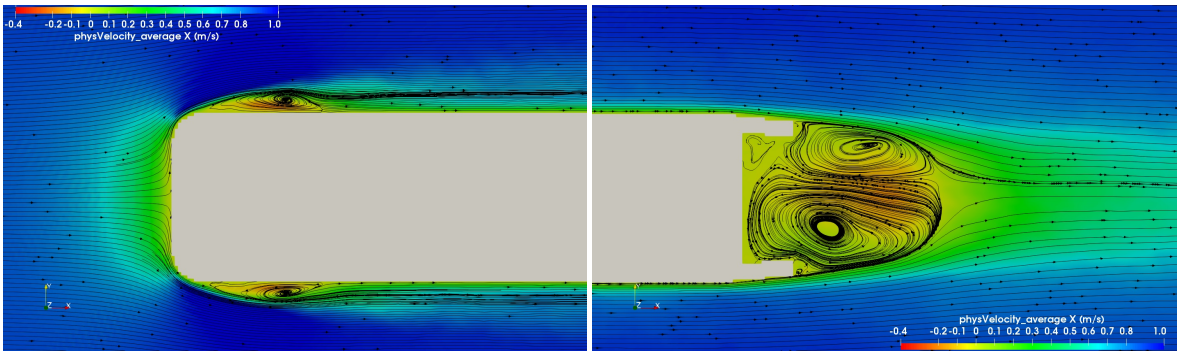

(a) Front-end of R12 model, Re=48,000 (b) Rear-end of R12model, Re=48,000

Figure B.15: Time-average contour plot of x-velocity of 12 at a Re=48,000 with N=46

R24

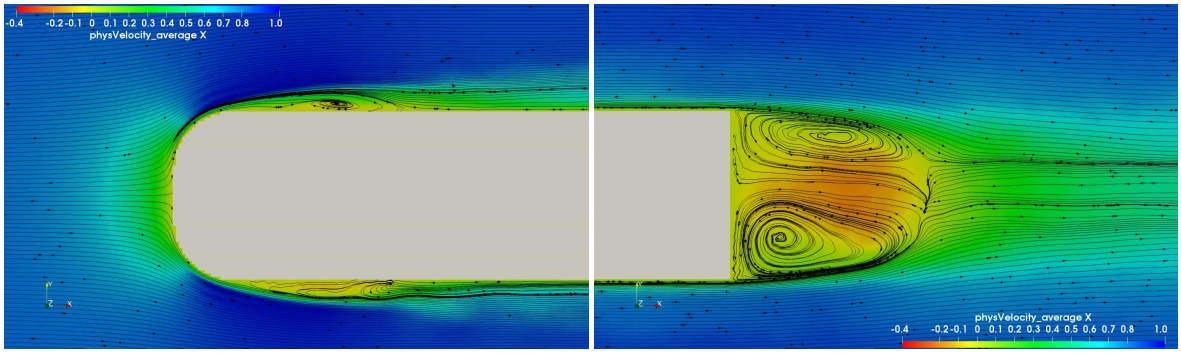

(a) Front-end of R24 model, Re=8,000 (b) Rear-end of R24 model, Re=8,000

Figure B.16: Time-average contour plot of x-velocity of R24 at a Re=8,000 with N=46

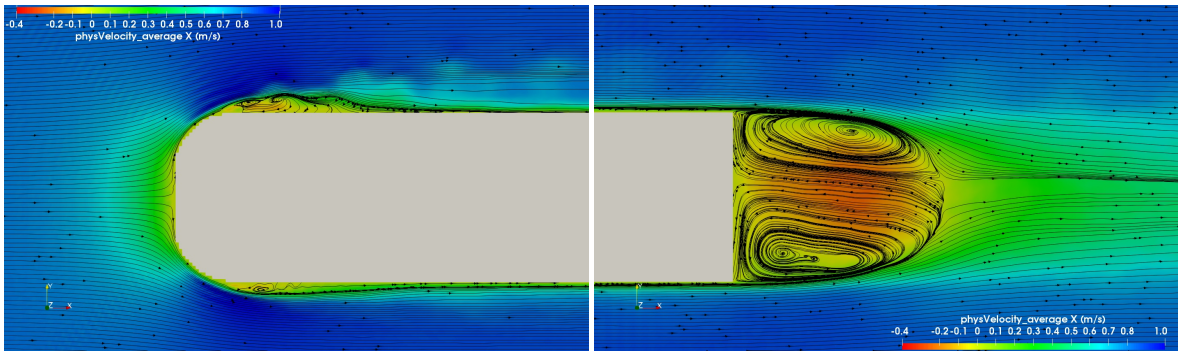

(a) Front-end of R24 model, Re=24,000 (b) Rear-end of R24 model, Re=24,000

Figure B.17: Time-average contour plot of x-velocity of R24 at a Re=24,000 with N=46

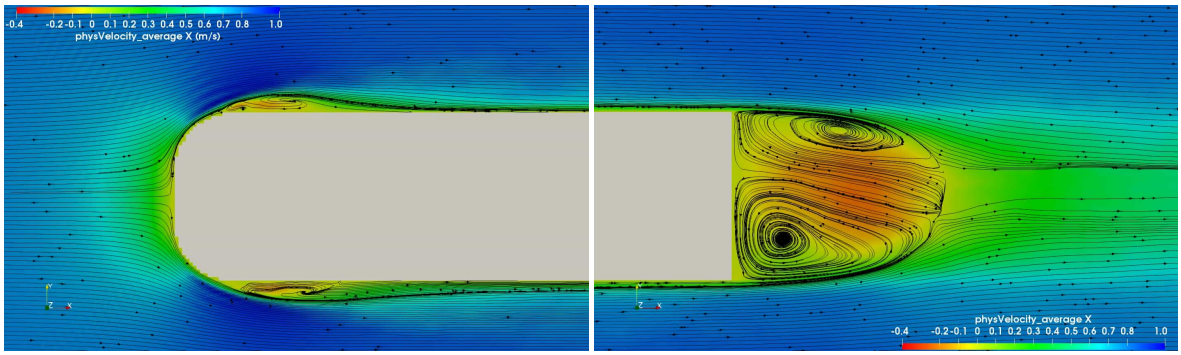

(a) Front-end of R24 model, Re=48,000 (b) Rear-end of R24 model, Re=48,000

Figure B.18: Time-average contour plot of x-velocity of R24 at a Re=48,000 with N=46

R24T12

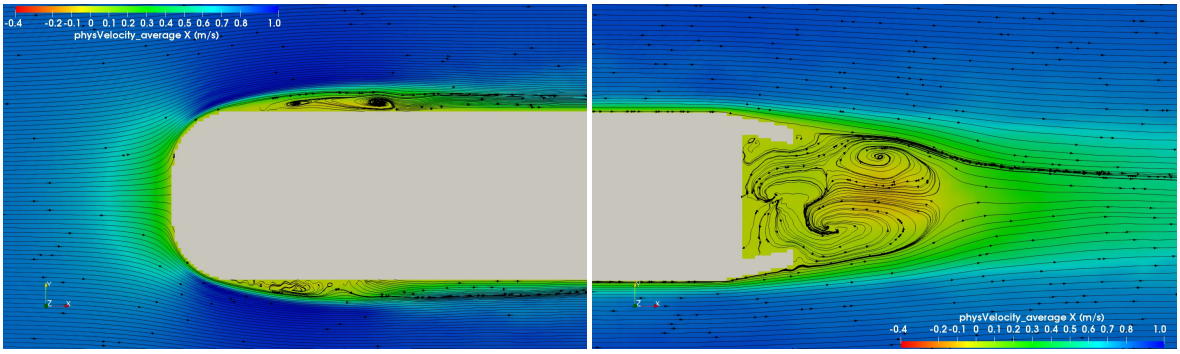

(a) Front-end of R24T12 model, Re=8,000 (b) Rear-end of R24T12 model, Re=8,000

Figure B.19: Time-average contour plot of x-velocity of R24T12 at a Re=8,000 with N=46

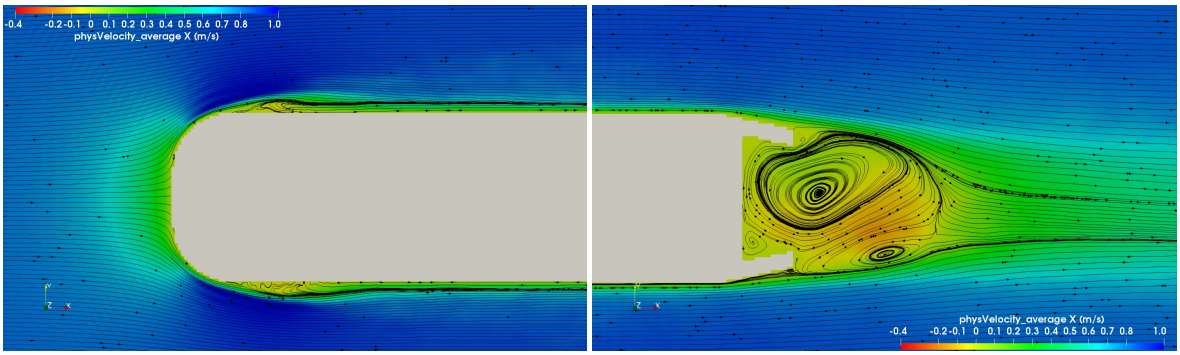

(a) Front-end of R24T12 model, Re=24,000 (b) Rear-end of R24T12 model, Re=24,000

Figure B.20: Time-average contour plot of x-velocity of R24T12 at a Re=24,000 with N=46

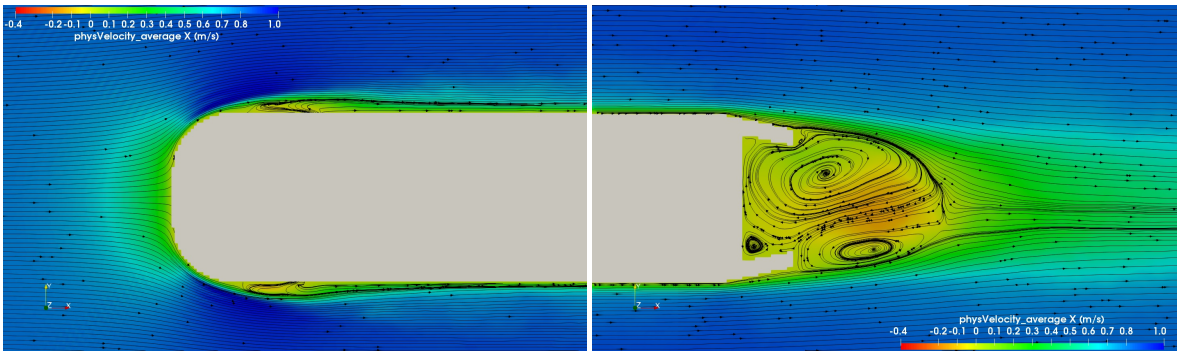

(a) Front-end of R24T12 model, Re=48,000 (b) Rear-end of R24T12 model, Re=48,000

Figure B.21: Time-average contour plot of x-velocity of R24T12 at a Re=48,000 with N=46

C

Pressure Plots

This appendix gives the front and rear pressure coefficient distribution for all the simulated configurations and Reynolds numbers.

R4

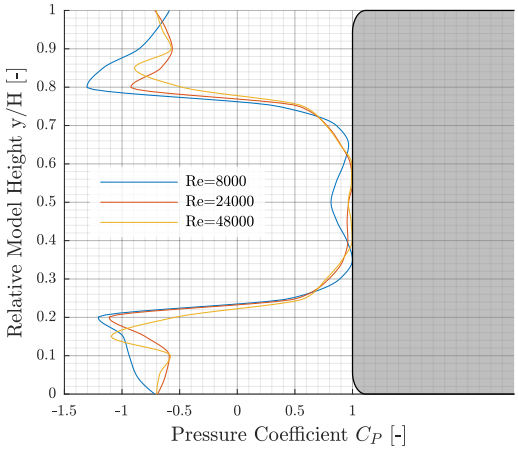

(a) Pressure coefficient front z=0.5W

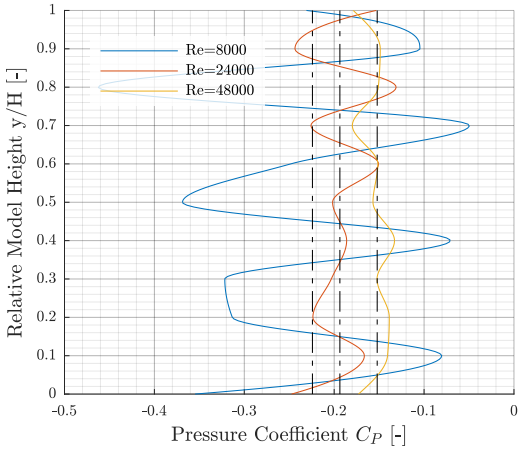

(b) Pressure coefficient rear z=0.5W

Figure C.1

R4t18

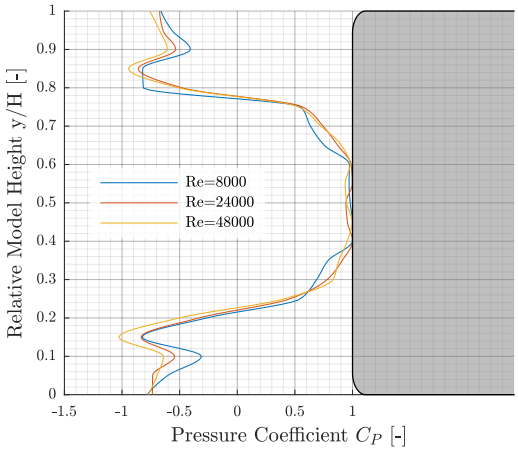

(a) Pressure coefficient front z=0.5W

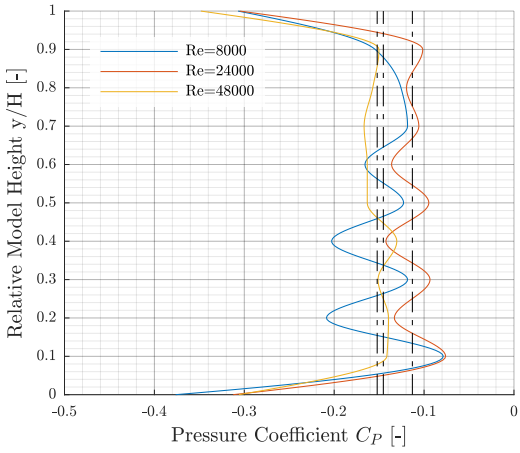

(b) Pressure coefficient rear z=0.5W

Figure C.2

R8

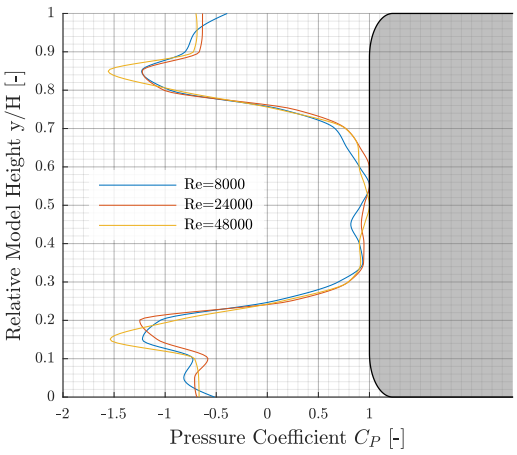

(a) Pressure coefficient front z=0.5W

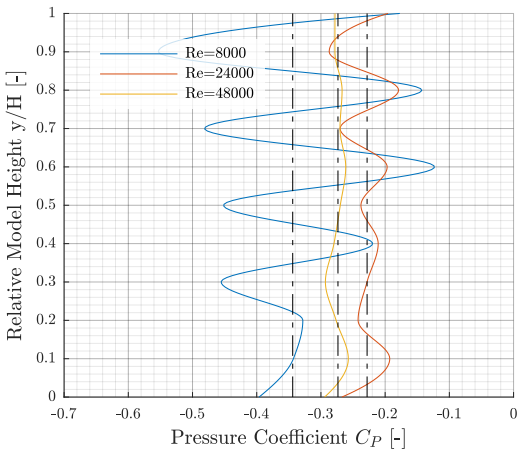

(b) Pressure coefficient rear z=0.5W

Figure C.3

R8T18

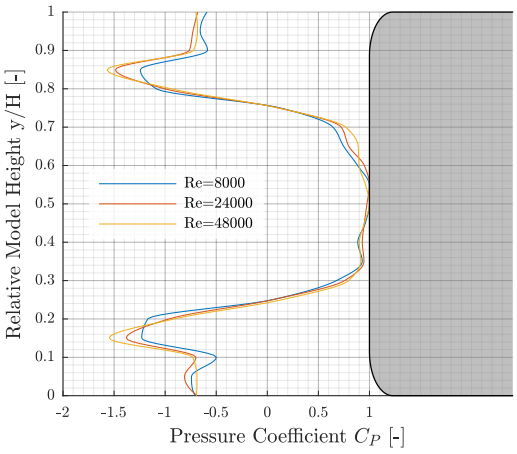

(a) Pressure coefficient front z=0.5W

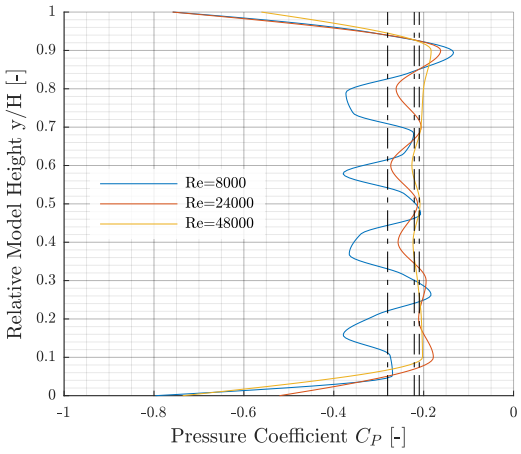

(b) Pressure coefficient rear z=0.5W

Figure C.4

R12

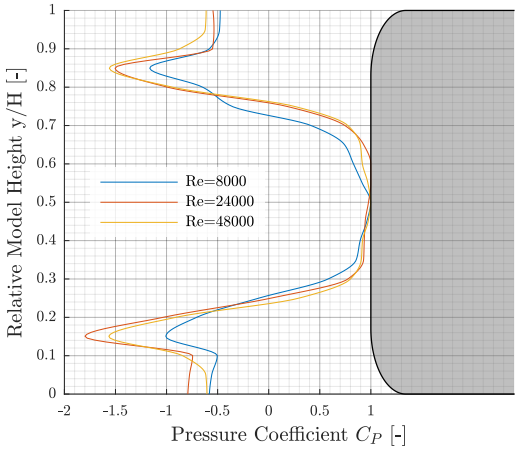

(a) Pressure coefficient front z=0.5W

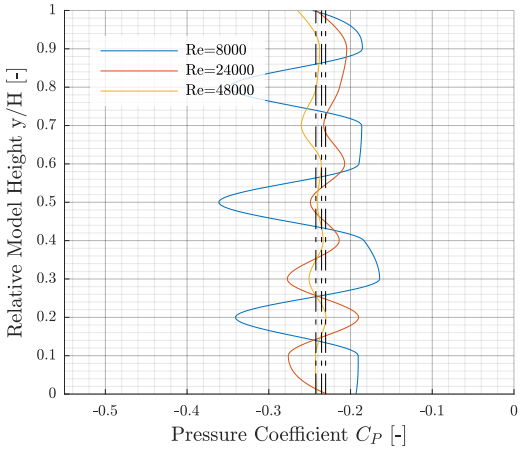

(b) Pressure coefficient rear z=0.5W

Figure C.5

R12T6

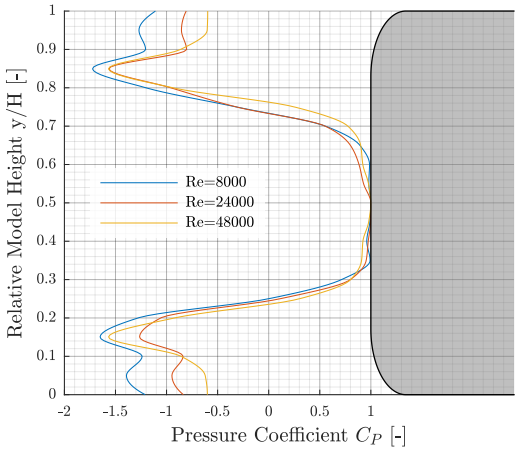

(a) Pressure coefficient front z=0.5W

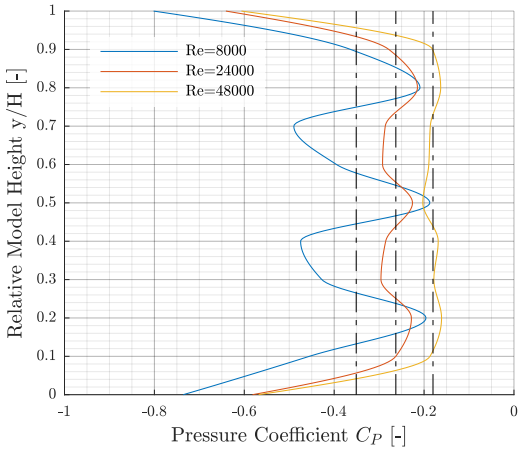

(b) Pressure coefficient rear z=0.5W

Figure C.6

R24

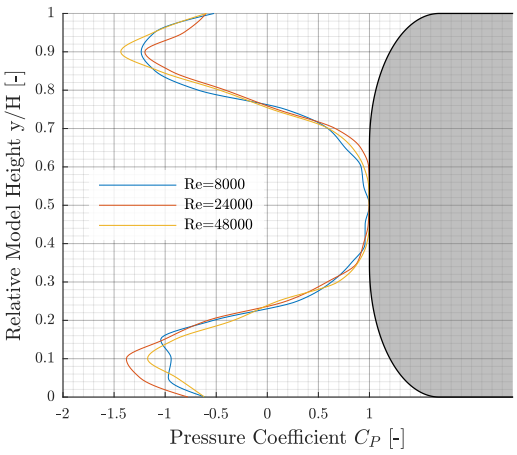

(a) Pressure coefficient front z=0.5W

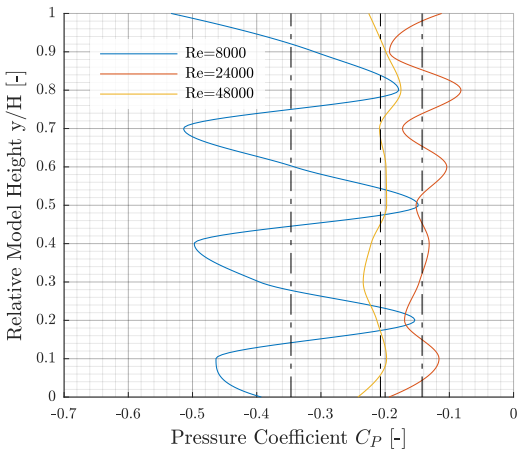

(b) Pressure coefficient rear z=0.5W

Figure C.7

R24T12

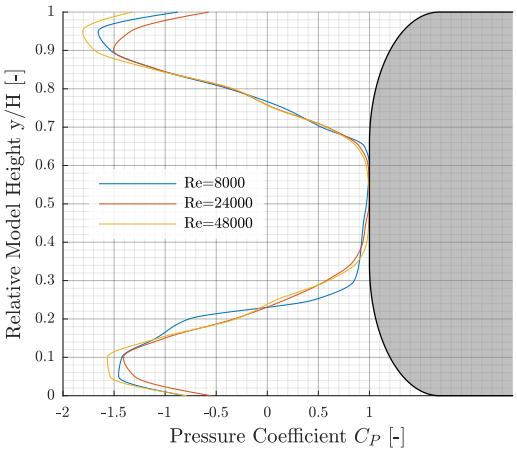

(a) Pressure coefficient front z=0.5W

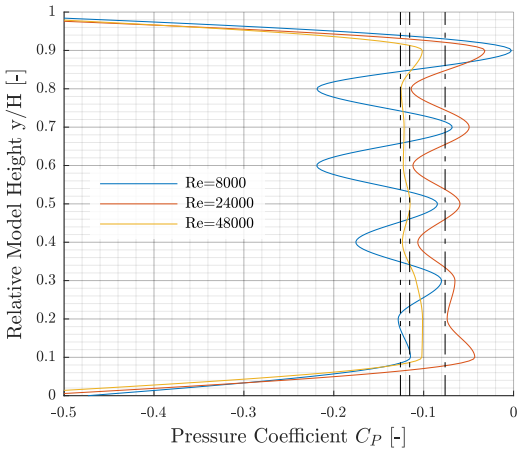

(b) Pressure coefficient rear z=0.5W

Figure C.8